PERFORMANCE ENHANCEMENT OF GRAPHENE/SILICON BASED NEAR-INFRARED SCHOTTKY PHOTODIODES

A Thesis Submitted to
the Graduate School of Engineering and Sciences of
İzmir Institute of Technology
in Partial Fulfillment of the Requirements for the Degree of

DOCTOR OF PHILOSOPHY

in Physics

by
Mehmet FİDAN

July 2022
İZMİR

ACKNOWLEDGMENTS

First of all, I would like to thank my advisor, Prof. Dr. Cem Çelebi. His encouragement and support made this thesis possible. I am very grateful for his invaluable help, guidance and his endless patience as well as his understanding provided during this thesis. I would like to thank my committee members of my thesis Prof. Dr. Gülnur Aygün, Prof. Dr. Serdar Özçelik, Prof. Dr. Cem Tozlu and Assist. Prof. Dr. Özhan Ünverdi for their participations. I am also thankful to Dr. Hasan Aydın, Alper Yanılmaz and Dilce Özkendir for their friendship and support. In addition, I would like to thank Sparks Electronics Ltd. in Turkey for their support in device fabrication processes. Also, I would like to acknowledge my institution, İzmir Institute of Technology, for providing me research facilities during my PhD study.

Finally, I want to deeply thanks to my family for leading me to this stage. Especially, I want to thank my mother for her understanding, support, and love since elementary school. Also, I would like to express my heart-felt gratitude to my wife Selin Fidan for ceaseless support, love and believing in me.

This work was supported as part of the project no. BAP089 that has been approved by Yaşar University Project Evaluation Commission.

ABSTRACT

PERFORMANCE ENHANCEMENT OF GRAPHENE/SILICON BASED NEAR-INFRARED SCHOTTKY PHOTODIODES

This thesis presents an experimental investigation on the performance enhancement of graphene/silicon based near-infrared Schottky photodiodes. The photodiode devices were fabricated by transferring CVD graphene layers onto n-type silicon (n-Si) substrates. The samples exhibited strong Schottky diode character and had high spectral sensitivity at 905 nm peak wavelength. The Schottky contact characteristics of the samples (e.g., barrier height, ideality factor and sheet resistance) were determined by analyzing the current-voltage measurement data. All the samples demonstrated a clear photovoltaic activity under light illumination. The Schottky barrier height (SBH) in Gr/n-Si photodiodes was tuned as a function of light power density. Light power density driven modification of the SBH was correlated with the variation in the measured open-circuit voltage.

The impact of junction area and number of graphene layers on the spectral responsivity and response speed of Gr/n-Si based Schottky photodiodes were also investigated. Firstly, three batches of Gr/n-Si photodiode samples with junction area of 4 mm^2, 12 mm^2 and 20 mm^2 were produced by transferring monolayer CVD graphene on individual n-Si substrates. The sample with 20 mm^2 junction area reached a spectral response of 0.76 AW^{-1}, which is the highest value reported in the literature for self-powered Gr/n-Si Schottky photodiodes without the modification of graphene electrode. In contrast to their spectral responsivities, the response speed of the samples was found to be lowered as a function of the junction area. After that, we increased the number of graphene layers on n-Si. Wavelength-resolved and time-dependent photocurrent measurements demonstrated that both spectral responsivity and response speed are enhanced as the number of graphene layers is increased from 1 to 3 on n-Si substrates. This thesis showed that the device performance of Gr/n-Si Schottky photodiodes can be modified simply by changing the size of graphene electrode and/or as well as the number of graphene layers on n-Si without need of external doping of graphene layer or engineering Gr/n-Si interface.

ÖZET

GRAFEN/SİLİKON BAZLI YAKIN-KIZILÖTESİ SCHOTTKY FOTODİYOTUNUN PERFORMANS GELİŞTİRMESİ

Bu tez, grafen/silikon bazlı yakın kızılötesi Schottky fotodiyotlarının performans artışı üzerine deneysel bir araştırma sunar. Fotodiyot aygıtları, CVD grafen katmanlarının n-tipi silikon (n-Si) substratlara aktarılmasıyla üretildi. Numuneler, güçlü Schottky diyot karakteri sergiledi ve 905 nm tepe dalga boyunda yüksek spektral duyarlılığa sahipti. Numunelerin Schottky temas özellikleri (örn. bariyer yüksekliği, idealite faktörü ve tabaka direnci) akım-voltaj ölçüm verileri analiz edilerek belirlendi. Tüm numuneler, ışık aydınlatması altında net bir fotovoltaik aktivite gösterdi. Gr/n-Si fotodiyotlardaki Schottky engel yüksekliği (SBH), ışık gücü yoğunluğunun bir fonksiyonu olarak değiştirildi. SBH'nin ışık gücü yoğunluğuna dayalı modifikasyonu, ölçülen açık devre voltajındaki varyasyon ile ilişkilendirildi.

Bağlantı alanı ve grafen katman sayısının Gr/n-Si tabanlı Schottky fotodiyotların spektral duyarlılığı ve tepki hızı üzerindeki etkisi de ayrıca araştırıldı. İlk olarak, 4 mm^2, 12 mm^2 ve 20 mm^2 bağlantı alanına sahip üç grup Gr/n-Si fotodiyot örneklerleri, birbirinden ayrı n-Si alttaşları üzerine tek katmanlı CVD grafen aktarılarak üretildi. 20 mm^2 bağlantı alanına sahip olan aygıt, grafen elektrot modifikasyonu olmadan kendi gücünü sağlayan Gr/n-Si Schottky fotodiyotları için literatürde bildirilen en yüksek değer olan 0.76 AW^{-1} spektral tepkisine ulaştı. Spektral duyarlılıklarının aksine, örneklerin tepki hızlarının bağlantı alanının bir fonksiyonu olarak düştüğü bulundu. Sonrasında, n-Si üzerindeki grafen katmanlarının sayısını artırdık. Dalga boyu çözümlü ve zamana bağlı fotoakım ölçümleri, n-Si substratlar üzerinde grafen katmanlarının sayısı 1'den 3'e yükseltildiğinde hem spektral duyarlılığın hem de tepki hızının arttığını gösterdi. Bu tez, Gr/n-Si Schottky fotodiyotlarının aygıt performansının, grafen elektrotunun boyutunu ve/veya n-Si üzerindeki grafen katmanlarının sayısını değiştirerek, grafen katmanının harici katkılanmasına gerek kalmadan basitçe değiştirilebileceğini göstermiştir.

To my Family

TABLE OF CONTENTS

LIST OF FIGURES

Figure **Page**

Figure **Page**

Figure **Page**

Figure **Page**

Figure **Page**

Figure **Page**

LIST OF TABLES

LIST OF SYMBOLS

Φ_m	Work function of metal
Φ_{sc}	Work function of semiconductor
E_F	Fermi level
Φ_{Gr}	Work function of graphene
χ	Electron affinity
E_F^m	Fermi level of metal
E_F^{sc}	Fermi level of semiconductor
E_V^{sc}	Valance band of semiconductor
E_C^{sc}	Conduction band of semiconductor
Φ_B	Schottky barrier height
Φ_{bi}	Built-in potential
W_d	Depletion region
ε_0	Vacuum permittivity
ε_s	Permittivity of semiconductor medium
q	Elementary charge
E	Electric field
Φ_0	Neutral energy level
E_g	Band gap energy
V_F	Forward bias voltage
V_R	Reverse bias voltage
A^*	Richardson constant
k_B	Boltzmann constant
T	Absolute temperature
m^*	Effective mass
h	Planck constant
J_{sm}	Current density flowing from semiconductor into metal
J_s	Saturation current density
A	Active junction area
n	Carrier density
v_f	Fermi velocity

T'	Optical transmittance
λ	Wavelength
c	Speed of light
ω	Angular frequency
η	Ideality factor
R_s	Sheet resistance
V_{oc}	Open-circuit voltage
I_{sc}	Short-circuit current
R	Responsivity
I_d	Dark current
I_p	Photocurrent
I_0	Reverse saturation current
D^*	Specific detectivity
P	Light power
t_r	Rise time
t_d	Decay time
μ	Mobility
B_w	Bandwidth
V_b	Bias voltage
Cu	Copper
Ni	Nickel
Au	Gold
Cr	Chromium
HF	Hydrofluoric acid
$FeCl_3$	Iron (III) chloride
HCl	Hydrochloric acid
SiC	Silicon Carbide
SiO	Silicon monoxide
ITO	Indium Tin Oxide
P3HT	Poly(3-hexylthiophene-2,5-diyl)
MoO_3	Molybdenum trioxide
TFSA	Trifluoromethanesulfonic acid

LIST OF ABBREVIATIONS

Gr	Graphene
n-Si	n-type Silicon
p-Si	p-type Silicon
MS	Metal / Semiconductor
Sc	Semiconductor
n-Sc	n-type Semiconductor
I-V	Current - Voltage
2D	Two Dimensional
PR	Photoresist
UHV	Ultra-High Vacuum
CVD	Chemical Vapor Deposition
HOPG	Highly Ordered Pyrolytic Graphite
FWHM	Full Width Half Maximum
SBH	Schottky Barrier Height
FE	Field Emission
TFE	Thermionic Field Emission
TE	Thermal Emission
e-h	Electron - Hole
NEP	Noise Equivalent Power
UV	Ultraviolet
THz	Terahertz
MIR	Mid-infrared
SRH	Shockley-Read-Hall
R.T	Room Temperature
PCB	Printed Circuit Board
LIDAR	Light Detection and Ranging

CHAPTER 1

INTRODUCTION

Photodiodes based on graphene/semiconductor heterojunctions have attracted great interest in the recent years since they exhibit relatively high spectral responsivities and reduced dark currents comparable to those of commercial p-n or p-i-n type photodiodes. Graphene, as a single-layer of carbon atoms arranged in a hexagonal lattice, exhibits high carrier mobility and inherently high optical transparency with great potential to replace transparent conductors such as Ti/W, Ni/Au, and ITO in optoelectronic device applications (Nair et al., 2008; Bonaccorso et al., 2010). Due to ease of fabrication, compatibility with existing CMOS technologies and broadband photo-detection capabilities, solar cells and photodetectors fabricated out of graphene/semiconductor heterojunctions are being comprehensively investigated in the recent years (Xinming Li et al., 2010; An et al., 2013; Di Bartolomeo 2016). It has been shown that a rectifying Schottky junction is created when graphene is interfaced with most of the semiconducting materials like Si, GaAs, GaN and ZnO (Chen et al., 2011; Tomer et al., 2015; Ranade et al., 2019; Qin et al., 2019). For example, a Schottky barrier height (SBH) in an energy range between 0.3 – 1.0 eV has been identified for the heterojunction of chemical vapor deposition (CVD) grown p-type graphene (Gr) and n-type Si (n-Si) substrate (Liu and Kar 2014; Sinha and Lee 2014; Zhang et al., 2006; H. Y. Kim et al., 2013; Parui et al., 2014; Y. Wang, Yang, Ballesio, et al., 2020). Gr/n-Si based Schottky junction photodiodes are sensitive to light in the visible and short wavelength infrared spectral regions due to the band gap of Si (Pelella et al., 2021). In such devices, the electric field arising from the built-in potential of around 0.5 – 0.7 V is strong enough to effectively separate the photo-generated charge carriers at the depletion region of Gr/n-Si heterojunction subject to light illumination (Chen et al., 2011b; Yu et al., 2016; Tongay et al., 2012; Periyanagounder et al., 2018). Under the influence of light illumination, electrons moved to n-Si and holes injected to graphene electrode give rise to a measurable photocurrent and an open-circuit voltage in the Gr/n-Si devices even under zero-bias conditions. Therefore, Gr/n-Si heterostructure is utilized as a Schottky photodiode operating in self-powered (photovoltaic) mode which is

tempting especially for solar cell and photo-detection applications without power consumption.

Contrary to conventional metal/semiconductor type Schottky junction photodiodes, where the Fermi level of metal electrode remains unchanged due to high density of states, the Fermi level of graphene can be shifted towards either lower or higher energy states relative to its charge neutrality point (Dirac point) simply by electrostatic gating and/or charge transfer doping from an external source. The shift of graphene's Fermi level leads to a measurable change in its work function. As a consequence of the change in graphene's work function, the SBH at the interface of graphene/semiconductor heterojunction is modified accordingly. For example, temperature dependent current-voltage (I-V) measurements revealed that the SBH of Gr/n-Si heterostructure can be tuned in an energy range between 0.4 – 0.6 eV when the graphene layer is chemically doped with NH_4F and/or $AuCl_3$ molecules (Tang et al., 2015). It has been shown in another study that the spectral responsivity of Gr/n-Si Schottky junction near-infrared photodiodes can be increased by modifying the work function of graphene electrode with P3HT polymer molecules (Aydin et al., 2018). In the one part of this thesis work, we have investigated the impact of light on the SBH of Gr/n-Si based Schottky barrier near-infrared photodiodes. The measurements conducted under 905 nm wavelength light showed that the SBH in Gr/n-Si photodiodes can be effectively tuned in an energy range between 0.7 and 0.9 eV with incident photons. The photo-generated holes transferred from n-Si substrate to graphene electrode shift its Fermi level towards higher energy states well below the Dirac point and therefore increase the SBH of Gr/n-Si photodiode under light illumination.

The device characteristics including the spectral response (R), specific detectivity (D*), noise equivalent power (NEP) and response speed of Gr/n-Si based Schottky junction photodiodes have been studied extensively in earlier works (Xinming Li et al., 2016; Lv et al., 2013; An et al., 2013; Aydin et al., 2018; Y. Wang, Yang, Lambada, et al., 2020; C. Wang et al., 2019). Gr/n-Si based photodiodes exhibit spectral responsivities in a range between 0.3-0.7 AW^{-1} and several AW^{-1} with a response time exceeding a few tens of microseconds (Riazimehr et al., 2016; Xinming Li et al., 2016; Fidan, Ünverdi, and Çelebi 2021; Şahan, Fidan, and Çelebi 2020; Periyanagounder et al., 2018; Riazimehr et al., 2019; Di Bartolomeo et al., 2017). Except its response speed, the spectral responsivity of Gr/n-Si heterojunction is comparable to those of commercial Si-based p-n and p-i-n type photodiodes. During the past few years, many interesting

strategies have been proposed to enhance the spectral responsivity of Gr/n-Si Schottky photodiodes. These include the modification of the doping level of either graphene electrode or underlying Si substrate and/or placing a thin oxide layer in between them and as well as nanotip patterning of the Si substrate underneath the graphene layer (Di Bartolomeo et al., 2017). As an example, Lv. et al., demonstrated a photovoltaic type near-infrared photodiode based on the heterojunction of CVD grown monolayer graphene with lightly doped n-Si (Lv et al., 2013). Under an illumination of 850 nm wavelength light, R, D* and response time of the device were measured as 29 mAW^{-1}, 3.9 $\times 10^{11}$ Jones, and ~100 μs at zero-bias voltage, respectively. Aydin et al., showed that the maximum R of Gr/n-Si Schottky photodiodes at 850 nm peak wavelength can be increased from 0.24 AW^{-1} to 0.78 AW^{-1} when Gr electrode is coated with P3HT polymer molecules (Aydin et al., 2018). In a subsequent work, Li et al., reported that D* and NEP values of Gr/n-Si Schottky junction photodiodes can be improved by an order of magnitude with a thin SiO_2 layer at the interface between Gr electrode and n-Si substrate due to strongly reduced dark current (Xinming Li et al., 2016).

Different from previous studies in the literature, we systematically investigated the impact of junction area on the above-mentioned device parameters of self-powered Gr/n-Si photodiodes. For the experiments, a large set of Gr/n-Si heterojunction devices was fabricated, in which a monolayer CVD grown graphene was employed as Schottky electrode and acted as the active region when interfaced with n-Si substrate. The junction area is changed by transferring graphene with different dimensions (e.g., 4 mm^2, 12 mm^2 and 20 mm^2) on three individual n-Si substrates. The electrical characteristics of all the samples displayed excellent rectification behavior. Wavelength resolved photocurrent spectroscopy measurements showed that the maximum spectral response of the photodiodes appears at 905 nm peak wavelength and increases linearly from 0.16 AW^{-1} to 0.76 AW^{-1} as the junction area is increased from 4 mm^2 to 20 mm^2. The rise in the junction area lead to greater depletion region length of the junction. This promotes the vertical electric field across the Gr/n-Si heterojunction and enhances the effective separation/collection of photo-generated charge carriers at the depletion region. Because of enhanced charge separation and collection efficiency, the photocurrent and thus the spectral response of our photodiode increase as a function of the size of graphene electrode. Based on the time-resolved photocurrent measurements, the photodiode with 20 mm^2 graphene exhibited lower response speed compared to that

of the photodiode having 4 mm^2 sized graphene electrode under the influence of 905 nm wavelength light pulsed with 5 kHz frequency.

Additionally, we examined the effect of the number of graphene layers on the R and response speed of Gr/n-Si Schottky junction photodiodes. The devices are fabricated by transferring CVD grown graphene layers one by one on n-Si substrates, reaching up to three graphene layers. Wavelength-resolved and time-dependent photocurrent measurements demonstrated that both R and response speed of these type of photodiodes can be improved simultaneously as the number of graphene layers on n-Si is increased from 1 to 3. For example, the spectral response and the response speed of the fabricated device was found to be improved about 15 % (e.g., from 0.65 AW^{-1} to 0.75 AW^{-1}) and 50 % (e.g., 14 μs to 7 μs), respectively when three graphene layers are used as the hole collecting cathode electrode. The variation in the R and response speed of Gr/n-Si photodiodes with the number of graphene layers is explained in terms of the electronic transport characteristics of graphene electrode and charge injection dynamics. The carrier density (n) of the graphene electrode were determined as a function of the number of graphene layers using four probe and Hall effect measurement techniques. We found that the Fermi level is lowered relative to its initial stage when 2 and/or 3 graphene layers are used as electrode due to increased hole density. The shift of Fermi level towards lower energy states increases the work function of graphene electrode and as well as the magnitude of the built-in potential and junction electric field at the Gr/n-Si interface. This promotes greatly the effective separation of the photo-generated charge carriers at the depletion region and enhances the photocurrent of the device. Therefore, the spectral responsivity and response speed of the samples are expected to rise as a function of the number of graphene layers in agreement with increasing hole density.

The experimental results presented in this thesis are expected to offer exciting opportunities in terms of high value-added optoelectronic device technologies such as multi-wavelength light measurement, laser marking, laser range finder, high-speed photometry, position/motion detection, and more.

CHAPTER 2

FOUNDATION

2.1. Metal/Semiconductor (MS) Junctions

The junction between a metal and a semiconductor has a great potential for semiconductor device technology based on its ease of fabrication and simple device architecture. When a metal gets into contact with a semiconductor, two different types of junction are formed: i) ohmic junction or ii) rectifying junction, which is also known as a Schottky junction. The formation of such junctions is directly related to work functions of metal and semiconductor. The first investigation on metal/semiconductor (MS) junctions were done around 1874 by Braun (Braun 1875), who was shown the rectifying characteristics of them. Then, a well-known theoretical model about Schottky junction was revealed by Schottky and Sir Mott in 1938 (Schottky 1938; Mott 1938). After that, Bethe in 1942 enhanced this model in order to describe the electrical behavior of Schottky junction diodes by the thermionic emission model. Nowadays, the Schottky junctions with reproducible and reliable MS junction can be widely used in many applications such as solar cells, photodetectors and sensors. The energy band diagram and charge transport mechanism of a MS Schottky junctions will be introduced in detailed in the next sections. Later on, some important diode parameters such as ideality factor and Schottky barrier height will be extracted from current-voltage (I-V) characteristics of a MS junction.

2.1.1. Ideal MS Schottky Junction Contact

As mentioned above, when metal brought into contact with a semiconductor, two different electrical natures which are called ohmic or rectifying (Schottky) behavior occur at the interface depending on the difference in work function between metal and semiconductor. An ohmic junction typically becomes from metal contact built on a highly doped semiconductor. In such a contact, current flows through the junction in either direction with a linear I-V characteristics. Ohmic junctions obey the rule of

Ohm's law with a lower resistance compared to Schottky junction. On the other hand, Schottky junctions are formed with an intimate contact of metal onto a lightly doped semiconductor. Such a junction only allows the current to flow in one direction. Whereas the junction shows a high current (lower contact resistance) in one direction, negligible current (very high resistance) is seen in other direction, which are called as forward bias (ON state) and reverse bias (OFF state) conditions, respectively.

As shown in Figure 2.1, the work function is the energy difference between the Fermi level and the vacuum level of a solid. The work function for metal and semiconductor is denoted by Φ_m and Φ_{sc}, respectively. An ohmic or Schottky junction occurs as a results of having lower or higher work function of metal than that of n-type semiconductor, respectively. In contrast, for a p-type semiconductor, if the work function of metal is lower than the work function of semiconductor, Schottky junction is formed at the interface. A comparison for both ohmic and Schottky junction is given in Table 2.1 based on work function of metal and semiconductor.

Table 2.1. The comparison of work functions in MS junctions.

The relation of work functions	n-type semiconductor	p-type semiconductor
$\Phi_m > \Phi_{sc}$	Schottky	Ohmic
$\Phi_m < \Phi_{sc}$	Ohmic	Schottky

Each metal has the different work function value, meaning that the specific energy requires to lift an electron from the fermi level to the vacuum level for each solid. Fermi level (E_F) represents the highest energy level which is occupied by electrons at the absolute zero temperature in a solid. In the case of semiconductor, E_F can be varied with doping concentration. As an example, E_F is closer to the minimum of conduction band in n-type silicon (n-Si) with a value of 4.05 eV, whereas it is closer to the maximum of valance band in p-type silicon (p-Si) (approx. 5.17 eV). Electron affinity (χ) is defined as the energy difference of an electron between vacuum level and conduction band edge. Electron affinity for silicon is 4.05 eV and it does not change with doping concentration.

In practice, a Schottky junction occurs by deposition of metal onto surface of semiconductor. As an example for a Schottky junction, the non-contact and contact situations of a high work function-metal and an n-type semiconductor are investigated

in below, assuming the ideal condition without interfacial states and the other anomalies. Figure 2.1 demonstrates the energy band diagrams of such metal and n-type semiconductor in the case of both separated system and equilibrium.

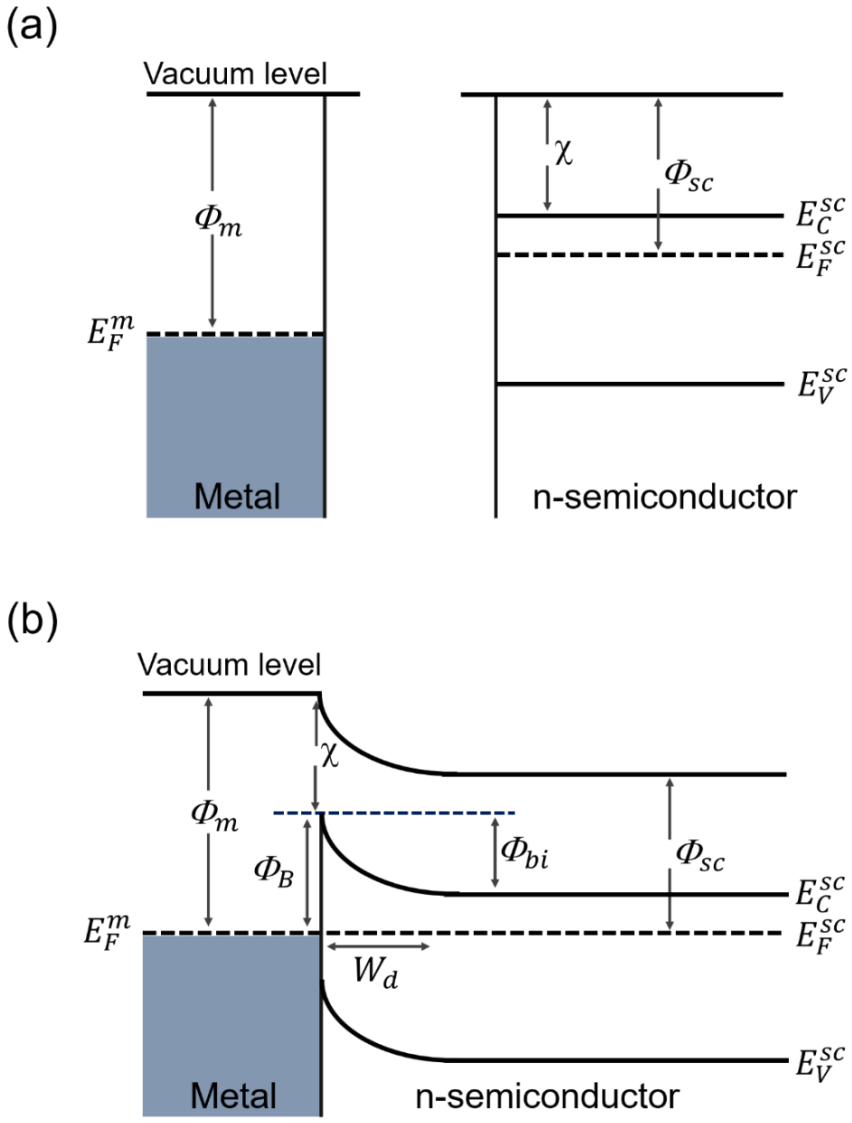

Φ_m: work function of metal
Φ_{sc}: work function of semiconductor
χ: electron affinity of semiconductor
E_F^m: fermi level of metal
E_F^{sc}: fermi level of semiconductor
E_V^{sc}: valance band of semiconductor
E_C^{sc}: conduction band of semiconductor
Φ_B: Schottky barrier height
Φ_{bi}: built-in potential
W_d: depletion region

Figure 2.1. Energy band diagram of metal and n-type semiconductor a) before and b) after contact.

When the metal and n-type semiconductor are kept separated each other as depicted in Figure 2.1(a), the energy levels are constant in the semiconductor. Also, their fermi levels would be independent of each other, in which fermi level of the semiconductor (E_F^{sc}) is greater than the fermi level of metal (E_F^m). When they come into an intimate contact as seen in Figure 2.1(b), due to the higher energy of the electrons in the conduction band of semiconductor compared to metal, electrons will flow from the semiconductor into the metal until their fermi levels get aligned to an equilibrium. The flow of electrons from semiconductor into metal leads to a decrease in electron concentration in the semiconductor side, resulting in the conduction band of semiconductor bends up. As a result of two different work functions, a depletion region (also called space charge region, W_d) is formed in the semiconductor which creates a built-in potential (Φ_{bi}) and denoted as: $\Phi_{bi} = \Phi_m - \Phi_{sc}$. According to Schottky-Mott model, the difference between the work function of metal and the electron affinity of semiconductor is called the Schottky barrier height (Φ_B) and it is written as below (Sze and Ng 2007).

$$\Phi_B = \Phi_m - \chi \qquad 2.1$$

Considering the Schottky-Mott relation, Φ_B actually depends only to choice of metal and there is no dependency to semiconductor doping level. So, better rectifying character with high $\Phi_B$value can be achieved by utilizing high work function metals on n-type semiconductors. Moreover, this equation is only valid in the case of no surface states and other anomalies at the interface of metal and semiconductor. The Φ_B estimated from the Schottky-Mott model differs from the experimentally obtained Φ_B value (Monch 1990; Cowley and Sze 1965; Hökelek and Robinson 1983). This inconsistency is explained due to some effects such as the presence of interface states, the existence of thin oxide layer and image force lowering. Such non-ideal effects at the interface of MS junctions have been discussed with detailed in following.

2.1.2. Non-ideal Effects at the MS Junctions

2.1.2.1. Image Force Lowering

Image force lowering (also known as Schottky barrier lowering) is an effect that causes decrease in Schottky barrier height. The presence of the metal changes the electric field near the interface of metal and semiconductor. When the charge carriers approach to MS junction interface, image charges occurs in the metal. So, the potential based on these charges reduces the Schottky barrier height.

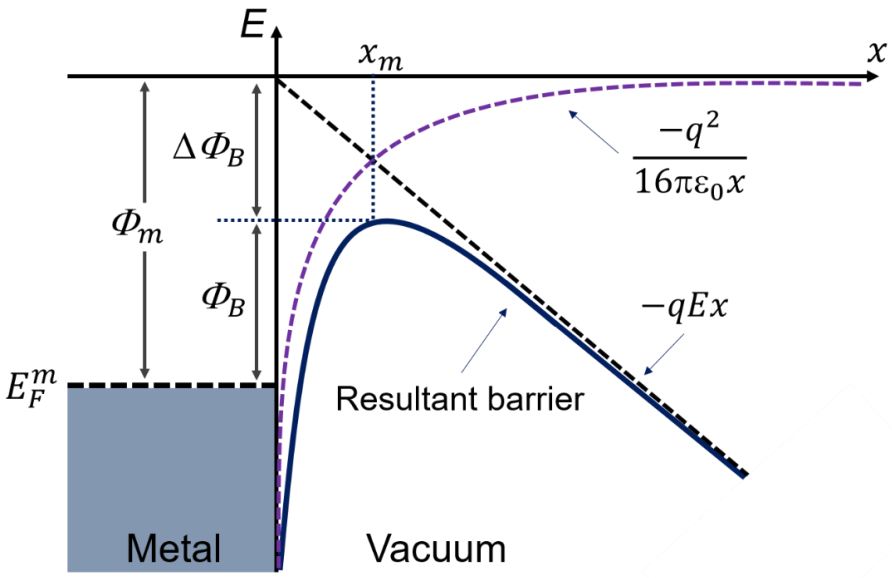

Figure 2.2. Energy band diagram between a metal and vacuum. The effective Schottky barrier is reduced when an electric field is applied to the surface. The reduction in the barrier is due to both the effect of electric field and the image force.

Figure 2.2 shows the potential energy of an electron at a constant electric field. An electron located at a distance of x from the metal generates an electric field perpendicular to the metal surface, which induces a positive image charge at a distance $(-x)$ inside the metal surface. The attractive force between these two charges is called image force and it is defined as,

$$F(x) = \frac{-q^2}{4\pi\varepsilon_0(2x)^2} = -qE \qquad 2.2$$

where ε_0 = 8.85 x 10^{12} F/m is the vacuum permittivity. The total potential energy of the electron equals to the sum of the barrier energy (-*qEx*) and the image potential energy as given below.

$$E(x) = \frac{-q^2}{16\pi\varepsilon_0 x} - qEx \tag{2.3}$$

The amount of image-force lowering ($\Delta\Phi_B$) and the location of the lowering x_m are extracted from the derivative of the potential energy $dE(x)/dx = 0$, as

$$x_m = \sqrt{\frac{q}{16\pi\varepsilon_0 E}} \tag{2.4}$$

and

$$\Delta\Phi_B = \sqrt{\frac{qE}{4\pi\varepsilon_0}} \tag{2.5}$$

While these results is applied to MS junction, the vacuum permittivity should be replaced by the permittivity of a semiconductor medium, ε_s. The effective Schottky barrier height (Φ_{Bn}) can be written as,

$$\Phi_{Bn} = \Phi_{Bn}^0 - \Delta\Phi_B \tag{2.6}$$

where, Φ_{Bn}^0 is Schottky barrier height at zero bias. Figure 2.3 indicates an energy band diagram of a MS junction under different biasing conditions by considering image force lowering. As shown in Figure 2.3, it should be noted that depending on bias voltage conditions, while the $\Delta\Phi_B$ reduces under forward bias because of the fact that W_{D1} is lightly decreased, it increases in reverse bias as a result of rise in the W_{D3}. Therefore, the image force lowering make the Schottky barrier height become a voltage dependent parameter.

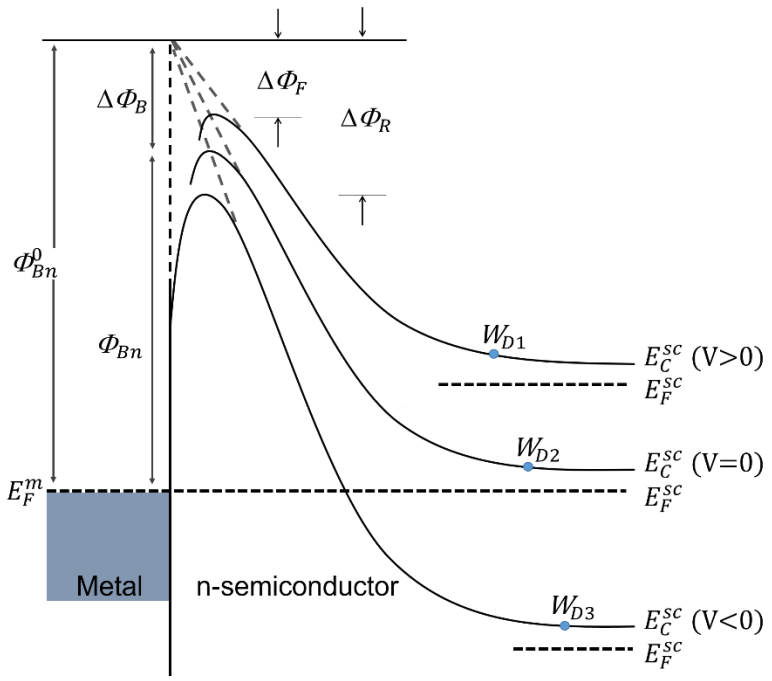

Figure 2.3. Energy band diagram depicting the Schottky barrier lowering effect for a MS junction under different bias conditions.

2.1.2.2. Bardeen Model

Another effect is that the existence of a thin insulating layer at the MS interface, resulting in an increase in the height of Schottky barrier. An additional voltage drop and an increment on the Schottky barrier height at the interface occurs due to the insulating layer (Sze and Ng 2007). It is known from the literature that larger barrier height provides better rectifying characteristics for a MS Schottky photodiodes (Card and Rhoderick 1971; Bardeen 1947; Lillington and Townsend 1976). Therefore, in practice, a Schottky devices with a thin insulating layer is deliberately employed to enhance the device characteristics.

Figure 2.4 demonstrates the band structure of a metal and n-type semiconductor including surface states and a thin insulator layer at the interface. The surface states are distributed within the semiconductor band gap and are characterized by neutral energy level denoted by Φ_0. This neutral level is located above the valance band of semiconductor separating acceptor and donor type surface states. The states above and below of this neutral level corresponds to acceptor-like (neutral when the empty and negatively charged when occupied by an electron) and donor-like (neutral when full of electron and positively charged when the empty), respectively.

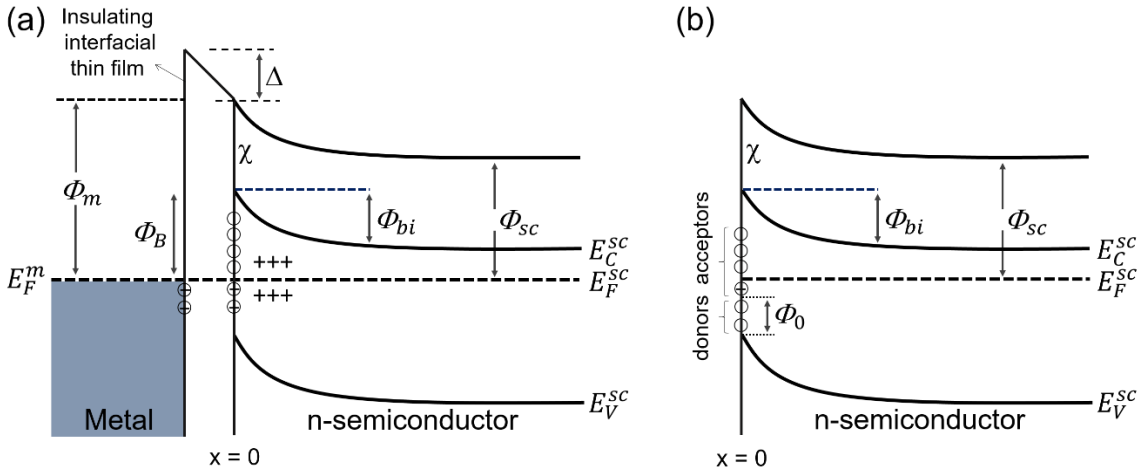

Figure 2.4. (a) Energy band diagram of a MS contact with a transparent atomically thin interfacial layer. Full and empty acceptor-like surface states are indicated at the interface. (b) Neutral level (Φ_0) separates the acceptor and donor type surface states.

The surface states change the charge distribution in the depletion region and thus create an impact on the height of Schottky barrier (Tyagi 1984). While both acceptor and donor type surface states presents at the semiconductor surface, the net interface-trap charge will be zero since the fermi level at the surface overlaps with the neutral level. In the case of being present a localized charge at the surface, it causes the fermi level pinning to the neutral point due to high density of surface states. In detail, this effect on surface states was studied by J. Bardeen in a study (Bardeen 1947). Schottky barrier height can be expressed by using Bardeen model as in the following (Tyagi 1984),

$$\Phi_{Bn} = E_g - \Phi_0 \qquad 2.7$$

In conclusion, the fermi level at the junction is pinned by the surface states at the neutral level and Schottky barrier height becomes independent of metal's work function. Considering all above factors, Φ_B prediction of the junction is not a straightforward calculation that could be easily found from the equation 2.1 by Schottky-Mott model. Instead, the electrical measurement such as I-V must be done in order to estimate Φ_B value with a high precision as explained in the upcoming section 2.1.4.

2.1.3. Current Transport Mechanisms

The current transport in Schottky junction is governed by the majority carriers over the barrier, in contrast to p-n junction where the current transport is controlled by the minority carriers comprising both electron and holes (Sze and Ng 2007). This leads some advantages to Schottky junction photodiodes such as low junction capacitance and fast recovery time as compared to p-n junction photodiodes. The current in Schottky junction flows from semiconductor to metal (or from metal to semiconductor) under operation of forward bias (or reverse bias).

Figure 2.5 illustrates the energy band diagram of metal and n-type semiconductor Schottky junction under forward bias and reverse bias condition. The junction is said to be in the non-equilibrium when applied bias voltage, resulting fermi level of semiconductor moves upward or downward. In the case of forward bias shown in Figure 2.5(a), the barrier is decreased by the amount of forward bias voltage (V_F) when the metal contact is positively biased with respect to the semiconductor. As a result of that, electron moves easily from the semiconductor into metal. On the other hand, under reverse bias, the semiconductor to metal barrier is increased by the amount of reverse bias (V_R) and the electron flowing from metal to semiconductor is prevented by Schottky barrier as depicted in Figure 2.5(b). It should be taken into account that Schottky barrier height remains constant in both conditions unless there is no image-force lowering or any other anomalies.

Figure 2.6 shows five basic transport processes occurred at the junction of metal and n-type semiconductor under forward bias. These processes for a forward bias Schottky barrier are (1) thermionic emission of electrons over the barrier which is dominant process for Schottky diodes, (2) quantum mechanical tunnelling of electrons through the barrier (seen in heavily doped semiconductor), (3) recombination of electrons and holes in the depletion region, (4) diffusion of electrons from the bulk of semiconductor in the space-charge region, (5) diffusion of holes injected from the metal into the semiconductor. The charge transport across a Schottky diode can be varied depending on the temperature and doping level of the semiconductor.

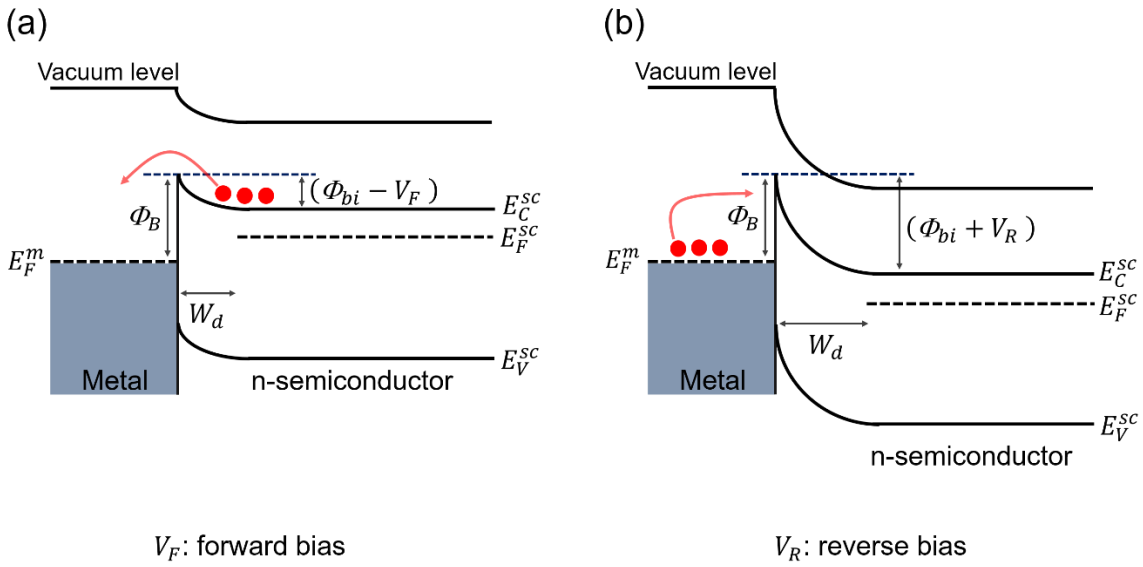

Figure 2.5. Energy band diagram of metal and n-type semiconductor Schottky junction (a) under forward bias and (b) reverse bias condition. Electrons are illustrated by red spheres.

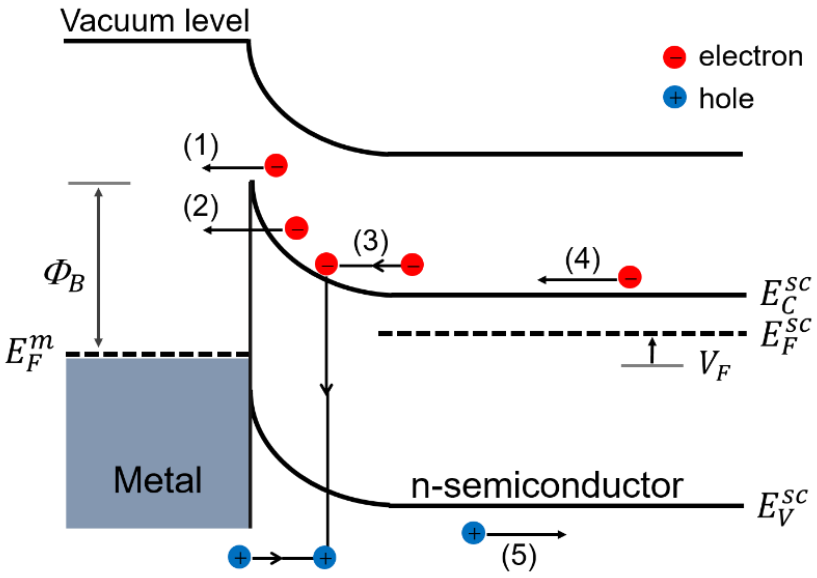

Figure 2.6. Five transport mechanism are shown in the energy band diagram of metal/n-type semiconductor Schottky junction under forward bias.

2.1.3.1. Thermionic Emission Model

According to thermionic emission model suggested by Bethe (Bethe 1991), charge transport occurs through the emission of charge carriers with the energies equal to or much larger than k_BT at room temperature (25 meV) as well as the height of the potential barrier. The current density flowing from semiconductor into metal, J_{sm} can be expressed as (Sze and Ng 2007),

$$J_{sm} = A^*T^2 exp\left(\frac{-q\Phi_B}{k_BT}\right) exp\left(\frac{qV}{k_BT}\right) \quad 2.8$$

where q, T, k_B are the elementary charge, the absolute temperature, the Boltzmann constant, respectively. Additionally, $A^* = 4\pi qm^*k^2/h^3$ is the effective Richardson constant (~112 $Acm^{-2}K^{-2}$ for n-Si) where m^* is the effective mass and h is the Planck constant. It should be pointed out that the Richardson constant is principally an intrinsic property of a semiconductor depending effective mass carriers at conduction band edge. In addition, some situations like inhomogeneity in the Schottky barrier, interfacial layers and tunneling of charge carrier can be varied the value of A^*.

Since the Schottky barrier height is independent of applied bias voltage, the current density from metal to semiconductor remains constant. Therefore, the current density from metal to semiconductor, J_{ms} is given by,

$$J_{ms} = -A^*T^2 exp\left(\frac{-q\Phi_B}{k_BT}\right) \quad 2.9$$

then, the total current density is written by the sum of equations 2.8 and 2.9,

$$J = A^*T^2\left[exp\left(\frac{-q\Phi_B}{k_BT}\right) exp\left(\frac{qV}{k_BT} - 1\right)\right] \quad 2.10$$

$$= J_s\left[exp\left(\frac{qV}{k_BT} - 1\right)\right] \quad 2.11$$

where J_s is the saturation current density. It is obvious that J_s depicts exponentially dependent on Schottky barrier height and inversely proportional to temperature.

In contrast to ideal Schottky contact, current transport deviates from the thermionic emission behavior described in equation 2.11. In practical Schottky diodes, thermionic emission model of non-ideal junctions can be expressed as in the following,

$$J = J_s \left[exp\left(\frac{qV}{\eta k_B T} - 1\right)\right] \quad 2.12$$

where η is the ideality factor of the diode defined as a measure how closely the diodes follows an ideal diode equation. Moreover, the important Schottky diodes parameters such as barrier height, sheet resistance and ideality factor can be derived from the slope (or intercept) of linear region of the equation 2.12. A more detailed about this is given by the following section of 2.1.4.

2.1.3.2. Diffusion Theory

Diffusion theory is another charge transport mechanism observed for the forward bias Schottky junction. According to this theory suggested by Schottky, the charge flowing is limited by the drift (local electric field) and diffusion (carrier concentration gradient) processes in the space-charge region. Therefore, the current density can be expressed as (Sze and Ng 2007),

$$J = q \left[n\mu_n \varepsilon + D_n \frac{d_n}{dx} \right]$$

$$= q\, D_n \left[\frac{n}{k_B T} \frac{dE_c}{dx} + \frac{d_n}{dx} \right] \quad 2.13$$

where, D_n and μ_n is the electron diffusion coefficient and the electron mobility, respectively. The local electric field depends on the shape of the depletion region. At the steady-state condition, the current density is independent of x. Thus, using an integrating factor of $exp(E_c(x)/kT)$ the current density over the entire depletion region can be written by,

$$J = q\, D_n n(x) exp\left[\left(\frac{E_c(x)}{k_B T}\right)\right]\Bigg|_{x=0}^{W_D} \quad 2.14$$

We assume that the carrier concentration at boundaries stay at equilibrium, and the current density for diffusion theory can be expressed by,

$$J \approx q\mu_n N_c \varepsilon_m exp\left(\frac{-q\Phi_B}{k_B T}\right)\left[exp\left(\frac{qV}{k_B T} - 1\right)\right] = J_D\left[exp\left(\frac{qV}{k_B T} - 1\right)\right] \qquad 2.15$$

where N_c, ε_m and J_D are the effective density of states in the conduction band of the semiconductor, the maximum electric field at the interface of metal-semiconductor and the saturation current density obtained from diffusion theory, respectively. The current densities acquired from thermionic emission and diffusion theory resembles to each other. However, J_D is affected by applied bias and also temperature dependent with less sensitive (Sze and Ng 2007).

2.1.3.3. Tunneling

Considering the heavily doped semiconductor and/or the operation at low temperature, the charge transport is dominated across the barrier by quantum mechanical tunneling (Sze and Ng 2007; Tyagi 1984). Charge carriers can be transported from semiconductor to metal or vice versa. For both forward and reverse biases, the tunneling can be occurred in a Schottky barrier junction as shown in Figure 2.7, respectively.

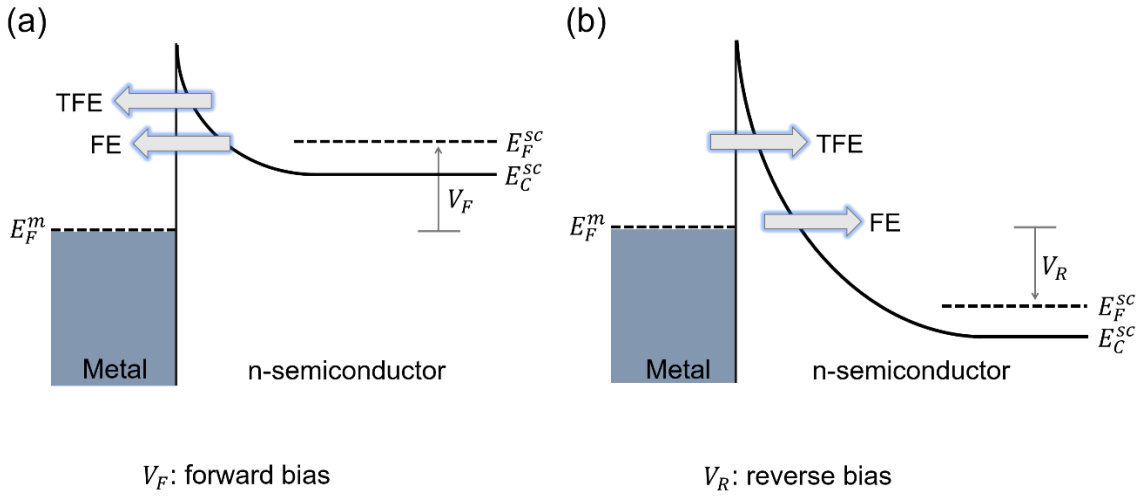

Figure 2.7. Field emission (FE) and thermionic field emission (TFE) tunneling currents illustrated on the energy band diagram of a Schottky barrier on n-type semiconductor under (a) forward bias and (b) reverse bias.

Due to heavily doped semiconductor, the depletion region is very narrow and the fermi level lies above the bottom of conduction band. The tunneling process is called the field emission (FE). At higher temperature, a significant number of electron move the energy states above the fermi level, where the barrier is thinner and lower. These thermally excited electrons can tunnel before reaching the top of the barrier. This tunneling is referred as thermionic field emission (TFE).

The tunneling mechanism was studied in detail by Padovani and Stratton (Padovani and Stratton 1966) and by Crowell and Rideout (Crowell and Rideout 1969). Due to difficult numerical analysis, the results which on the current density (J_t) are given below in the simple form (Donald A. Neamen 2006),

$$J_t \propto exp\left(\frac{-q\,\Phi_B}{E_{00}}\right) \tag{2.16}$$

where

$$E_{00} = \frac{q\hbar}{2\pi}\sqrt{\frac{N_d}{\varepsilon_s m^*}} \tag{2.17}$$

E_{00} is a crucial tunneling parameter and is related to the semiconductor characteristics. It is obvious that the tunneling current increases exponentially with donor concentration. Additionally, E_{00} can be utilized as a characteristic energy to determine relative contributions of transport mechanism by comparing with the thermal energy ($k_B T$). When $k_B T \gg qE_{00}$, the current transport mechanism is dominated by thermal emission (TE). On the other hand, field emission (FE) becomes dominate when $k_B T \ll qE_{00}$. In the case of $k_B T \sim qE_{00}$, the charge carriers tunnel from the barrier by thermionic field emission (TFE) (Schroder 2006; Padovani and Stratton 1966).

2.1.4. Measurement of Schottky Barrier Height

When considering only thermionic emission model, for a Schottky junction between a metal and a lightly doped semiconductor ($\Phi_m > \Phi_{sc}$), there is no net flow across the junction at zero bias. Therefore, the total current across the junction is given by,

$$J_{ms} + J_{sm} = 0 \tag{2.18}$$

J_{sm} was expressed by the equation 2.8 earlier. In the case of zero bias, J_{sm} can be rewritten as following,

$$J_{sm} = A^* T^2 exp\left(\frac{-q\,\Phi_B}{k_B T}\right) \tag{2.19}$$

where A^* is the Richardson constant. Moreover, J_{ms} which is also referred by reverse saturation current would equal to $-J_{sm}$ as shown below,

$$J_{ms} = -J_{sm} = -A^* T^2 exp\left(\frac{-q\,\Phi_B}{k_B T}\right) \tag{2.20}$$

When applying bias voltage to the junction, fermi level of metal remains unchanged and barrier height at the interface does not changed. So, J_{ms} is to be independent of applied bias. The correlation between the bias voltage and the total current flowing across the junction can be expressed by the Shockley equation as (Sze and Ng 2007),

$$J = J_{ms} + J_{sm} = J_0 \left[exp\left(\frac{q(V - IR_s)}{\eta k_B T}\right) - 1\right] \tag{2.21}$$

where, J_0 and IR_s are the reverse saturation current density and the voltage drop due to the series resistance, respectively. V_d which is known as the total voltage across the junction is equal to $V - IR_s$. For above equation, it should be a value of $V_d > 3k_b T/q$.

I-V measurement in dark can be utilized in order to determine the major parameters of MS Schottky contacts such as Schottky barrier height (Φ_B), ideality

factor (η) and sheet resistance (R_s). The dark I-V curve of a MS Schottky contact (e.g. a Pd/ZnO thin film grown on n-Si substrate is illustrated in Figure 2.8 (Somvanshi and Jit 2014). From forward bias region of I-V plot, the Φ_B, η and R_s can be extracted using the method developed by Cheung (Cheung and Cheung 1986). In the case of a high forward bias, the -1 term in the equation 2.21 can be neglected, so the equation can be rearranged in term of voltage as,

$$V = \frac{\eta k_B T}{q}\, ln\left(\frac{I}{I_0}\right) + IR_s \qquad 2.22$$

When the equation 2.22 is differentiated with respect to I,

$$\frac{dV}{dlnI} = \frac{\eta k_B T}{q} + IR_s \qquad 2.23$$

the equation 2.23 is obtained. As shown in Figure 2.9(a), the slope and the intercept of the straight line fitting of $dV/dln(I)$ versus I gives the R_s and $\eta k_B T/q$ values of the diode, respectively. Thus, the η of the diode can be calculated as following,

$$\eta = \frac{q}{k_B T}\,\frac{dV}{dln(I)} \qquad 2.24$$

Furthermore, in order to estimate the Φ_B of the junction, the following function of $H(I)$ can be defined from the equation 2.22.

$$H(I) = V - \frac{\eta k_B T}{q}\, ln\left(\frac{I}{AA^* T^2}\right) = IR_s + \eta\Phi_B \qquad 2.25$$

where, A is the active junction area of the diode in a unit of cm^2. The Φ_B can be determined from the intercept of the linear region of $H(I)$ vs. I plot as shown in Figure 2.9(b). In addition, the slope of this plot gives the second determination of R_s, so the consistency of R_s values can be checked by these two ways.

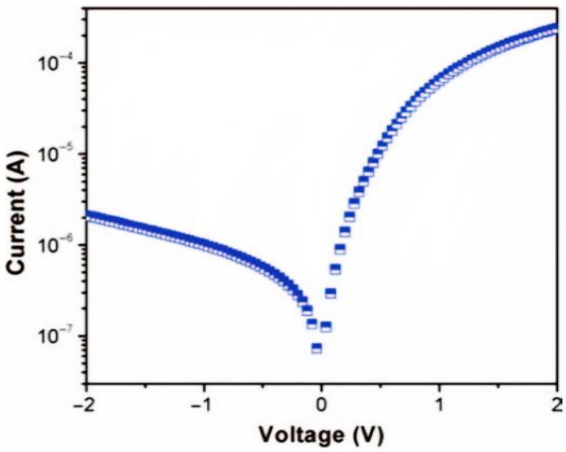

Figure 2.8. Semi-logarithmic plot of the I-V characteristics of Pd/ZnO thin film grown on n-Si substrate in dark, which shows a good rectifying behavior (Source: Somvanshi and Jit 2014).

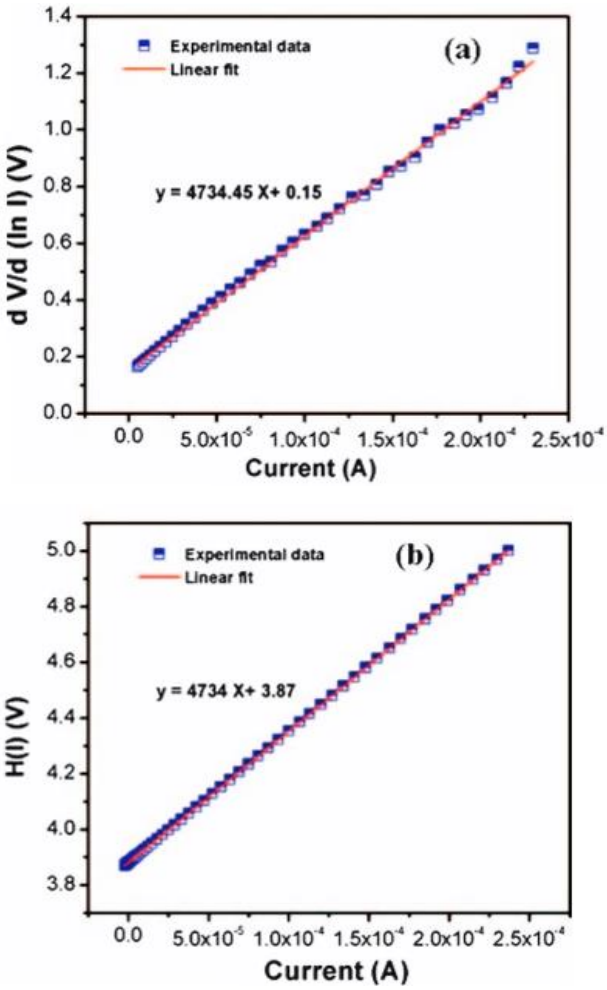

Figure 2.9. Plots of (a) $dV/dln(I)$ and (b) *H(I)* as a function of *I* for the sample of Pd/ZnO thin film grown on n-Si (Source: Somvanshi and Jit 2014).

2.2. Schottky Junction Photodiodes

Photodiodes convert optical signals into electric current. The photodetection process in the photodiodes comprising of three main mechanisms which includes carrier generation by absorption of light, carrier transport and collecting of carriers as current, respectively (Sze and Ng 2007). Photodiodes can be classified depending on types of the construction that p-n junction diode, p-i-n photodiode and Schottky junction photodiode. They are widely used for a variety of photodetection applications because of their characteristics. In general, all photodiodes function in the same way. When photons strike the diode, semiconductor absorbs these photons and electron-hole (e-h) pairs are created in the depletion region. Such photogenerated charge carriers are separated by the built-in electric field, producing a photocurrent.

A p-n photodiode occurs the combination of a p-type and n-type semiconductor. In the case of p-i-n diode, an intrinsic semiconductor is placed between these two semiconductors. The intrinsic layer provides some benefits to the diode which increases the depletion region and electric field strength. Therefore, the sensitivity and performance of p-i-n photodiodes is better than p-n diodes. As an instance, p-i-n photodiodes generally have higher response speed than the p-n photodiodes because of increased depletion region. Schottky photodiodes is created by the deposition of a thin metal layer on the surface of semiconductor. In Schottky junctions, depletion region is formed just beneath of the semiconductor depending on the energy difference between the work function of the metal and electron affinity of the semiconductor. These diodes have high response speed, low dark current and easy to fabricate compared to p-n and p-i-n photodiodes

In mostly, photodiodes can be manufactured from a variety of semiconductor materials such as silicon, germanium, indium gallium arsenide etc. depending on varying sensitivity toward to specific wavelength as well as differing response speed and dark current. The relationship between the band gap of semiconductor and the cut-off wavelength of light is expressed as,

$$\lambda_g(nm) = \frac{hc\ (\sim 1240\ eV\ nm)}{E_g(eV)} \qquad 2.26$$

where, h and c are the Planck constant (equals to 4.136×10^{-15} eV s) and the speed of light (2.99×10^{8} m/s), respectively. λ_g is known as the upper cut-off wavelength. For example, the band gap of silicon is 1.12 eV which corresponds to the upper cut-off wavelength of 1100 nm. Therefore, silicon based photodiodes are not sensitive to light above 1100 nm and is limited to a wavelength range of 400-1100 nm. In addition, it has the highest sensitivity for incoming light at the wavelength of $\sim$ 900 nm. On the other hand, for germanium with the band gap energy of 0.66 eV, λ_g is 1870 nm. As the focus of this thesis is on Schottky junction photodiode, the working principle of such diode in the photovoltaic and photoconductive modes will be examined in detailed in the next section.

2.2.1. Photodetection in Schottky Photodiodes

Schottky photodiodes are known to be highly efficiency photodetectors due to providing much higher speed and more efficient operation compared to the p-n and p-i-n junction photodiodes (Kosonocky 1991). Unlike typical p-n or p-i-n photodiodes, in Schottky photodiodes, a semi-transparent metal contact is necessary in order to get the exposure of the light into semiconductor. The amount of the photons reached to semiconductor in such diodes reduces some percentage due to the reflection of incident light from the semi-transparent metal surface. An anti-reflective coating can be provided to overcome this problem. But, the anti-reflective coating performs only at specific wavelength. Since graphene has both high electrical conductivity and optical transparency independent of wavelength, it can be used to remedy this problem in the Schottky photodiodes. A further information about graphene and graphene/semiconductor based Schottky photodiodes is given in sections 2.3 and 2.4.

2.2.1.1. Photovoltaic and Photoconductive Mode

Schottky junction photodiodes can operate in two modes: i) when there is no bias voltage, it is named as photovoltaic mode, ii) when a reverse bias is applied, it is known as photoconductive mode. In photovoltaic mode, the photogenerated charge carriers are created in the depletion region as a result of only light illumination as shown

in Figure 2.10, leading to limited photocurrent compared to photoconductive mode. Additionally, when the diode operates in this mode, it does not need an external power.

In photoconductive mode, higher photocurrent can be obtained from the diode since the applying reverse bias leads to rise in the width of depletion layer. As more photons reach into this depletion region, more photogenerated charges are collected, resulting in an increase in the photocurrent. However, the diode working in this mode has larger dark current. Figure 2.11 shows the energy band diagram of a metal/n-type semiconductor Schottky junction photodiode under reverse bias condition and light illumination. Such a photodiode can work in two modes depending on the photon energy as shown in the figure. The first one is that when the energy of incident photons is higher than the band gap of semiconductor ($h\nu > E_g$), the electrons excited from the valance band moves to the conduction band of semiconductor. Each ejected electron leaves behind an equivalent number of holes in the valance band. Thus, the generation of e-h pairs occurs in the depletion region inside semiconductor, determining the conductivity of the diode. The latter is internal photoemission mode. For a radiation with smaller photon energy than band gap but larger than Schottky barrier height ($q\Phi_B < h\nu < E_g$), the photo-excited electrons in the metal can pass over the Φ_B and can be collected by the n-type semiconductor. The height of the Schottky junction can be extensively determined by using this mode.

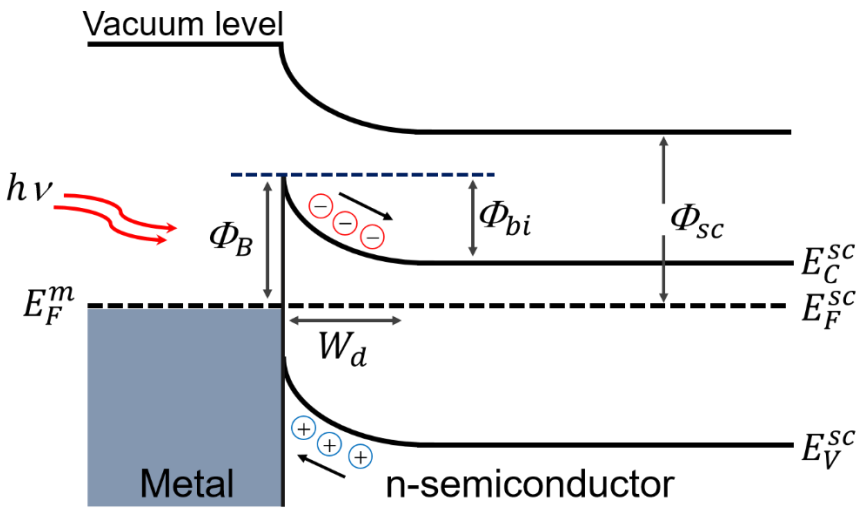

Figure 2.10. Energy band diagram of a metal/n-type semiconductor Schottky junction at zero bias and light illumination.

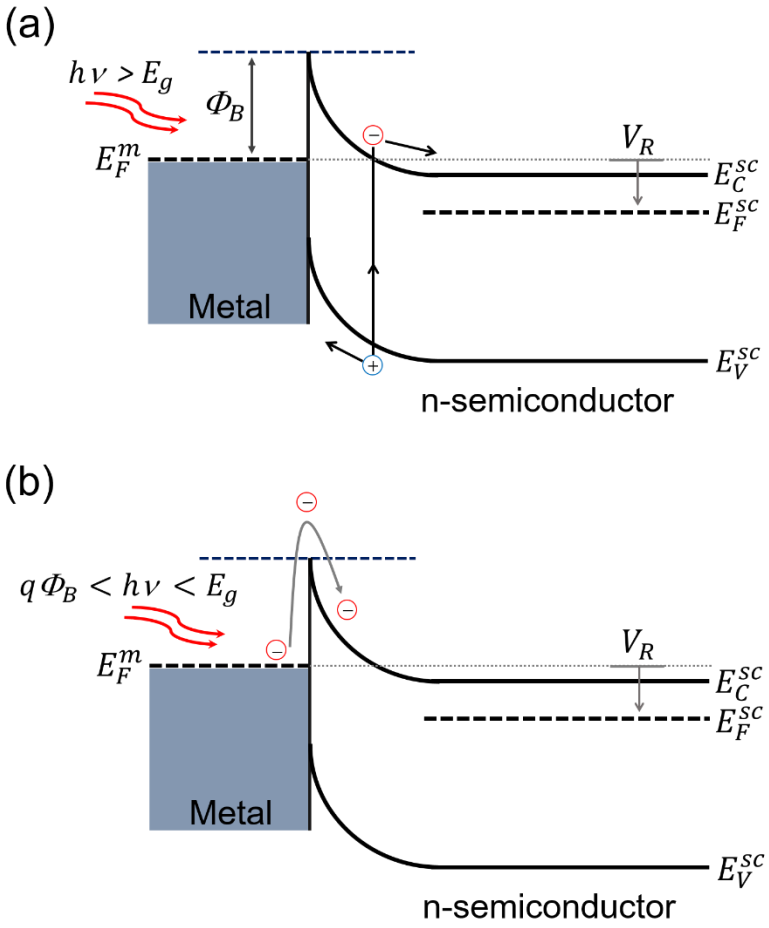

Figure 2.11. Energy band diagram of a metal/n-type semiconductor Schottky junction under reverse bias condition and light illumination in the case of (a) $h\nu > E_g$ which is known as band to band excitation of e-h pairs in the depletion region and, (b) $q\Phi_B < h\nu < E_g$ which is referred as internal photoemission of electrons from metal to n-type semiconductor.

2.2.2. Performance Parameters of Photodiodes

The performance of photodiodes is evaluated by a number of parameters. These are responsivity, response speed, specific detectivity and noise-equivalent power. The responsivity (R) is one of the most important diode parameters to characterize the properties of the light sensing and is defined as the ratio of generated photocurrent (I_p) to the incident light power (P) at a certain wavelength (in a unit of ampere per watt, A/W) and is expressed by the formula below,

$$R(A/W) = \frac{I_p - I_d}{P} \qquad 2.27$$

where I_d is the dark current. In other words, R is a measure of the conversion of the light power into photocurrent. It is varied with the wavelength of incident light. Besides, by applying reverse bias voltage, the magnitude of R increases slightly due to the enhanced depletion region of the photodiode.

Based on the measured R values of the diodes, specific detectivity (D^*) and noise-equivalent power (NEP) parameters of the devices can be calculated using equation 2.28 and 2.29, respectively. Here, D^* is interpreted as the weakest level of light detected by the photodiode having a device junction area of 1 cm^2 and is determined by,

$$D^* = \frac{A^{1/2}R}{\sqrt{2qI_d}} \qquad 2.28$$

where, q and A are the elementary charge and the active junction area of the diode, respectively. The unit of $D^*$is $cmHz^{1/2}W^{-1}$ which is also called ″Jones″. D^* is usually used to compare the sensitivity limits of different photodiodes. Furthermore, NEP is the incident power required to obtain a signal-to-noise ratio of 1 at a bandwidth of 1 Hz and is described as following,

$$NEP = \frac{A^{1/2}}{D^*} = \frac{\sqrt{2qI_d}}{R} \qquad 2.29$$

NEP is expressed in a unit of $WHz^{-1/2}$. It is obvious from the equation 2.29 that the noise of a photodiode can be reduced simply by decreasing the active junction area of the device. Also, it can be referred to be reciprocal of D^*, normalized with respect to the junction area. Smaller NEP value corresponds to more sensitive photodiode whereas high value of D^* yields more sensitivity. The response speed of a photodiode is generally characterized by the rise time (t_r) and decay time (or fall time) (t_d). t_r is also known as the decay time that is defined as the time that the photocurrent rises from 10 % to 90 % of its maximum and t_d is also defined similarly.

2.3. Graphene

Graphene possesses several outstanding electronic and optical properties due to its extraordinary light absorbance of 2.3% despite being only 0.34 nm thick (Nair et al., 2008). Moreover, graphene is a broadband absorber covering the entire spectrum from ultraviolet to terahertz, which is a consequence of its linear dispersion relation and zero bandgap characteristic. In addition, graphene has high charge carrier mobility, large surface-to-volume ratio, tunable optical and electrical properties via electrostatic doping, and high sensitivity through adsorbates (Bolotin et al., 2008; Novoselov et al., 2005; Geim and Novoselov 2009; Mak et al., 2012). All these unique properties make graphene a potential candidate for technological applications such as imaging, sensing, communication and spectroscopy, chemical and biological sensors, photodetectors and solar cells.

2.3.1. Atomic Structure of Graphene

Graphene is the name given to single layer of graphite and consisting of sp^2-hybridized carbon atoms arranged in hexagonal honeycomb structure (Novoselov et al., 2005). Each of monolayer graphene in graphite is held together by the weak van der Waals bonds as depicted in Figure 2.12(a). Within an impeccable sheet of graphene, each of carbon atoms is connected to three neighboring atoms with covalent bonding.

In a graphene lattice, each carbon atoms comprises six atoms occupying atomic orbitals of $1s^2$, $2s^2$ and $2p^2$, where two of them are occupied the inner shell and do not contribute to conductivity. The remaining four electrons fill outer shell of 2*s* and 2*p* ($2p_x$, $2p_y$ and $2p_z$). As three orbitals *s*, p_x and p_y combine together, sp^2 hybridization occurs. Figure 2.12(b) shows the sp^2 hybridized orbitals of carbon atoms symmetrically distributed in the *xy*-plane at angle of 120° forming three σ-bonds. So, in the horizontal plane, each atom has a strong covalently bonded to the nearest three atoms with σ-bonds. These bonds are the reason behind the extraordinary mechanical robustness and elasticity of graphene. In Figure 2.12(c), the orbitals of the remaining p_z electrons lies perpendicular to the plane and they form the weak π-bonds which are responsible for electronic properties of graphene.

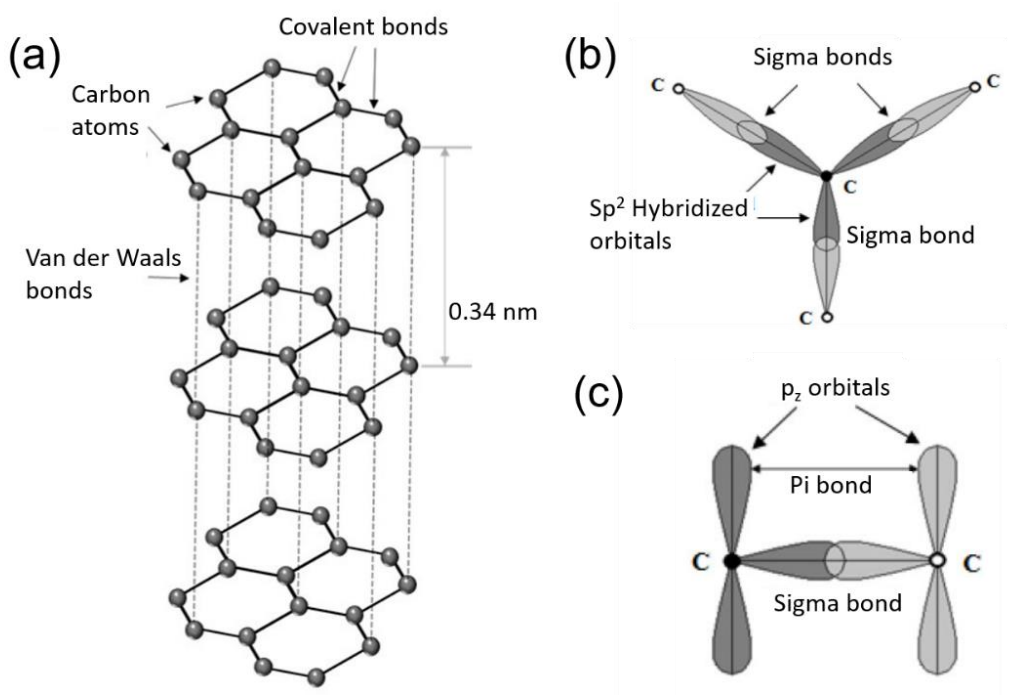

Figure 2.12. (a) Graphene layer held together by van der Waals forces in graphite. (b) In-plane bonds, sp^2 hybridized orbitals of carbon atoms symmetrically distributed in the molecular plane at angles of 120° forming three σ-bonds with those of the three nearest neighbors. (c) out of plane bonds, orbitals of the remaining electrons distributed perpendicular to the molecular plane form π-bonds with those of one of the nearest neighbor, assigning four bonds to each carbon atoms (Source: Dash, Pattanaik, and Behera 2014).

The hexagonal lattice structure of graphene including two carbon atoms of A and B per unit cell is shown in Figure 2.13(a). The real space lattice vectors of a_1 and a_2 can be written as following,

$$a_1 = a\left(\frac{3}{2}, \frac{\sqrt{3}}{2}\right), \qquad a_2 = a\left(\frac{3}{2}, \frac{-\sqrt{3}}{2}\right) \tag{2.30}$$

where a is the lattice constant with a value of 0.246 nm. The length between the nearest carbon atoms is equal to 0.142 nm. Figure 2.13(b) indicates the first Brillouin zone of graphene in reciprocal space defining with the lattice vectors of b_1 and b_2 :

$$b_1 = \frac{2\pi}{3a}\left(1, \sqrt{3}\right), \qquad b_2 = \frac{2\pi}{3a}\left(1, -\sqrt{3}\right) \tag{2.31}$$

In the first Brillion zone of graphene, Γ is the zone center, M is the midpoint, K and K' are two non-equivalent corners of first Brillouin zone, respectively. The corners K and K' which also named Dirac points are quite important for the physics of graphene. Their positions in momentum space are given by,

$$K = \frac{2\pi}{3a}\left(1, \frac{1}{\sqrt{3}}\right), \qquad K' = \frac{2\pi}{3a}\left(1, -\frac{1}{\sqrt{3}}\right) \tag{2.32}$$

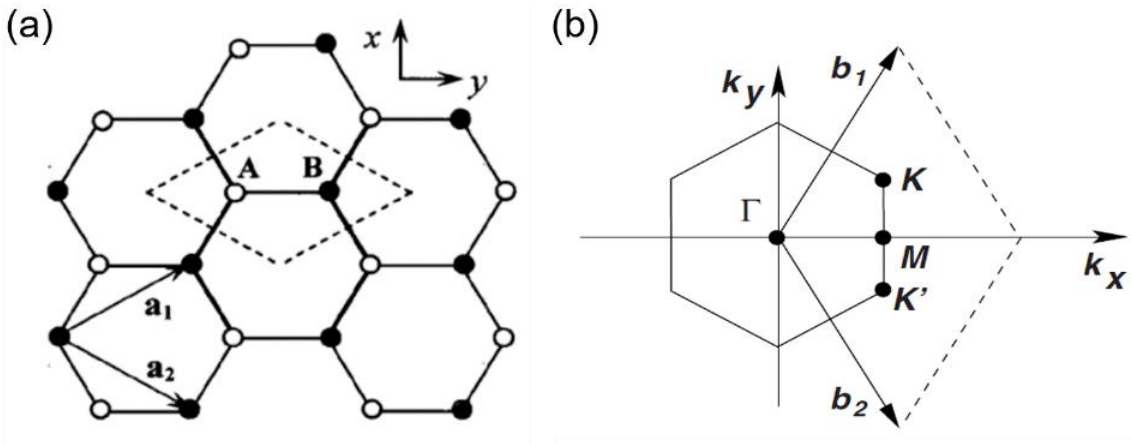

Figure 2.13. (a) Honeycomb lattice structure of graphene in real space with a basis of two atoms A and B. The unit cell results from two interpenetrating triangular lattices and is given with a dashed rhombus. (b) First Brillouin zone of graphene in momentum space (Source: Castro Neto et al., 2009).

2.3.2. Electrical Properties of Graphene

The electrical properties of graphene depend on π-electrons of the carbon atom. Graphene sheets with honeycomb structure is held together by the energy levels of π-bond orbitals in which π bonds with lower energy form the valence band and anti-bonding π^* electrons with higher energy form the conduction band. The cone-shaped conduction and valence bands touch each other at six highly symmetric K and K'points known as Dirac points in the hexagonal first Brillouin zone, as shown in Figure 2.14. Here, the z-axis represents the energy $E(k)$, with the xy-plane corresponding to the momentum $k = (k_x , k_y)$.

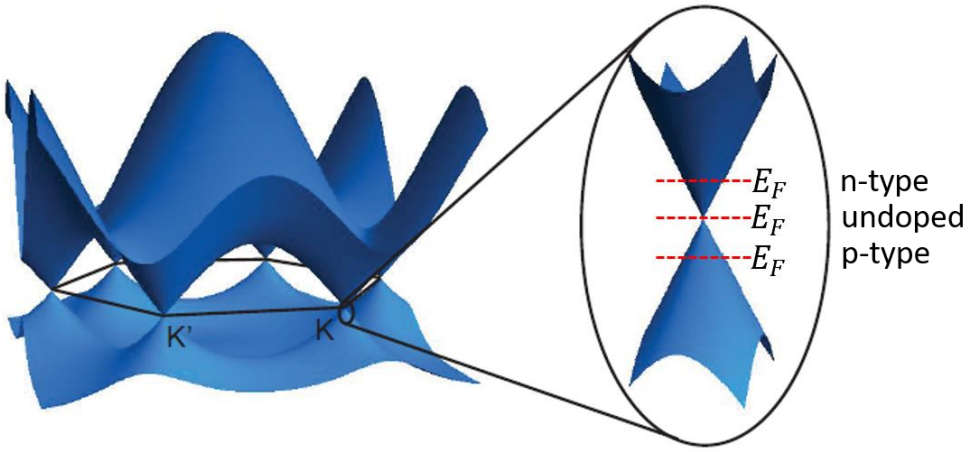

Figure 2.14. Electronic band structure of graphene obtaining from tight binding method. At the one corner of Brillouin zone, the up and down side of one Dirac point corresponds to conduction and valance band, respectively (Source: Molitor et al., 2011).

The electronic band structure of graphene can be determined using the tight-binding model (Reich et al., 2002). For monolayer graphene, valance and conduction bands do not overlap due to zero number of density of states. On the other hand, as the number of graphene layer increases, the band structure of the graphene deviates from the linear dispersion. By using tight binding approximation, the dispersion relationship of the massless π-electrons can be expressed as follows (Castro Neto et al., 2009),

$$E(k)^{\pm} = \pm\gamma\sqrt{1 + 4\cos\left(\frac{\sqrt{3}\,k_x\,a}{2}\right)\cos\left(\frac{k_y\,a}{2}\right) + 4\cos^2\left(\frac{k_y\,a}{2}\right)} \qquad 2.33$$

where γ is the nearest hopping energy that is nearly equal to 2.7 eV. The plus and minus signs refer to the upper and lower half-filled bands respectively. Further details on the band structure of graphene can be found in literature (Castro Neto et al., 2009; Molitor et al., 2011).

Conduction (π^*) and valence (π) bands of intrinsic monolayer graphene touch at the Dirac points (the energy of these points is fermi energy, E_F), so graphene is considered a semi-metal or zero-bandgap semiconductor. The energy dispersion around the Dirac points can be expressed as a linear equation (Das Sarma et al., 2011),

$$E(k)^{\pm} = \pm\hbar\,v_f\,|\mathbf{k}| = \pm\hbar\,v_f\sqrt{k_x^2 + k_y^2} \qquad 2.34$$

where $\hbar$ is the reduced Planck constant, k is the wave vector in spherical coordinates and v_f is the Fermi velocity. From there, the energy dispersion relation of graphene reveals linear behaviour around Dirac points with no energy gap. The fermi level of graphene is sensitive to external influences, such as electric fields, mechanical deformations, doping and adsorption. Under non-equilibrium conditions (applied electric fields) or extrinsic conditions (presence of impurity atoms), the E_F goes to upward or downward from its equilibrium value of 0 eV. (Philip Wong and Akinwande 2011).

2.3.3. Optical Properties of Graphene

Due to being only one atomic thick of 0.34 nm, graphene indicates remarkable optical properties. A single layer of graphene absorbs a mere 2.3% of incident light with a very broad wavelength range from ultraviolet (UV) to terahertz (THz). This is a result of its gapless and linear dispersion relation behavior. The optical transmittance (T') of monolayer graphene can be determined by the following Taylor expansion (Bonaccorso et al., 2010; Bao and Loh 2012),

$$T' = \frac{1}{\left(1 + \frac{\alpha\pi}{2}\right)^2} \approx 1 - \alpha\pi \approx 97.7\% \qquad 2.35$$

where $\alpha = e^2/\hbar c \approx 1/137$ is the fine structure constant. Here, it is obvious that there is no dependence with frequency and any other physical material properties. In addition, graphene only reflects < 0.1% of the incident light in the visible region (Nair et al., 2008). The absorption of few-layer graphene can be roughly estimated by scaling the number of layers ($T' \approx 1 - N\alpha\pi$) (Bao and Loh 2012).

Although the absorption spectrum of graphene is nearly immutable at the wavelength from 300 nm to 2500 nm due to linear band structure of graphene at low energies, it can be seen a slight deviation from $\pi\alpha$ absorption at the higher frequencies arising from the nonlinearities in the band structure (Kravets et al., 2010). The optical absorption of graphene supplies from two kinds of processes involving interband and intraband transitions. The intraband transitions exists at low photon energies (from far-infrared to THz), on the other hand interband transitions dominates at higher photon

energies such as in MIR and UV spectral region. For intraband transition, optical absorbance is supplied from free carrier in graphene and can be described by Drude model for the frequency-dependent sheet conductivity as following equation (Mak et al., 2012),

$$\sigma(\omega) = \frac{\sigma_0}{1 + i\omega\tau} \qquad 2.36$$

where σ_0 and τ are the dc conductivity and the electron scattering time, respectively, and ω refers to the angular frequency of light. Interband transition defines optical response of graphene at higher frequencies which is the direct transitions of photoexcited electrons from valance band to conduction band. For example, the optical conductivity of a pristine graphene at zero temperature is found to be a frequency-independent and determined by the fundamental constants and approach to a value of $\sigma(\omega) = \pi e^2/2h$. This conductivity corresponds to a fixed absorbance of $A(\omega) = (4\pi/c)\sigma(\omega) = \pi\alpha \approx 2.3\%$ (Nair et al., 2008; Mak et al., 2012).

Transparent electrodes are widely used in many optoelectronic devices such as photodetectors and solar cells. As an example, Indium Tin Oxide (ITO) is frequently used in such devices, with a transmittance of around 80% (Bonaccorso et al., 2010). It is therefore obvious that monolayer graphene layer with a transparency of 97.7% has a clear advantage over ITO. Nowadays, graphene is an alternative transparent material to fabricate next-generation optical devices.

2.3.4. Production of Graphene

High quality graphene has a crucial importance for electronic and optoelectronic devices. Various methods have been utilized to reach this goal. Commonly employed graphene production methods are classified by i) mechanical exfoliation, ii) thermal decomposition of Silicon Carbide (SiC) and iii) chemical vapor deposition (CVD). The methods are selected depending on where and on which devices the graphene will be used. Also, all the techniques have some advantages and drawbacks in terms of production, cost and yield etc. Each of these methods will be discussed in detail below.

2.3.4.1. Mechanical Exfoliation

In graphite, graphene layers are hold together by weak van der Waals interaction. Therefore, individual graphene sheets can be separated from the graphite by breaking these weak bonds. Mechanical exfoliation is the most preferred technique to produce high quality graphene. In this technique, single or a few-layer graphene can be peeled off from highly ordered pyrolytic graphite (HOPG) flakes by using a scotch tape. This provides pure graphene layers without defects and dopant among all other methods. Graphene on the adhesive tape is easily transferred onto SiO_2/Si substrate by slightly pressing and then graphene layers can be observed with color contrast under optical microscope. Even though mechanical exfoliation produces a high quality graphene it has some drawbacks such as irregular shape, low yield and poor throughput. So, graphene produced with this method is not feasible to the industrial applications.

Figure 2.15(a) and (b) show the optical image of graphene transferred by mechanical exfoliation onto Si wafer with 300 nm thick of SiO_2 under a white light and green light, respectively. Trace in the figure shows the changes in the contrast, which corresponds to different graphene layers. Here, lightest color on the substrate indicates single layer graphene whereas the other flakes with increasing darkness corresponds to few or multilayer graphene (Blake et al., 2007).

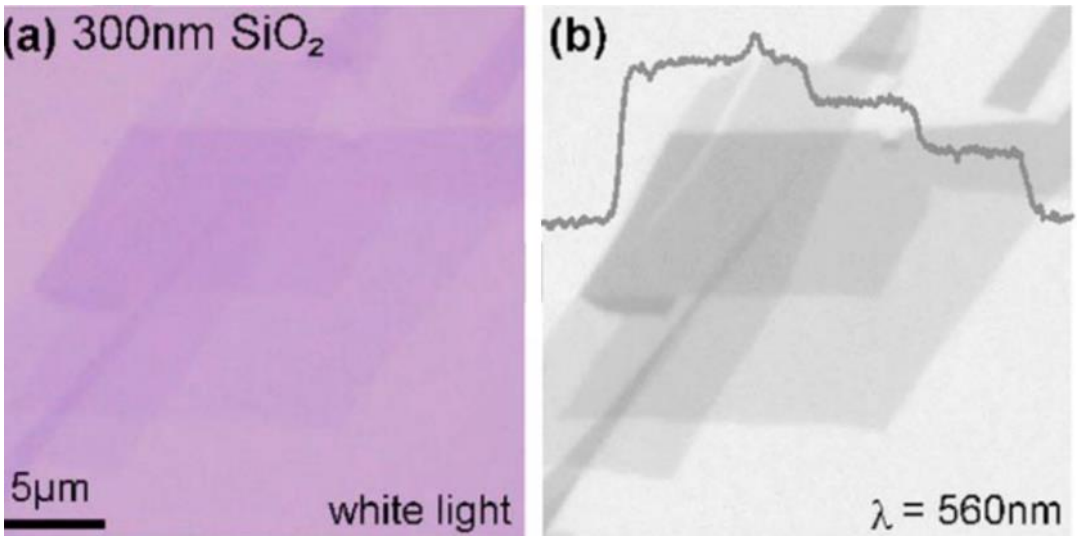

Figure 2.15. Optical image of exfoliated graphene transferred on SiO_2/Si substrate under white and green light illumination (Source: Blake et al., 2007).

2.3.4.2. Thermal Decomposition of SiC

Graphene layers can be formed by heating the SiC substrate at high temperatures (above 1000 °C) in ultra-high vacuum (UHV) environmental, which is causing sublimation of Si atoms and thereby graphitization of remaining C atoms on the surface. Due to being bipolar of SiC, graphene can be grown on both faces of 4H-SiC or 6H-SiC wafers including the Si-terminated face (0001) and C-terminated face (000-1). Grown graphene layers on these two faces have different growth rates and electronic properties.

Graphene can be grown by a low growth rate on the Si-terminated face of SiC (De Heer et al., 2011). By controlling the growth parameters such as annealing temperature and time, single or a few-layers graphene sheets on the SiC (0001) can be formed on the wafer (Mishra et al., 2016). On the other hand, graphene forms much faster on the C-terminated face (000-1) surface than on the silicon-terminated face (0001), occurring high graphene layers at 5 layers and above. But, the number of layers can be controlled by the capping method (Çelebi et al., 2012). Here, the surface of C-terminated face SiC is capped by another SiC sample with Si-terminated face in order to reduce high growth rate of graphene. Graphene growth on SiC by thermal decomposition is very promising for semiconducting industry due to its scalability, good electronic properties and especially its high-quality of graphene. However, this method has its own drawbacks. For example, synthesized epitaxial graphene on SiC although had high quality, they could not be transferred on other substrates.

2.3.4.3. Chemical Vapor Deposition

The most commonly used graphene growth method is Chemical Vapor Deposition (CVD), which comprises chemical reaction of a vapor near or at heated surface. This technique provides high quality single-layer graphene with large scale. A typical CVD system contains a transition metal foil, supply of carbon containing gas (e.g., methane or ethylene) and a reaction chamber that can function up to 1200 °C. In the CVD method, gas precursor like hydrocarbon is used as carbon source which reacts with metal catalysts at high temperatures (around 1000 °C). Figure 2.16 demonstrates the schematic illustration of typical CVD grown graphene process under gas mixture of CH_4/H_2. Graphene growth by CVD technique on a transition metal consists of nine main

steps: (1) Reactants are transported by forced convection, (2) thermal activation, (3) transport of reactants by diffusion of gas, (4) reactants are adsorbed on the substrate surface, (5) bulk diffusion occurs in the substrate, (6) thermal activation and surface processes including chemical decomposition and reaction occurs growth of graphene, (7) by-products are desorbed from the surface, (8) transportation of by-products occurs by diffusion through the boundary layer and return to the main gas stream, (9) carrying of by-products away from the deposition region via forced convection.

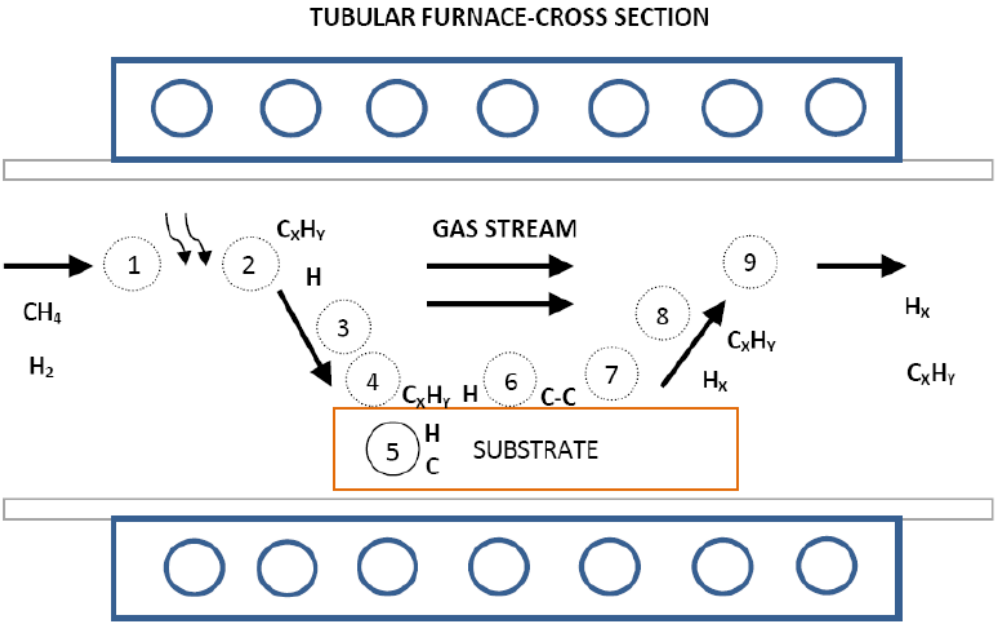

Figure 2.16. Schematic diagram of thermal CVD grown graphene under CH_4/H_2 gas mixture (Source: Muñoz and Gómez-Aleixandre 2013).

Transition metals such as Copper (Cu) (Xuesong Li et al., 2009), Nickel (Ni) (K. S. Kim et al., 2009), Palladium (Pd) (Murata et al., 2012), and Ruthenium (Ru) (Loginova et al., 2009) foils or films have been utilized as catalysts in graphene growth. Among those, the most commonly used transition metals are Cu and Ni. Compare to Ni, Cu has very low solubility of carbon, which is the key parameter to control number of graphene layers. As a result of low solubility, Cu and carbon generate weak bond by means of charge transfer from the π electrons in the sp^2–hybridized carbon to empty 4s states of Cu (Muñoz and Gómez-Aleixandre 2013). This combination of very low affinity between carbon and copper could make easy graphitic carbon formation. The CVD method has many controllable parameters that result in synthesis of large size graphene up to 30 inches (Bae et al., 2010).

2.4. Graphene/Semiconductor Schottky Junction Photodiodes

Due to high carrier mobility and inherently excellent optical transparency of graphene, it has become a preferred material to be used as a transparent conductive electrode instead of metals in MS Schottky junction. It is known that graphene is a semimetal in which valance and conduction bands meet each other at Dirac point and shows linear dispersion relation (Castro Neto et al., 2009). In this section, the characteristics of graphene/semiconductor (Gr/Sc) Schottky junctions will be presented in detail.

Tongay et. al have reported that when CVD grown graphene layers is placed onto lightly doped semiconductor materials such as Si, GaAs, SiC and GaN, the strong rectifying character forms at the interfaces of them as depicted in Figure 2.17 (Tongay et al., 2012). From the forward bias of J-V plots in semi-logarithmic scale illustrated in the inset of Figure 2.17, the Schottky barrier heights of such diodes were extracted to be 0.86, 0.79, 0.91 and 0.73 eV for the junctions built on Si, GaAs, SiC and GaN, respectively. They also showed that the fermi level of graphene in such Gr/Sc heterojunction is varied with respect to applied bias voltage due to charge transfer at the interface. In conventional MS junction, the fermi level of metal is not affected by the charge transfer at the junction due to high density of states. However, charge transfer (or doping) in Gr/Sc junction modifies the work function of graphene (Castro Neto et al., 2009), leading the variation of the Schottky barrier height.

Figure 2.18 shows the energy band diagram of graphene/n-type semiconductor (Gr/n-Sc) Schottky junction at zero bias, under forward and reverse bias conditions. When graphene gets in contact with a lightly doped n-type semiconductor, Schottky barrier height and depletion region are formed at the interface as soon as the junction reaches the thermal equilibrium. It was assumed that graphene's fermi level is at the Dirac point under zero bias. In thermal equilibrium, whereas the depletion region formed inside n-Sc fills with holes, an equal amount of electrons is induced in graphene. When the forward bias is applied to the diode as shown in Figure 2.18(b), fermi level of graphene shifts below the Dirac point due to the reduction of number of induced electron in graphene. Thus, the width of depletion region decreases, whereas the Schottky barrier height increases proportional to the decrement in fermi level of graphene. On the other hand, under reverse bias condition (see Fig. 2.18(c)), graphene is

doped with electrons, so the fermi level of graphene shifts above the Dirac point, leading to a decrease of the Schottky barrier height and a rise in the depletion region.

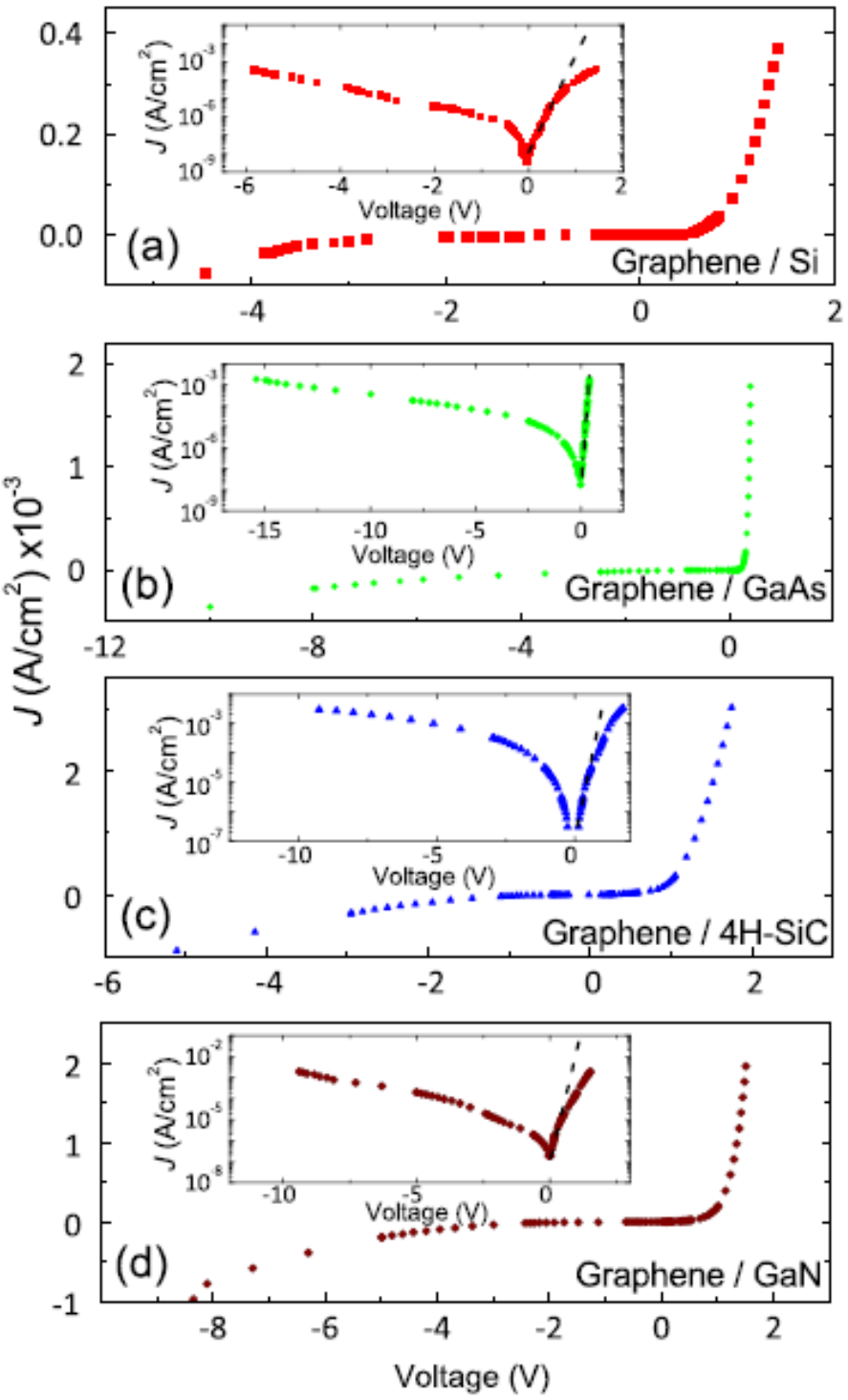

Figure 2.17. Current density-voltage (J-V) plots showing a clear Schottky rectifying character at the interface of graphene/Si, graphene/GaAs, graphene/SiC and graphene/GaN, respectively. Inset: J-V plots in semi-logarithmic scale (Source: Tongay et al., 2012).

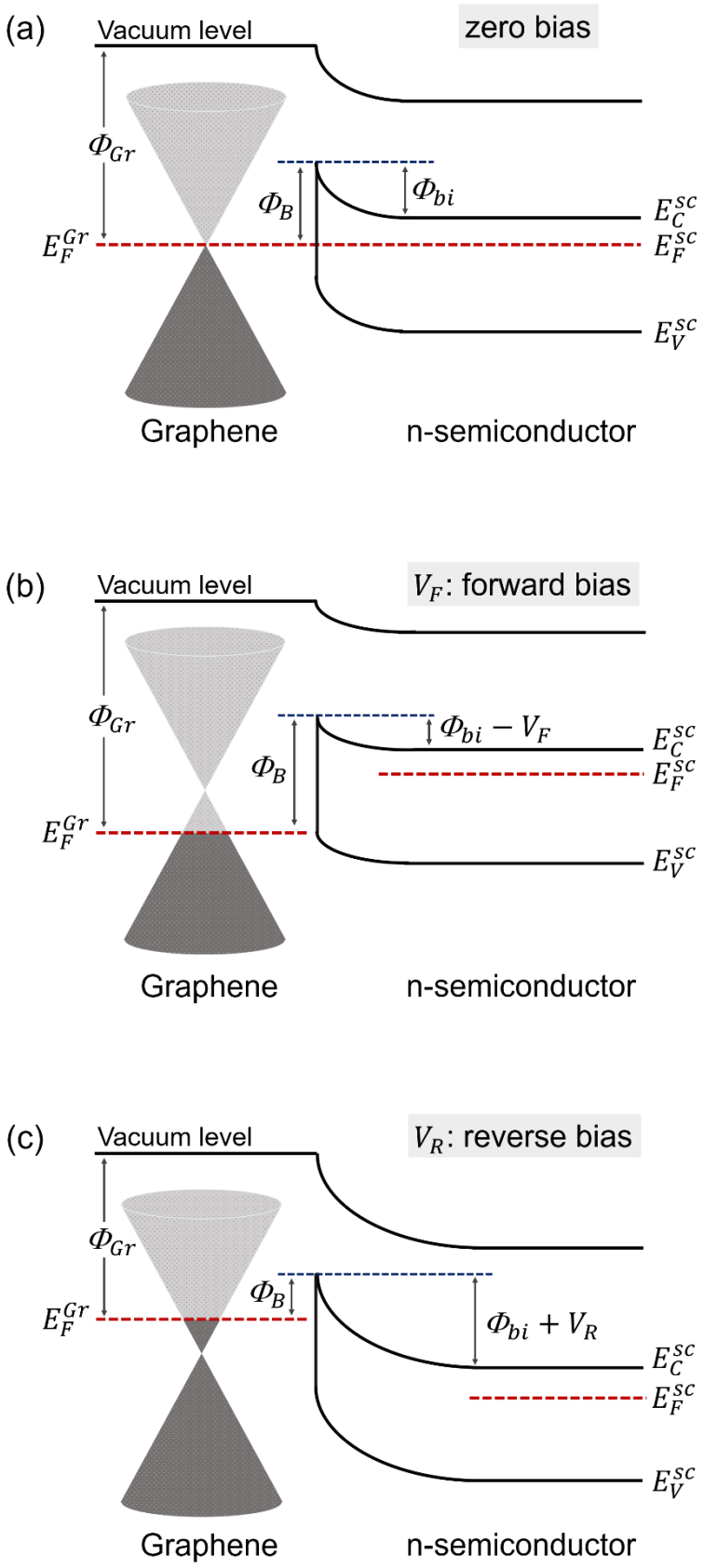

Figure 2.18. Energy band diagram of a graphene/n-type semiconductor Schottky junction (a) at zero bias, under (b) forward and (b) reverse bias voltages.

As mentioned above, by considering the bias dependent alteration of graphene's fermi level in Gr/Sc Schottky junction, a simple modification in the thermionic emission model was done by S. Tongay (Tongay et al., 2012). In order to determine the shift in fermi level of graphene as a function of applied reverse bias voltage, it can be considered that the induced charge density on graphene per unit area is expressed as,

$$Q = qn_{ind.} = C_{dep.}(\Phi_{bi} + V_r) \tag{2.37}$$

where,

$$C_{dep.} = \sqrt{\frac{q\varepsilon_0\varepsilon_r N_d}{2(\Phi_{bi} + V_r)}} \tag{2.38}$$

is the magnitude of capacitance at the depletion region, $n_{ind.}$ is the number of induced electron per unit area and V_r is the magnitude of the applied reverse bias voltage. Combining eqn. (2.37) and eqn. (2.38), the number of charge carriers at the depletion region is given by the equation below,

$$n_{ind.} = \sqrt{\frac{\varepsilon_0\varepsilon_r N_d(\Phi_{bi} + V_r)}{2q}} \tag{2.39}$$

Before graphene does not built on semiconductor, we also need to take into account the initial doping level of graphene, which is described as

$$n_{final} = n_0 - n_{ind.} \tag{2.40}$$

So, the fermi level of graphene can be calculated as,

$$E_F = -\hbar|v_F|k_F = -\hbar|v_F|\sqrt{\pi(n_0 - n_{ind.})} \tag{2.41}$$

Inserting eqn. (2.39) into eqn. (2.41), the fermi level of graphene can be associated with the built-in potential and applied reverse bias as expressed by the equation below,

$$E_F = -\hbar|v_F|\sqrt{\pi\left(n_0 - \sqrt{\frac{\varepsilon_0\varepsilon_r N_d(\Phi_{bi}+V_r)}{2q}}\right)} \qquad 2.42$$

This equation can be utilized to estimate the shift of fermi level of graphene by taking into account the constant values such as: $\hbar = 6.65\times10^{-16}\,eV\,s$, $q = 1.6\times10^{-19}\,C$, $v_F = 1.1\times10^{8}\,cms^{-1}$, $\Phi_{bi}\approx 0.6\,V$, $\varepsilon_0 = 8.84\times10^{-14}Fcm^{-2}$ and ε_r equals about 10 for a typical semiconductor.

The bias voltage dependent Schottky barrier height described by S. Tongay can be given as,

$$q\Phi_B = q\Phi_B^0 + q\Delta\Phi_B(V) = q\Phi_B^0 - \Delta E_F(V) \qquad 2.43$$

where $q\Phi_B^0$ is the Schottky barrier height at zero bias and $q\Delta\Phi_B(V)$ is the barrier height at fixed bias voltage. The amount of alteration in Schottky barrier height from applied reverse bias voltage would be equal to the change in the fermi level of graphene.

$$q\Delta\Phi_B(V) = -\Delta E_F(V) \qquad 2.44$$

For reverse bias, by using both eqn. (2.42) and inequality of $n_{ind.} \ll n_0$, the variation in the Schottky barrier height can be calculated as,

$$\begin{aligned} q\Delta\Phi_B(V_r) &= -\Delta E_F(V_r) \\ &= -\hbar|v_F|\left[\sqrt{\pi(n_0 - n_{ind.})} - \sqrt{\pi n_0}\right] \\ &\approx -\frac{1}{2}\hbar v_F\sqrt{\pi n_0}\frac{n_{ind.}}{n_0} \\ &= -\frac{1}{2}\hbar v_F\sqrt{\frac{\pi\varepsilon_0\varepsilon_r N_d(\Phi_{bi}+V_r)}{2qn_0}} \end{aligned} \qquad 2.45$$

In conventional MS junction, the saturation current density is given by the following equation.

$$J_0 = A^* T^2 exp\left(\frac{-q\Phi_B^0}{k_B T}\right) \quad 2.46$$

In Gr/Sc Schottky junction, the height of Schottky barrier is modified with applied bias voltage. Thereby, the saturation current density is written as,

$$J_0 = A^* T^2 exp\left(-\frac{q\Phi_B^0 + q\Delta\Phi_B(V)}{k_B T}\right) \quad 2.47$$

The total current density flowing over Gr/Sc junction is expressed as below.

$$J(V) = A^* T^2 exp\left(-\frac{q\Phi_B^0 + q\Delta\Phi_B(V)}{k_B T}\right)\left[exp\left(\frac{qV}{k_B T} - 1\right)\right] \quad 2.48$$

Since the main focus of this thesis is on the performance enhancement of graphene/n-type silicon (Gr/n-Si) Schottky junction photodiodes, a more detail related to such diodes is given below.

2.4.1. Graphene/Silicon (Gr/Si) Schottky junction photodiodes

Graphene/silicon (Gr/Si) Schottky photodiode can be produced when graphene is coupled with lightly doped n-type Si (n-Si) substrate, where graphene is employed not only as a transparent conductive electrode but also functions as a photo-active material due to its ~2.3 % optical absorption. The spectral response of the junction is determined by the band gap of silicon, which is sensitive to light in the visible and short wavelength infrared spectral range.

Many studies have been conducted to fabricate and to improve the performance of Gr/Si based Schottky junction photodiodes. Chen et. al. (Chen et al., 2011b) revealed the Schottky rectifying behavior of the junction occurred by depositing mechanically exfoliated graphene on Si substrate. A schematic diagram of the fabricated photodiode is illustrated in Figure 2.19(a). The I-V characteristic of this diode in dark and under illumination is shown in Figure 2.19(b). It is obvious that the device shows a clear Schottky rectifying behavior. The photocurrent and open circuit voltage can be clearly

seen from the I-V curve plotted in semi-logarithmic scale. Based on light illumination, an increase in the current occurs when the applied voltage is equal to zero, indicating photocurrent generation. In addition, the voltage difference seen in horizontal scale corresponds to open circuit voltage (V_{oc}).

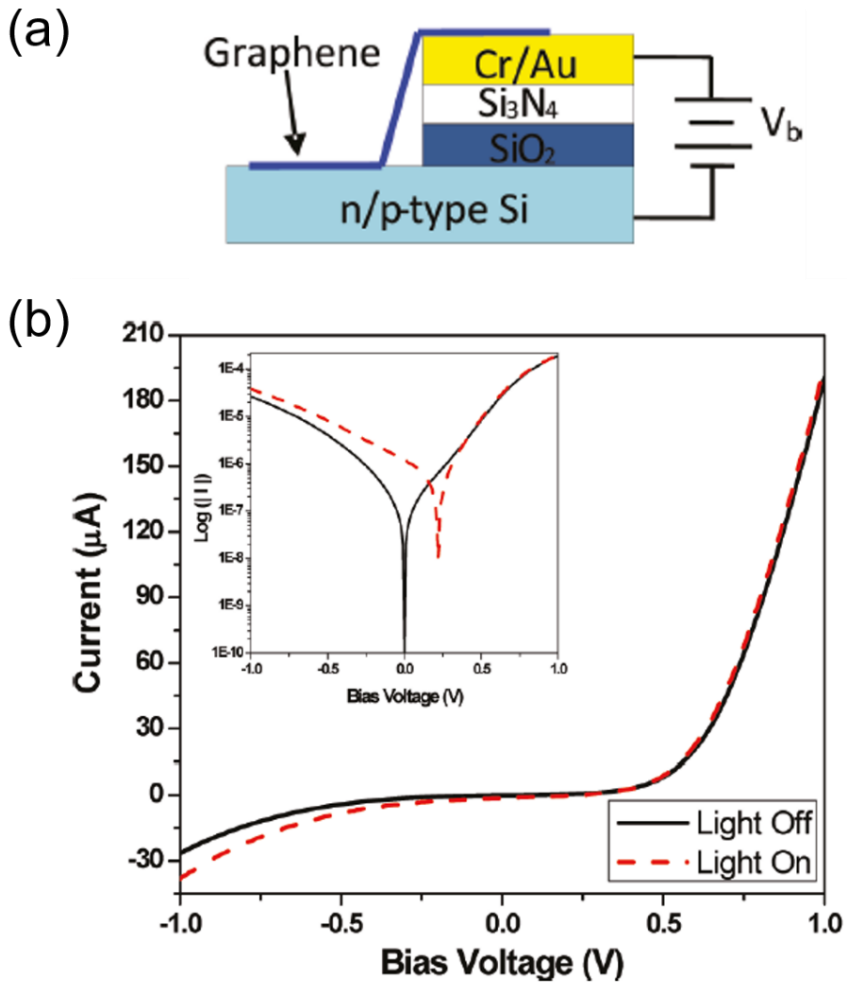

Figure 2.19. (a) Schematic diagram of a Gr/n-Si Schottky photodiode. (b) The I-V characteristics of Gr/Si based Schottky photodiode in dark and under illumination. The inset shows I-V plot in semi-logarithmic scale (Source: Chen et al., 2011b).

In a subsequent study, Li et. al. (Xinming Li et al., 2010) demonstrated the rectifying behavior of Schottky junction formed by transferring CVD graphene on top of n-Si substrate. The fabricated device exhibited photovoltaic properties under light illumination.

Another study on Gr/n-Si photodiodes was done by Riazimehr et. al. (Riazimehr et al., 2017), who characterized the spectral response of the diode under light illumination in a wide range of wavelength between 360 nm and 2000 nm. Figure 2.20(a) shows the schematic illustration of the fabricated Gr/n-Si Schottky junction photodiode. One end of the graphene lies on the n-Si surface without touching the metal electrodes deposited on the n-Si, forming Schottky junction. The other end is placed on the Cr/Au pad which was deposited on the SiO_2 layer. Figure 2.20(b) demonstrates the spectral response measurements with a wide range wavelength from 360 nm to 1800 nm under different bias voltages on the Gr/n-Si photodiode. It was found that the spectral responsivity is increased with applied bias due to the increased electric field. They measured that the responsivity of the device is reaching a maximum value of 0.27 AW^{-1} at a reverse bias of – 2 V. This maximum is observed at the peak wavelength of 940 nm and then exhibited a downward trend towards to wavelength of 1100 nm due to the band edge of n-Si substrate.

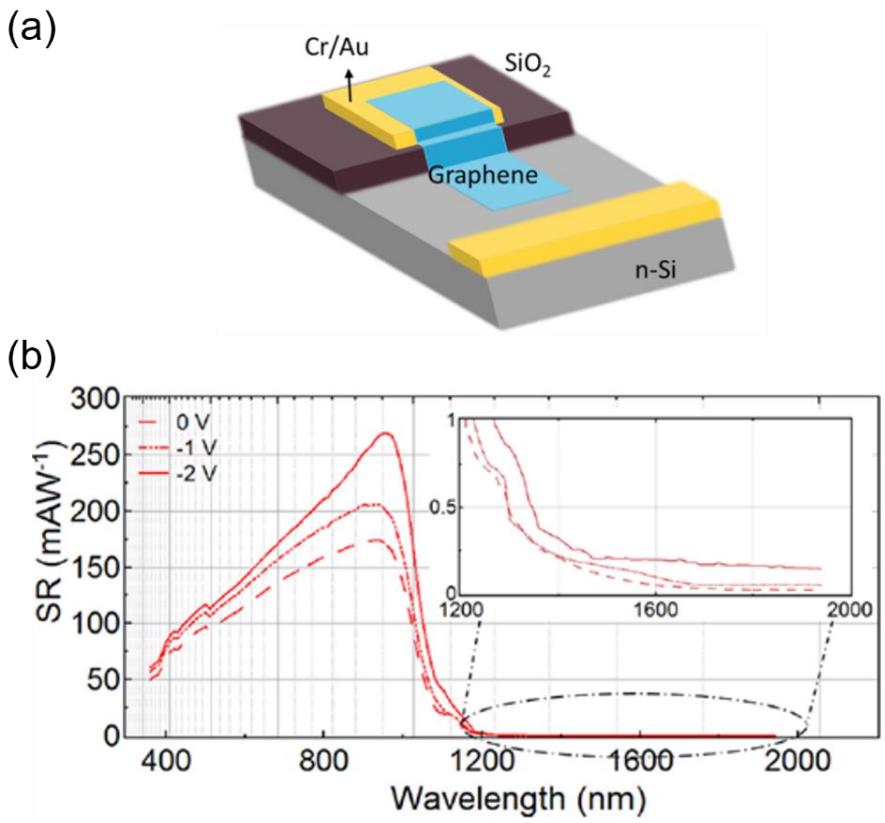

Figure 2.20. (a) Schematic illustration of a Gr/n-Si Schottky photodiode in a basic architecture. Spectral response vs wavelength of Gr/n-Si photodiode over a broad spectrum (from 360 nm to 2000 nm) at zero bias and reverse biases of – 1 V and – 2 V (Source: Riazimehr et al., 2017).

In another study, C. Wang et.al. (C. Wang et al., 2019) showed a high speed self-powered Gr/Si based Schottky junction photodiode operating under pulsed light frequency of 10 kHz at 1550 nm. Rise time and decay time of the device have been determined to be 12 μs and 40 μs as extracted from the one cycle photo-response measurement, respectively. (see Figure 2.21).

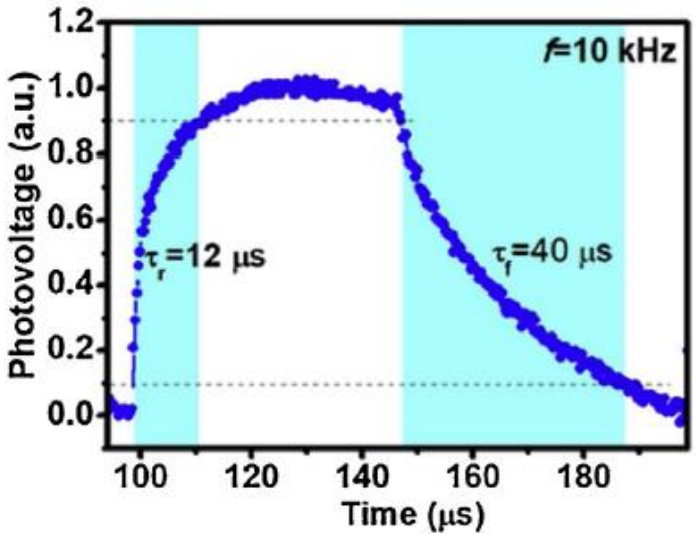

Figure 2.21. One cycle time-dependent photo-response measurement of Gr/n-Si photodiode under fast varied light illumination of 1550 nm wavelength light with a switching frequency of 10 kHz (Source: C. Wang et al., 2019).

Table 2.2 lists some of the performance parameters for Gr/n-Si based Schottky photodiodes. It has been shown that a Schottky barrier height in an energy range between 0.7 – 1.0 eV has been identified for the heterojunction of CVD graphene with n-Si substrate and as well as some surface modification of graphene and/or the thin oxide layer inserted into interface of them. Most of the researchers constructed Gr/Si based Schottky photodiodes with different device designs for enhancing their photo-response performance. Their photodiode characteristics were found to vary substantially depending on the doping level of Gr layer and/or of n-Si substrate underneath and as well as on the presence/absence of an oxide layer at their interface. For example, Aydin et. al. (Aydin et al., 2018) showed that the maximum responsivity of Gr/n-Si Schottky photodiodes can be increased from 0.24 AW^{-1} to 0.78 AW^{-1} when Gr electrode is coated with P3HT polymer molecules. Li et al., (Xinming Li et al., 2016) reported that the sensitivity of Gr/n-Si Schottky junction photodiodes can be improved with a thin

interfacial oxide layer between Gr electrode and n-Si substrate due to reduced dark current. In a subsequent work, Bartolomeo et. al. (Di Bartolomeo et al., 2017) showed a novel Gr/n-Si diode with a high responsivity value of 3 AW^{-1} as a result of utilizing graphene on nanotip patterned onto n-Si substrate.

Table 2.2. Summary of the performances of Gr/n-Si based Schottky photodiodes

Device structure	Φ_B (eV)	*Max., R* (AW^{-1})	(t_r / t_d) (μs)	References
Gr/n-Si	-	0.029	93 / 110	(Lv et al., 2013)
Gr/n-Si	0.79	0.040	12 / 40	(C. Wang et al., 2019)
Gr/n-Si	0.76	0.51	130 / 135	(Periyanagounder et al., 2018)
Gr/n-Si	1.01	0.73	-	(Y. Wang, Yang, Ballesio, et al., 2020)
Gr/n-Si	0.80	0.44	1200 / 3000	(An et al., 2013)
Gr/GO/n-Si	0.91	0.65	-	(Y. Wang, Yang, Lambada, et al., 2020)
Gr/SiO_2/n-Si	-	0.73	320 / 750	(Xinming Li et al., 2016)
P3HT Gr/n-Si	-	0.78	-	(Aydin et al., 2018)
MoO_3 Gr/n-Si	0.86	0.40	-	(Xiang et al., 2015)
TFSA Gr/n-Si	0.89	0.25	-	(Miao et al., 2012)
SiNH arrays Gr/n-Si	0.82	0.33	25 / 56	(Zeng et al., 2015)

CHAPTER 3

EXPERIMENTAL METHODS

3.1. Device Fabrication

3.1.1. Chemical Vapor Deposition (CVD) of Graphene

Chemical vapor deposition (CVD) stands the most widely used technique in order to synthesize 2D graphene sheet since it offers many advantages such as high purity, high uniformity, low defects and low cost (Saeed et al., 2020).

In our laboratory, for the graphene growth process by CVD technique, high purity copper (Cu) foils (*25 μm thick, purchased from Alfa Aesar)* used as catalyst substrate material were cut into small pieces. Then the Cu foils placed on a quartz slide was loaded into the tube furnace (Lindberg/Blue TF55035C Split Mini Tube) of CVD system at atmospheric pressure as shown in Figure 3.1.

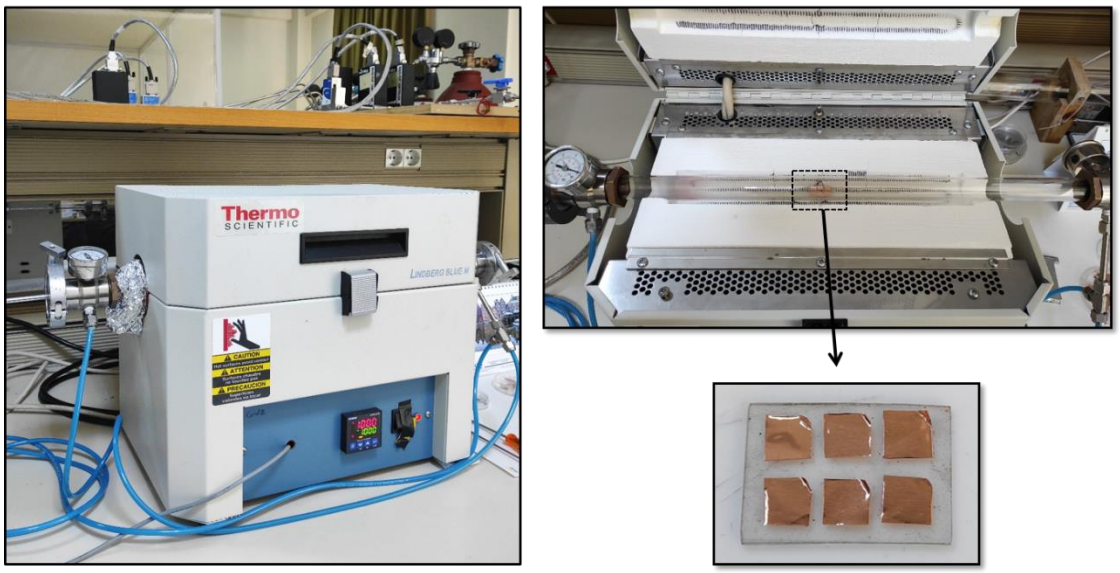

Figure 3.1. The experimental setup for CVD graphene growth in our laboratory contains a furnace with quartz tube, thermocouple and mass flow meter. The Cu foils placed on a quartz slide are inserted into quartz tube.

The representative graph on graphene growth process via CVD involving heating, annealing, growing and cooling in the four steps was depicted in Figure 3.2. After loaded the Cu foils into furnace, the chamber was first pumped down to its base vacuum level. As for the first step, the Cu foils inside the quartz tube was heated up to 1000 °C under the flow of H_2 (20 sccm) and Ar (1000 sccm) gas mixture with a temperature ramp rate of 30 °C min^{-1}. Subsequently, the samples were annealed for 59 min. under the same temperature and gas flow rates. This provides both removing of the native oxide layer on the Cu foil and forming of (111) oriented grain boundaries. Following the annealing process, CH_4 (10 sccm) gas was delivered into the tube furnace for 2 min. in order to grow the graphene layer on Cu foils. Finally, the tube was left for cooling down to room temperature under gas flows of H_2 (20 sccm) and Ar (1000 sccm). After the temperature of the furnace reached nearly 100 °C, the samples was put off from the furnace and then Microposit S1318 Photoresist (PR) used supporting layer was drop casted on the Graphene/Cu and the stack was annealed at 70 °C overnight in an oven.

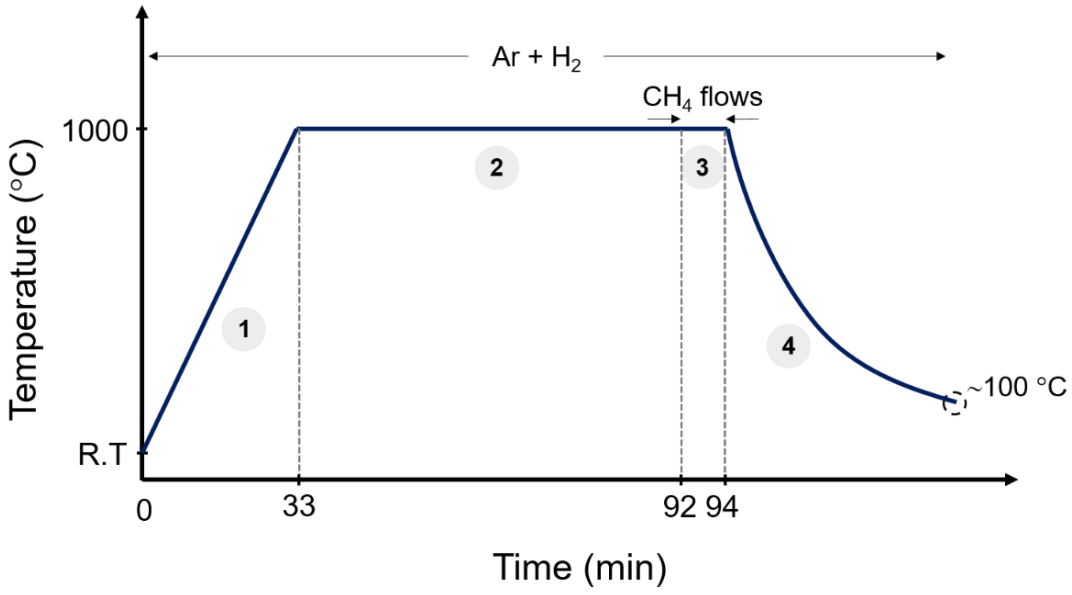

Figure 3.2. Schematic representation of temperature-time plot for the growth of monolayer graphene on Cu foil, the process includes (1) heating, (2) annealing, (3) growth and (4) cooling, respectively. R.T is the room temperature.

3.1.2. Deposition of SiO_2 and Cr/Au by Thermal Evaporation System

A commercial Si wafer (n-type, resistivity of ρ = 1-5 Ω.cm) was utilized as the substrate for the fabrication of Gr/n-Si based Schottky junction photodiodes. The wafer has a crystal orientation of (100) and its surface covered with native oxide grown in air. The n-Si wafer was diced into 10 mm × 10 mm square pieces and was ultrasonically cleaned for 10 min. in acetone, isopropanol (IPA) and deionized (DI) water, respectively. After the native oxide on the n-Si substrates was etched away by 6 % diluted hydrofluoric acid (HF) in 3-5 seconds, the substrates were immediately loaded into thermal evaporation system to deposit silicon dioxide (SiO_2) dielectric layer and then chromium/gold (Cr/Au) metallic contact pads. This is an important process for ensuring good electrical contact on n-Si substrate, before the deposition of Cr/Au contact pads and graphene transfer.

Figure 3.3. The NVTH-350 thermal evaporation system in quantum device laboratory. The chamber includes (1) tungsten wire basket for evaporation of SiO, (2) chromium plated tungsten rod, (3) tungsten boat for evaporation of Au, (4) substrates placed in the sample holder are held inverted at the top of the vacuum chamber.

Figure 3.3 shows thermal evaporation system in quantum device laboratory. It is one of the easiest method to deposit evaporation materials on the surface of substrate in high vacuum environment. In this work, silicon monoxide (SiO), Cr and Au were used as evaporation materials. These are thermally contacted with tungsten (W), so when W is heated, the materials are heated up, too. The SiO pellets sized with 3-5 mm were filled into W wire basket for the sublimation. To gain desired device geometry, hard metallic masks were designed in AutoCAD and manufactured by Sparks Technologies-Turkey by laser cutting system. By using these metallic masks, 400 nm thick SiO_2 dielectric layer was first evaporated to cover a portion of the surface of n-Si substrate. Subsequently, Cr/Au (4 nm/80 nm) metal contact pads were deposited both on the n-Si side and on the SiO_2 covered side of the substrate by using the cromium plated tungsten rod and high purity Au pieces, respectively. Here, 4 nm Cr was used to increase the stickiness of the gold to the substrate before vaporization of gold.

3.1.3. Graphene Transfer

Figure 3.4 demonstrates the fabrication stages of Gr/n-Si photodiode after growth of graphene on Cu foil. As mentioned before, after graphene was grown on the Cu foil by using the CVD method described in section 3.1.1, photoresist as a supportive layer was applied to the graphene on Cu foil and annealed at 70 °C overnight. Thereafter, the Cu foil at the bottom was fully etched using Iron chloride ($FeCl_3$) solution to get suspend photoresist/Gr bilayer. After rinsed by using DI water and then a mixture of H_2O:HCl (3:1) for the removal of $FeCl_3$ residues, the photoresist/Gr became ready for transferring onto the surface of n-Si substrate (see Fig. 3.4(a)).

After finished the deposition of SiO_2 dielectric layer and Cr/Au metallic pads (see Fig. 3.4(b)), the photoresist/Gr was annealed at a temperature of 100 °C for 5 min. in order to provide better adhesion of the graphene layer on the surface of n-Si substrate. One end of the graphene lies on the n-Si surface without touching the metal electrodes deposited on the n-Si, forming the Schottky junction and the other end is contacted with a Cr/Au pad on SiO_2 layer which insulates a direct contact between the metal electrode and the n-Si substrate. After the transfer of graphene electrode, the supporting photoresist layer was removed by acetone, followed by rinsing with IPA and DI water and drying it with nitrogen.

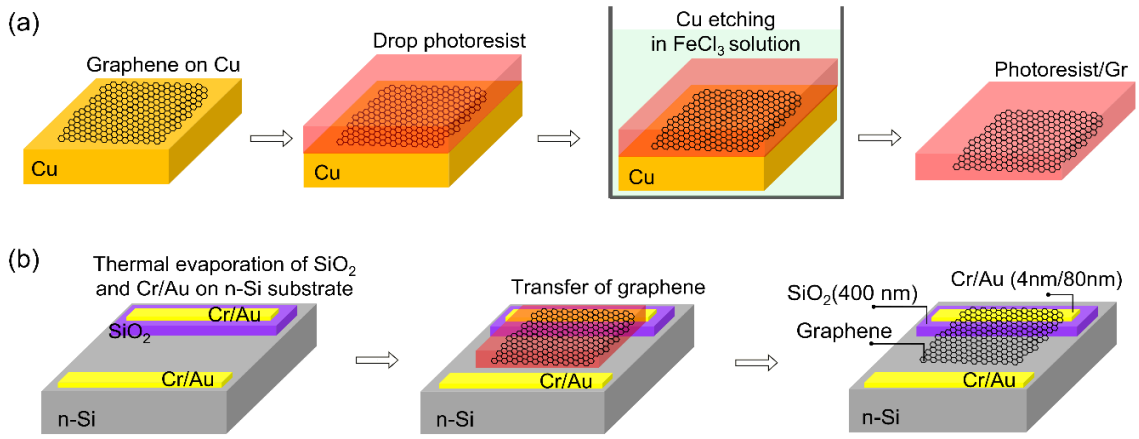

Figure 3.4. (a) Schematic illustration of CVD graphene growth on Cu foil and its transfer preparation onto n-Si substrate, (b) SiO_2 and Cr/Au deposition onto n-Si substrate, followed by transferring of graphene

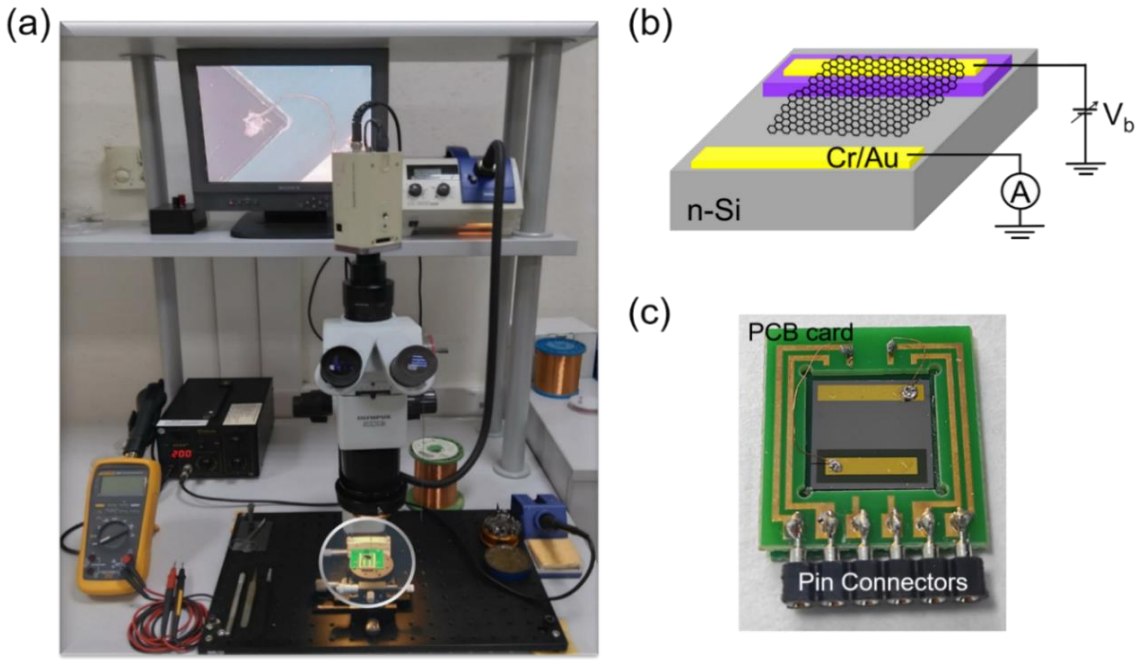

Figure 3.5. (a) Lab-built wire bonder. (b) Schematic illustration of the electrical contacts for two-terminal I-V measurements on the device. (c) The fabricated device's metallic electrodes were connected with Cu plated paths on PCB card and then the pin connectors were soldered with these Cu paths in order to get electrically connection with optoelectronic measurement setup in our laboratory.

3.1.4. Chip Carriers and Wire Bonding

Prior to the opto-electronic measurements, it needs to be carry out electrical contact for two-terminal I-V measurements. As seen from Figure 3.5, the lab-built wire bonder was used to bond electrical connections between the device's metallic contact pads and Cu plated chip carrier paths on the PCB card by using 80 μm copper wire. After two-terminal connection between the device and Cu plated paths was established, the fabricated Gr/n-Si Schottky junction diode is ready to conduct the electrical and optoelectronic measurements.

3.2. Surface Characterization

After transferring of graphene on the n-Si substrate, it should be controlled the presence and quality of graphene film. It is so important for producing high performance device that graphene should be stay continuous without any contamination, holes and cracks during graphene transfer process. Therefore, in our work, optical microscopy and Raman spectroscopy have been carried out to check the presence and quality of graphene.

3.2.1. Optical Microscopy

Optical microscopy is an important tool for characterizing graphene layer by virtue of contrast difference between graphene and substrate. It is a simple, swift and non-destructive technique to obtain surface image of graphene. Even monolayer graphene placed onto n-Si substrate provides a distinguishable contrast with respect to the color of the substrate.

In this work, an optical microscopy (Optika B-500 Optical Microscope) is employed for rapid observation of graphene in order to determine any disruptions in the structure such as defects, residues and holes. Additionally, the homogeneity of graphene transferred onto the Si substrate was determined by looking for whether the color of graphene is the same on all region. Therefore, it is possible to investigate the presence and quality of the transferred graphene on the entire device surface by optical microscopy. All the defects and holes can be effected directly on the performance of the fabricated Gr/n-Si photodiodes, as explained in Chapter 4.

3.2.2. Raman Spectroscopy

Raman spectroscopy is a non-destructive and reliable method, which provides information about molecular vibration in the sample. In this technique, a monochromatic laser beam interacts with chemical bonds of atoms within the material and then the scattered light is detected by a CCD camera. Most of scattered light is at the same energy and does not provide any information, which is named as Rayleigh scattering. However, a small amount of light is scattered at different energies than incident photon, this is called Raman scattering. The shift in energy is based on vibrational, rotational or electronic energy of the molecules that cause the scattering. When plotted the intensity of shifted light versus the wavenumber, it is obtained a Raman spectrum of the material.

Raman spectroscopy is widely used to characterize graphene, giving the information about number of graphene layers, continuity and quality of graphene. The Raman spectrum of graphene includes three main peaks at the specific wavenumbers. The peaks in the Raman spectra of graphene are at 1350 cm^{-1} for D peak, 1582 cm^{-1} for G peak, 2700 cm^{-1} for 2D peak (Jorio 2012; Pimenta et al., 2007), as depicted in Figure 3.6.

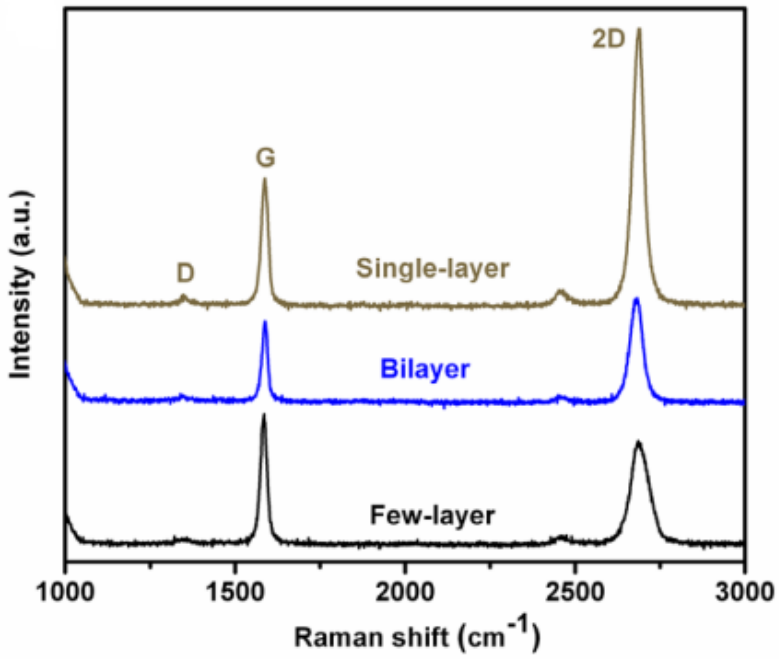

Figure 3.6. Raman spectrum of single-layer, bilayer and few-layer graphene (Source: Di Bartolomeo 2016).

In detail, the D peak is known as defect band or a structural disorder in graphene. It is typically very weak in high quality graphene. G peak indicates in-plane vibrations of sp^2 bonded C-C pairs of graphene. 2D peak is the second order of D band, which gives information about number of graphene layers. The strong G peak and weak D peak indicate good graphitic quality, and the 2D to G peak intensity ratio greater than one ($I_{2D}/I_G > 1$) confirms the monolayer nature of graphene layer. While the $I_{2D}/I_G = 1$ represents the bilayers of graphene, $I_{2D}/I_G < 1$ and close to each other reveals that the grown graphene have three-layers (Y. Y. Wang et al., 2008; Ferrari et al., 2006).

In this work, Raman spectroscopy measurements were performed with a high resolution confocal micro-Raman spectroscopy (MonoVista - Princeton instruments) using Ar^+ ion laser with excitation wavelength of 514 nm (600 groove/mm grating under 100X microscope objective). (see Fig. 3.7)

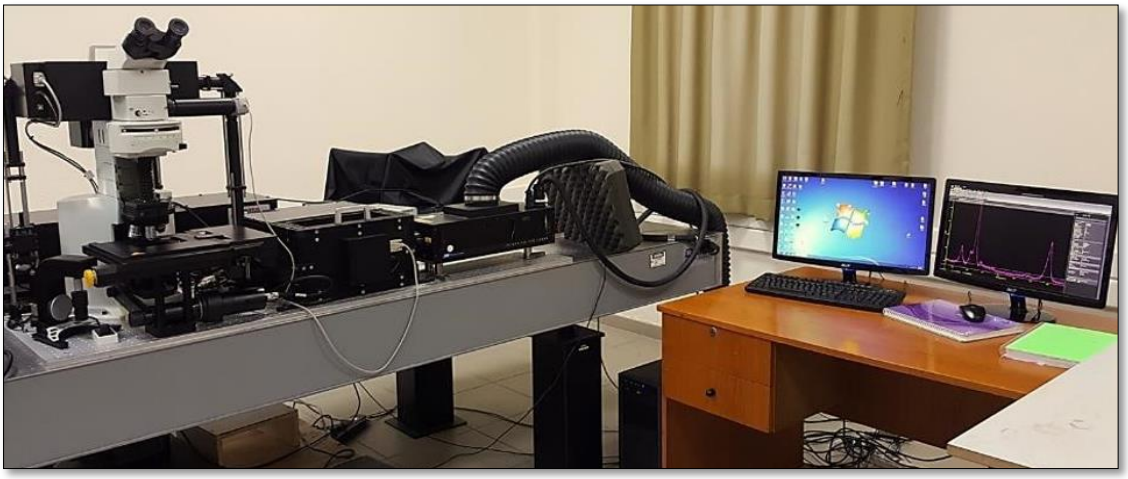

Figure 3.7. Raman spectroscopy measurement setup in department of physics at IZTECH.

3.3. Electrical and Optoelectronic Measurements

3.3.1. Current-Voltage and Spectral Response Measurements

The electronic and optoelectronic characterizations of the fabricated Gr/n-Si photodiodes were done using Keithley 2400 Source-Meter, Keithley 6485 Picoammeter and Keithley 2182 Nanovoltmeter in a rack unit equipped with a quartz tungsten halogen lamp (Osram, 275 W), a high resolution monochromator (Newport, Oriel

Cornerstone), Ocean Optics flame spectrometer and a commercial Si-photodetector (FDS10X10, Thorlabs) as shown in Figure 3.8.

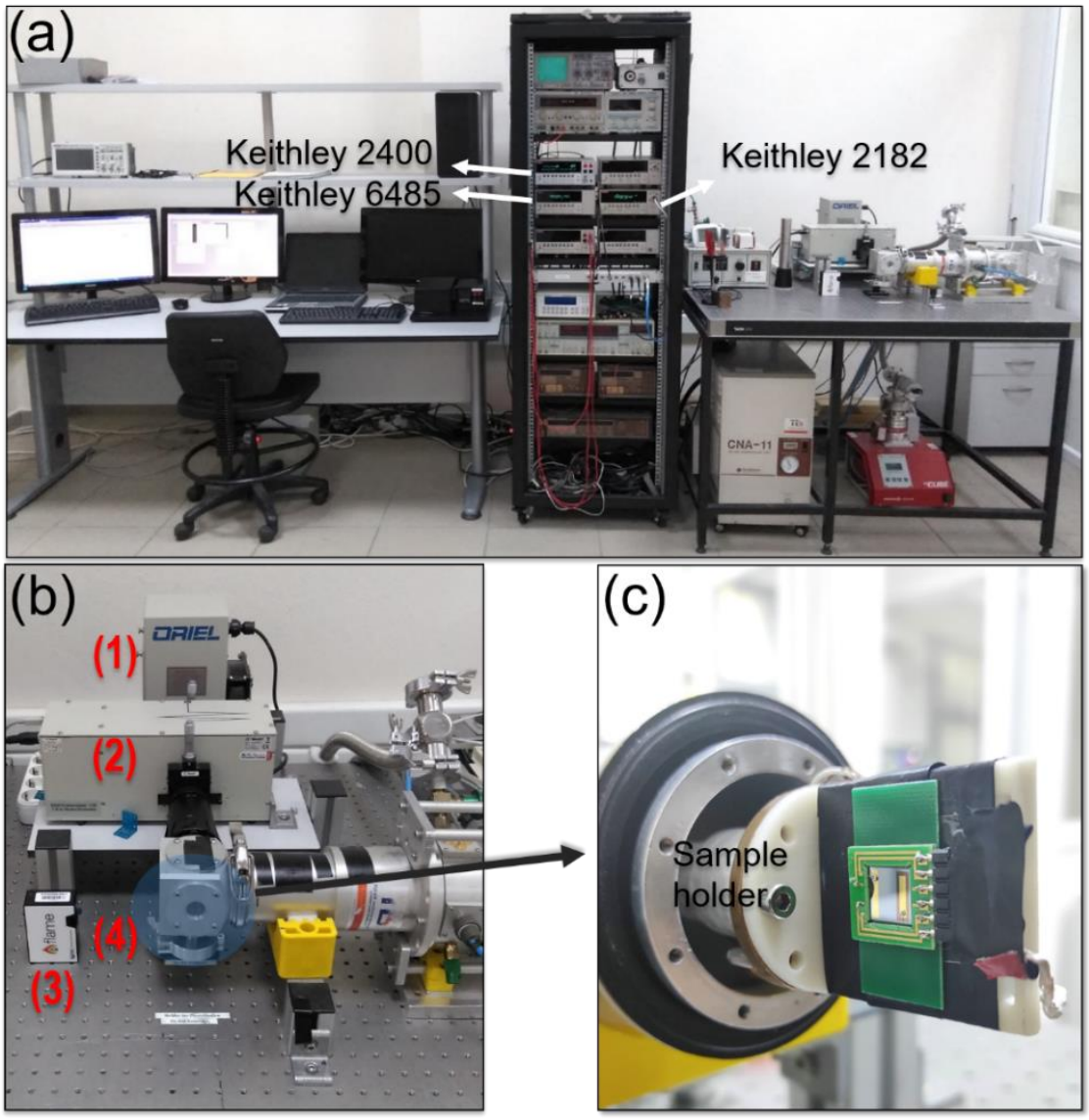

Figure 3.8. (a) Electrical and optoelectronic characterization units in Quantum Device Laboratory at IZTECH. (b) The setup including, (1) a quartz tungsten halogen lamp (Osram, 275 W), (2) a high resolution monochromator (Newport, Oriel Cornerstone), (3) spectrometer (Oceans Optics), (4) a closed loop sample stage. (c) The image shows the Gr/n-Si photodiode after loaded onto sample holder of the system.

I-V plot obtained in the dark can be utilized as a tool to determine important diode parameters such as rectification, ideality factor, Schottky barrier height and series resistance. In this work, I-V characteristics of the devices were carried out at room

temperature under ambient condition. For darkness, the device is connected to a closed loop sample holder as seen in Figure 3.8(c). The voltage was applied for all the devices from 0 to 0.5 V for forward biasing and 0 to – 0.5 V for reverse biasing. In order to conduct power-dependent I-V measurements under light illumination at the wavelength of 905 nm, a tungsten-halogen lamp with a value of 275 W was used to generate light and a specific wavelength of 905 nm was separated by using a monochromator including an appropriate grating, which operates between 515 nm to 1200 nm. All measurements under 905 nm light illumination were taken with a filter, which passes 515 nm and above, also in order to suppress unwanted intense second order harmonics.

Spectral response (R) is a meaning of its optical responsivity as a function of wavelength. Prior to the responsivity measurements, spectrometer was used to calibrate full width half maximum (FWHM) of light by tuning the slit mounted on the monochromator and then a commercial Si-photodetector as reference detector was used to determine the incoming power of light on the device area, giving power output in unit of watt. Hence, responsivity vs. wavelength data on our fabricated devices were obtained based on this power output. The irradiation wavelength is specifically selected to be 905 nm since it corresponds to the maximum spectral response of our fabricated Gr/n-Si photodiode.

3.3.2. Time-Resolved Photocurrent Measurements

Time-resolved photocurrent measurements were performed using a led driver with pulse modulation (DC2200, Thorlabs), collimated led source with 940 nm (M940L3-C4, Thorlabs), 905 nm laser line filter (FL905-10, Thorlabs), transimpedance amplifier (AMP102, Thorlabs) and oscilloscope (MS05204, Rigol) as shown in Figure 3.9. In this setup, a led which has 940 nm wavelength was used as a light source. The light pulses incoming on the sample were controlled by a LED controller. A specific wavelength of 905 nm was provided with a laser filter. After the photocurrent obtained as a result of incoming pulsed light on the sample, transimpedance amplifier convert the photocurrent to voltage and amplify the signal, so we get the data from oscilloscope.

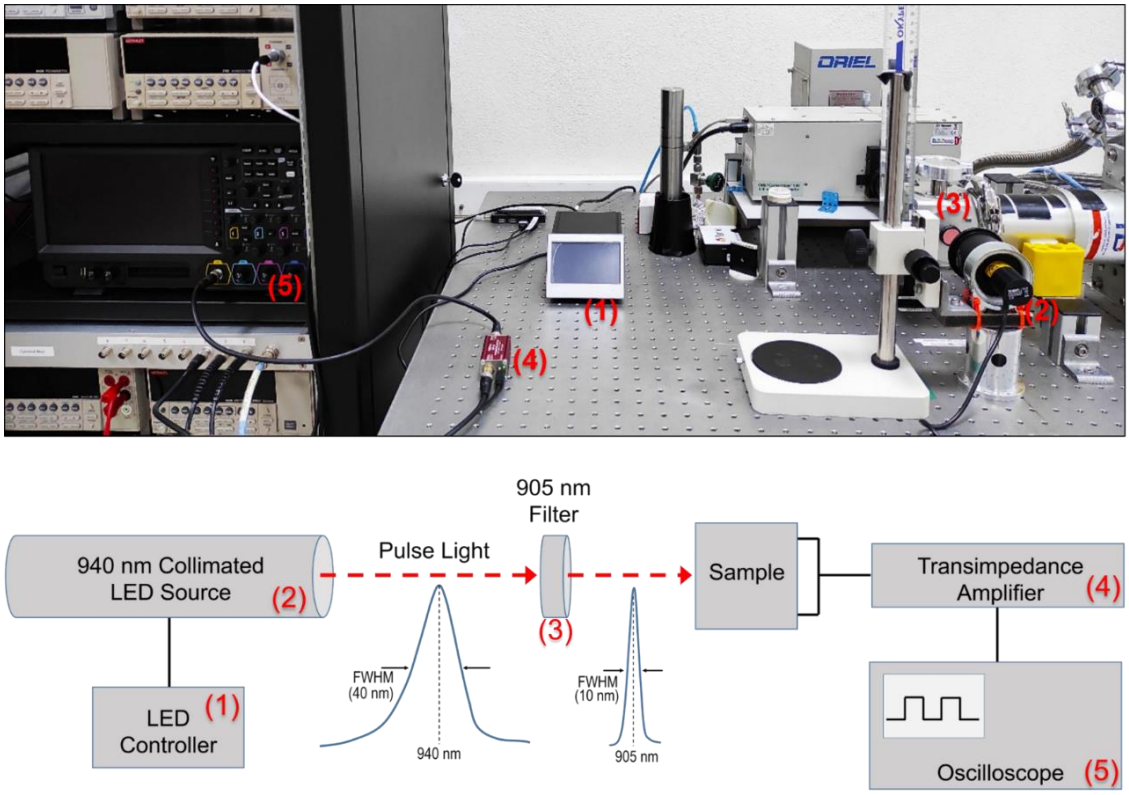

Figure 3.9. The image and schematic illustration of the time-resolved photocurrent measurement setup in Quantum Device Laboratory at IZTECH.

3.3.3. Four-Probe and Hall Effect Measurements

In order to determine some fundamental electronic transport characteristics such as mobility (μ), sheet resistance (R_s) and charge carrier density (n), it is necessary to perform four-point probe and Hall effect measurements. For the measurements, 4-terminal (4W) contacts onto the sample must be deposited in the geometry of van der Pauw, comprising 1 mm × 1 mm ohmic contacts placed at the corners of sample (Figure 3.10(c)).

Sheet resistance and Hall effect measurements were done with a lab-built four-point probe station having properly oriented Au plated pins connected to Keithley 6220 Precision Current Source and Keithley 2000 Digital Multimeter as shown in Figure 3.10(a-b). The interface of the main program consists of three programs. First measurement is IV characterization, which is necessary to check to ohmic quality of metallic contacts deposited on the sample. In order to measure sheet resistance in correctly, the contacts must be ohmic. Then, we start the sheet resistance program. After

measured the resistance value in the eight different positions, the program gives the calculated sheet resistance of the sample. Afterwards, Hall effect measurements were done under a permanent magnet out of neodymium providing an effective magnetic field of 0.33 T. After the measurements, doping type (p or n), carrier mobility and doping concentration are obtained.

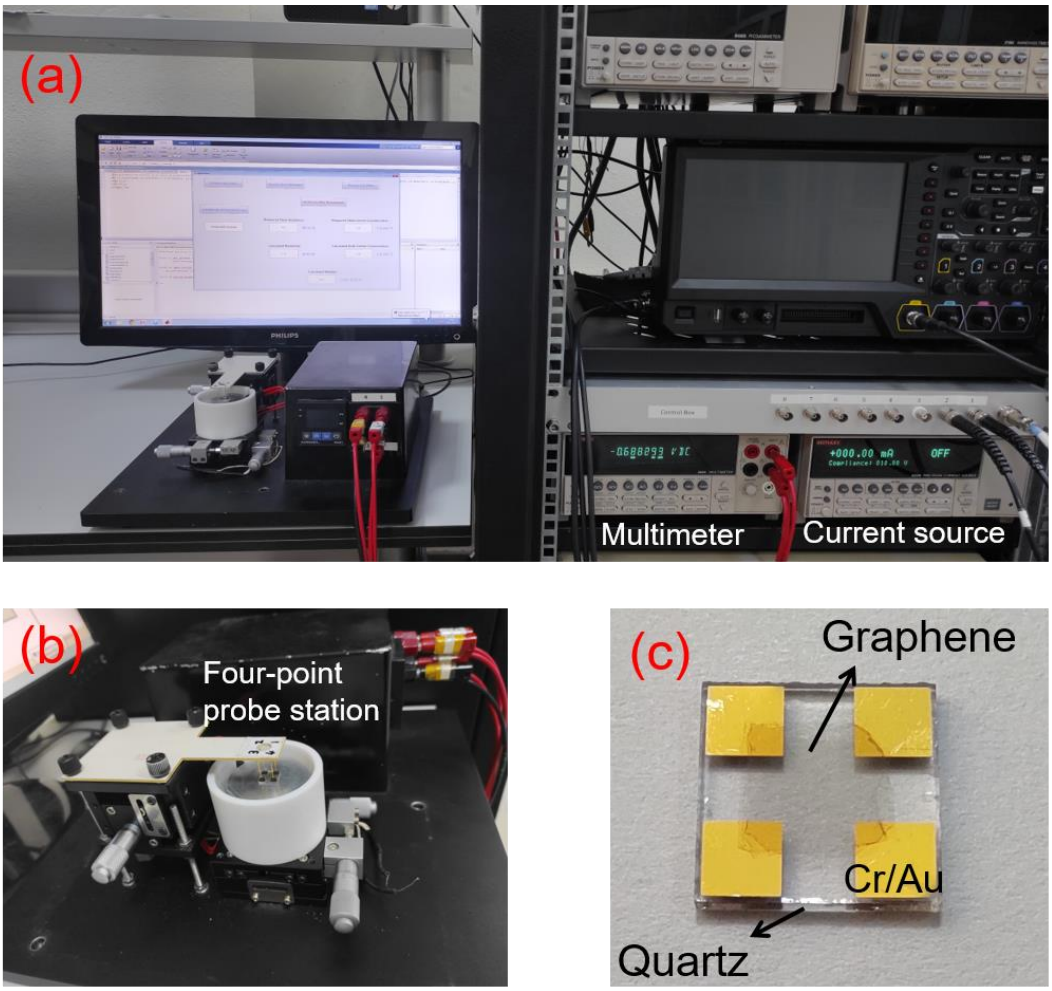

Figure 3.10. (a) The four probe and Hall effect measurement setup. (b) The four probes which are connected independently of each other and touched the Cr/Au contacts of the sample. (c) Configuration of Van der Pauw geometry for electronic transport measurement (graphene touches the metallic contacts).

3.3.4. Optical Transmittance Measurements

In order to measure optical transmittance values depending on graphene layers, we built an experimental setup demonstrated in Figure 3.11. Here, the transmittance measurements of the sample shown in Figure 3.10(c) were done by using a halogen lamp, monochromator, fiber-optic cable and a spectrometer. The broadband light emitted from the halogen lamp source is set a fixed wavelength of 905 nm via monochromator. Then, the specific wavelength with 905 nm is guided to sample and the transmitted light is collected by the spectrometer.

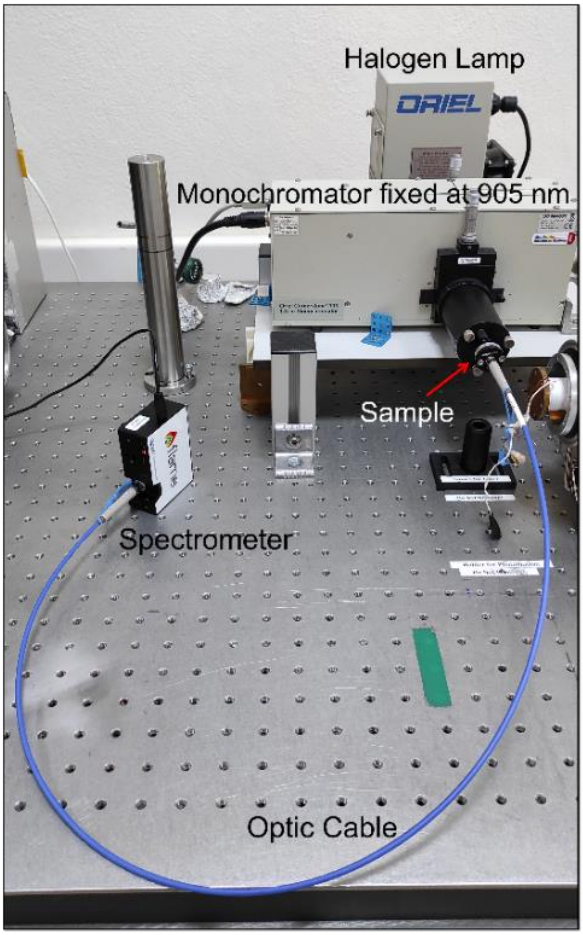

Figure 3.11. Configuration of transmittance measurement setup in Quantum Device Laboratory at IZTECH

CHAPTER 4

RESULTS AND DISCUSSION

4.1. Light-induced Modification of the Schottky Barrier Height in Graphene/Si Based Near-infrared Photodiodes

In this section, I have investigated the impact of light on the Schottky barrier height (Φ_B) of graphene/n-type silicon (Gr/n-Si) based Schottky junction photodiodes. For the device structure used in this study, about 400 nm thick SiO_2 dielectric layer is evaporated partially on the surface of (10 mm × 10 mm) n-Si substrate with 1-5 Ω.cm resistivity. For conducting two-terminal I-V measurements, Cr/Au (5 nm/80 nm) metal contact pads were deposited both on the n-Si side and on the SiO_2 covered side of the substrate by a thermal evaporator. Then, monolayer graphene grown by CVD technique was transferred on the device structure shown in Figures 4.2(a) and (b). The active area of the junction, where the graphene layer is in intimate contact with the n-Si side of the substrate, was measured as ~10 mm^2. As for the experimental investigation of the sample, the dark and light I-V measurements were performed at room temperature and under ambient conditions. Afterwards, Hall effect measurements were done in order to reveal charge carrier dynamics of the device. Additionally, the photoresponsivity of our device was measured at zero-bias and under reverse bias voltages.

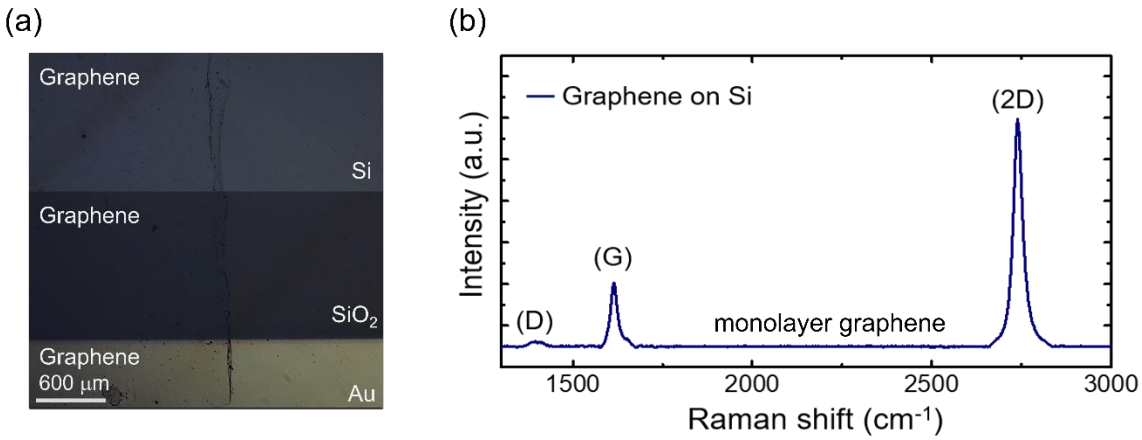

Figure 4.1. (a) Optical micrograph of selected region on fabricated Gr/n-Si photodiode. (b) A typical single-point Raman spectrum taken from graphene electrode on n-Si substrate.

Prior to electrical/optoelectronic measurements, I take an image with optical microscope for rapid observing to graphene layer by looking color contrast. The color contrast (dark zone) seen in Figure 4.1(a) refers to the presence of graphene layer. In addition, the thickness of transferred graphene was determined by single-point Raman spectroscopy measurement taken from the randomly chosen spot of the sample surface. Figure 4.1(b) shows a Raman spectrum of the graphene on Si part of device structure. From the obtained Raman spectra, the large 2D to G peak intensity ratio ($I_{2D}/I_G > 1$) verifies the single-layer thickness of the graphene layer (Ferrari et al., 2006). The observed weak D peak confirms the high quality of the graphene.

The I-V measurement of the fabricated Gr/n-Si sample in dark is shown in Figure 4.2(c) as a function of bias voltage applied in the range between – 0.5 V and 0.5 V. The dark I-V curve exhibits the strong rectifying character of a typical Schottky diode and can be explained in terms of the well-known thermionic emission model (Sze and Ng 2007) given as,

$$I = I_0 \left[exp\left(\frac{qV}{\eta kT}\right) - 1 \right] \quad 4.1$$

where (I_0) is the reverse saturation current which is written as,

$$I_0 = AA^* T^2 \exp\left(-\frac{q\Phi_B}{kT}\right) \quad 4.2$$

A is the active junction area (0.1 cm^2 for our Gr/n-Si sample), A^* is the effective Richardson constant (112 A/cm^2K^2 for n-Si), T is the temperature (300 K), Φ_B is the Schottky barrier height at the junction between Gr and n-Si, k is the Boltzmann constant, q is the elementary charge and η is the ideality factor. The Schottky diode parameters η and Φ_B for the fabricated Gr/n-Si diode were extracted using the method developed by Cheung (Cheung and Cheung 1986) in the case of non-negligible series resistance (R_s). The Cheung's function is given as,

$$\frac{dV}{dln(I)} = IR_s + \eta\frac{kT}{q} \quad 4.3$$

Equation (4.3) was used to determine the R_s and η from the slope and the intercept of the straight line fitting *dV/dln(I)* vs. *I* plot, respectively. The R_s and η values of the sample were found to be 4 kΩ and 2.61, respectively. The *H(I)* function given in Eq. (4.4), the Φ_B of the junction is determined.

$$H(I) = V - \eta\left(\frac{kT}{q}\right) ln\left(\frac{I}{AA^*T^2}\right) = IR_s + \eta\Phi_B \qquad 4.4$$

From the intercept of the linear region of *H(I)* vs *I* plot as shown in Figure 4.2(d), the zero-bias Φ_B of our Gr/n-Si diode in dark was determined as 0.72 eV. These obtained diode parameters are consistent with the previously reported η and Φ_B values for the heterojunction of monolayer graphene with n-Si (Miao et al., 2012; Singh et al., 2014; Parui et al., 2014).

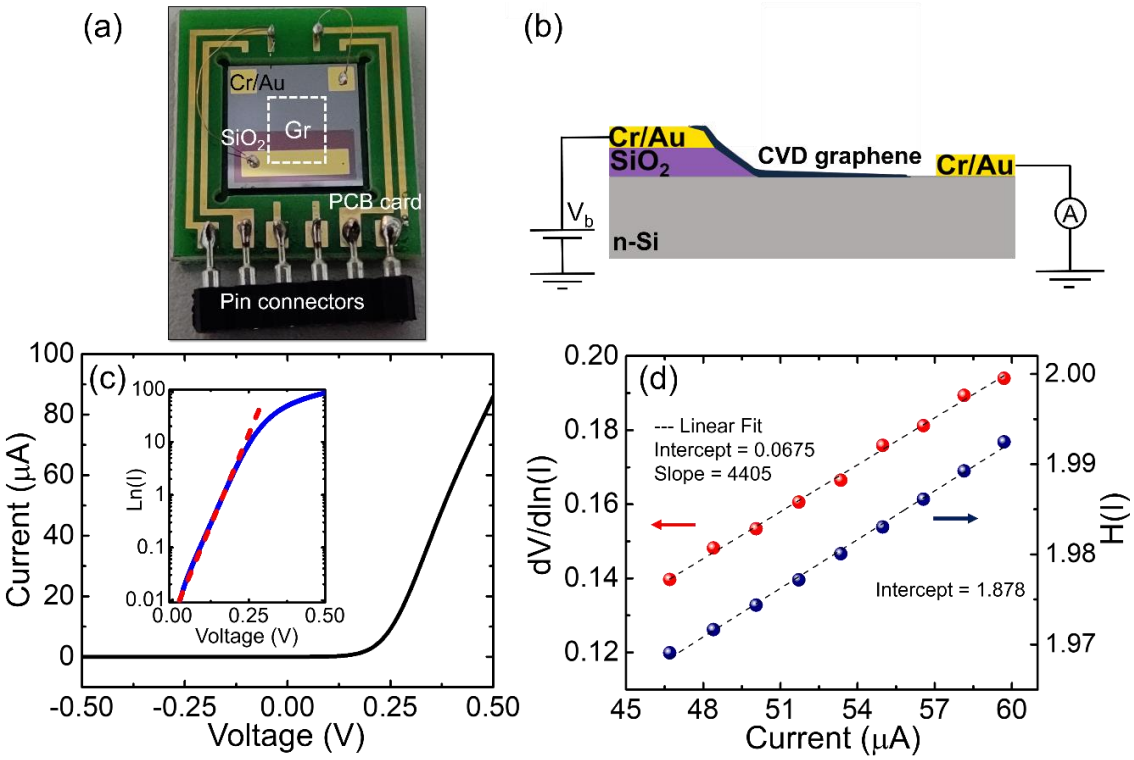

Figure 4.2. (a) Schematic illustration and (b) the cross-sectional image of the fabricated Gr/n-Si Schottky junction photodiode after electrical connections. (c) The I-V curve of the device in dark. Inset shows the forward bias ln(I)-V plot. (d) Plots of *dV/dlnI* and *H(I)* as a function of current which were used to extract diode parameters according to Cheung's method.

The variation in the I-V characteristics of our sample exposed to 905 nm wavelength light with different power densities were displayed in the semi-logarithmic scale in Figure 4.3(a). The sample exhibits a clear photovoltaic activity under light illumination. For each of the I-V curves, the voltage read at the minimum current and the current at zero bias correspond to open-circuit voltage (V_{oc}) and short-circuit current (I_{sc}), respectively. Although I_{sc} exhibits a clear linear response to the incident light, V_{oc} increases nonlinearly and converges to a saturation level of around 0.18 V at the light power density of 200 μW/cm^2 as seen in Figure 4.3(b).

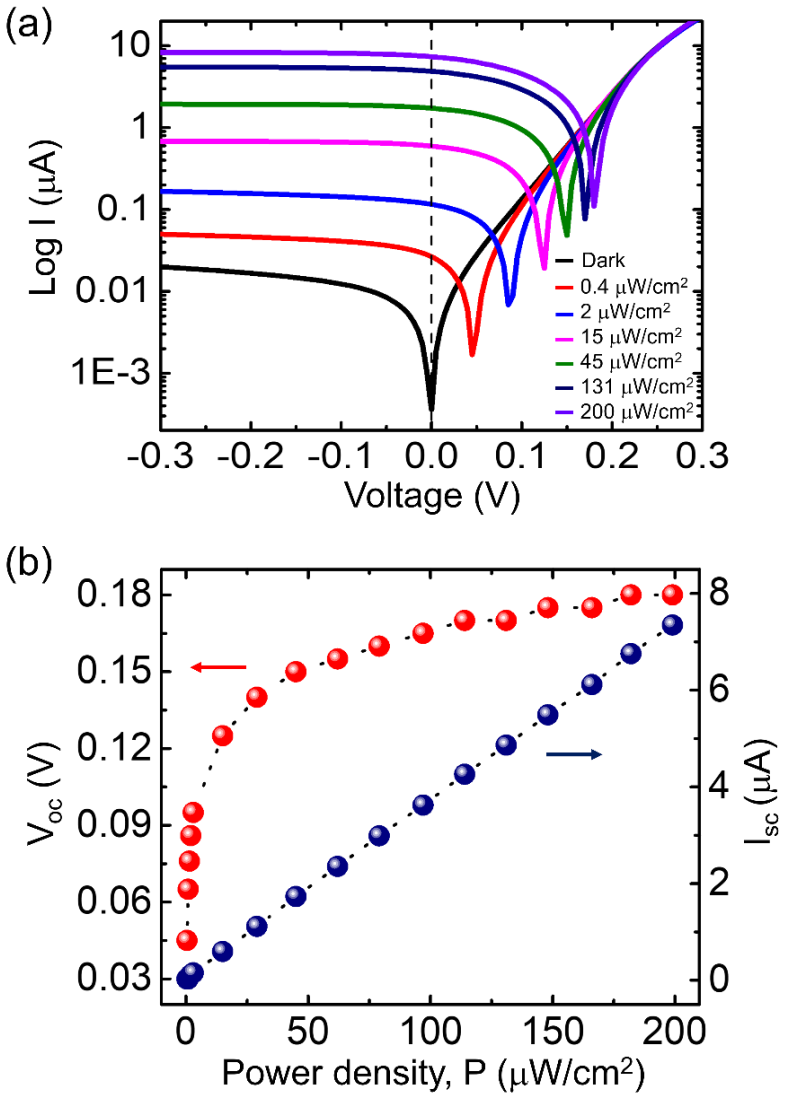

Figure 4.3. (a) Semi-logarithmic scale I-V characteristics and (b) I_{sc} and V_{oc} of the fabricated Gr/n-Si photodiode exposed to 905 nm wavelength light with different power densities, respectively.

The observed nonlinear variation of V_{oc} with the light power density has been previously attributed to the quasi-Fermi level transport model which was also used to interpret the light intensity dependence of V_{oc} for polymer:fullerene bulk heterojunction solar cells (Wan et al., 2017; Koster et al., 2005). From the slope of I_{sc}-P plot the spectral responsivity of the photodiode was determined as 0.4 AW^{-1} which is comparable to that of single-layer Gr/n-Si based photodiodes reported previously (Lv et al., 2013; Wan et al., 2017).

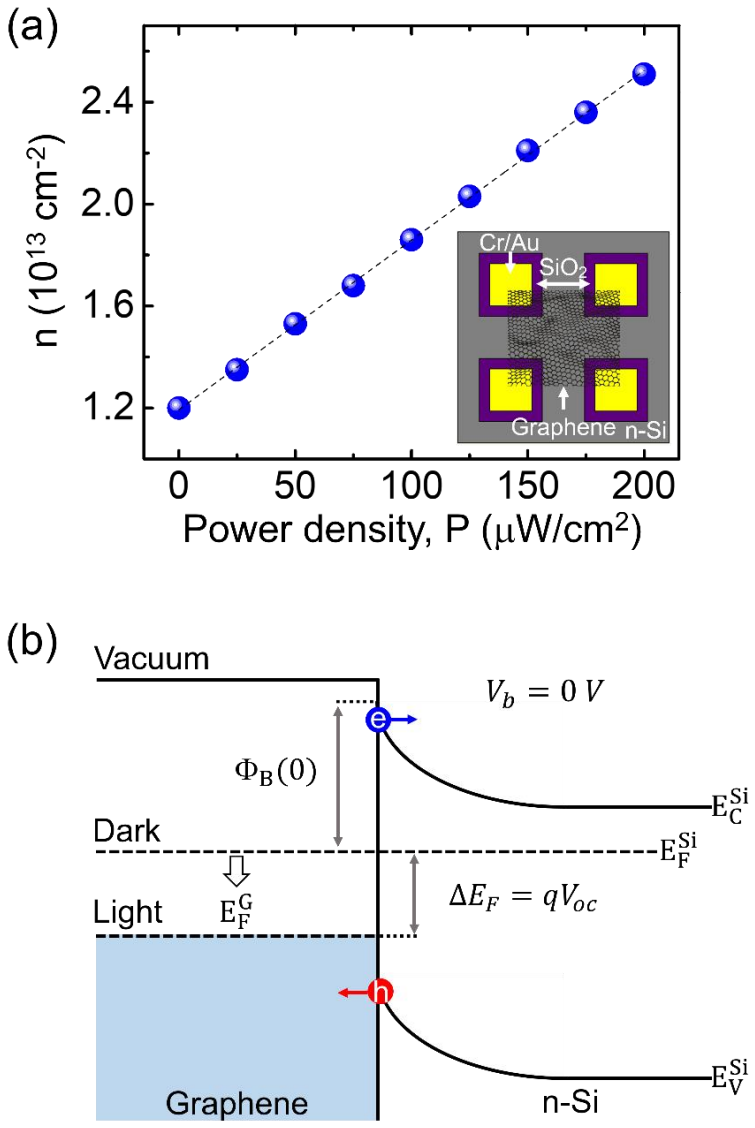

Figure 4.4. (a) The variation of hole carrier concentration in monolayer graphene as a function of incident light power density. Inset depicts the illustration of Gr/n-Si sample in Van der Pauw geometry that was used to conduct four-point probe and Hall effect measurements. (b) The schematic illustration of the energy band diagram for Gr/n-Si Schottky junction photodiode in dark and under light illumination.

In order to reveal the charge carrier dynamics of our sample, we carried out Hall effect measurements on a single layer graphene transferred on the surface of a (10 mm × 10 mm) n-Si substrate having Cr/Au electrodes on 400 nm thick SiO_2 insulation pads at its corners (see inset of Fig. 4.4(a)). The measurements were done under different incident light power densities ranging between 0 - 200 μW/cm^2. In the absence of light illumination, graphene layer was determined to be unintentionally p-type doped with an intrinsic hole carrier concentration of about 1.2 × 10^{13} cm^{-2}. However, under light illumination, the hole carrier concentration in graphene layer increases linearly up to 2.5 × 10^{13} cm^{-2} as the light power density is rised from 0 to 200 μW/cm^2 as seen in Figure 4.4(a). This suggests that the amount of photo-generated charge carriers is greatly proportional with the absorbed photon flux as also evidenced by the linear dependence of I_{sc} on the light power density in Figure 4.3(b).

Based on the discussions above, an increase in the hole concentration due to incident light is expected to significantly shift the E_F of graphene (Figure 4.4(b)) towards higher energy levels away from its Dirac point. As a consequence of the shift in graphene's E_F, an energy difference of $\Delta E_F = E_F^{Si} - E_F^G$ is formed which is directly proportional with the V_{oc} measured under light illumination. For a quantitative analysis, the carrier concentration dependent variation in graphene's E_F is calculated with the relation (Fang et al., 2007; Tongay et al., 2012),

$$E_F = \hbar v_F \sqrt{\pi n} \tag{4.5}$$

where v_F (1 x 10^8 cm/s) and n are the Fermi velocity and the measured hole carrier concentration, respectively. Since the hole concentration in graphene on n-Si is dominated by the light power density (P), the shift in graphene's E_F can be determined by rearranging equation (4.5) as,

$$\Delta E_F(P) = \hbar v_F \pi^{1/2} \left(\sqrt{n(P)} - \sqrt{n(0)} \right) \tag{4.6}$$

where $n(0)$ and $n(P)$ are the hole carrier concentration of graphene on n-Si before and after the light illumination, respectively. In the case of P = 200 μW/cm^2, which is the highest light power density that we could achieve with our experimental set-up, ΔE_F was found to be about 0.18 eV which is in the same range as the experimentally

obtained V_{oc} (0.18 V). As a consequence of the shift in graphene's Fermi level relative to that of n-Si, the Φ_B of Gr/n-Si heterojunction increases in accordance with the relation $\Phi_B(P) = \Phi_B(0) + q|V_{oc}(P)|$. Here, $\Phi_B(0)$ and $\Phi_B(P)$ are the Schottky barrier height of the heterojunction before and after light illumination, respectively. Considering $\Phi_B(0) = 0.72$ eV and the V_{oc} data shown in Figure 4.3(b), we plotted the Φ_B of our Gr/n-Si photodiode as a function of light power density in Figure 4.5(a). Following a steep rise at low light power densities (e.g., P < 10 μW/cm^2), Φ_B increases gradually and approaches to a saturation value of around 0.90 eV when the light power density reaches at 200 μW/cm^2. The nonlinear behavior of Φ_B which is governed by V_{oc} is interpreted in terms of the charge recombination processes discussed below.

A common approach to explore the rate and mechanisms of recombination processes for the photodiodes operating in photovoltaic mode is to determine the carrier lifetime and/or the recombination current (e.g., I_{sc} in our case) as a function of V_{oc}. Since no current is flowing at open-circuit, all possible effects arising from the series resistance of the device are minimized. Therefore, V_{oc} can be used directly as a measure of how strongly the carrier distribution of the illuminated sample differs from thermal equilibrium. The correlation between V_{oc} and I_{sc} for such devices is defined in terms of the Shockley equation (Shockley 1949) written as,

$$I_{sc} = I_0 \exp\left(\frac{qV_{oc}}{\eta kT}\right) \tag{4.7}$$

where I_0 is the dark saturation current and I_{sc} is the short-circuit current. For our Gr/n-Si photodiode sample, the dependence of η on the light power density (P) can be calculated by rearranging Eq. 4.7 as in the following form,

$$\eta(P) = \frac{qV_{oc}(P)}{kT} \times [ln\,(I_{sc}(P)/I_0)]^{-1} \tag{4.8}$$

The variation of η with the light power density is plotted in Figure 4.5(a) for I_0 = 26 nA and $\eta(0)$ = 2.61 of our sample. It is known from the literature that η = 1 corresponds to radiative band-to-band free carrier recombination and/or to the non-radiative Shockley-Read-Hall (SRH) recombination via shallow states. However, for indirect gap semiconductors like Si, band-to-band free carrier recombination should not be expected. On the other hand, $\eta \geq 2$ is realized also for SRH recombination but throughout mid-gap

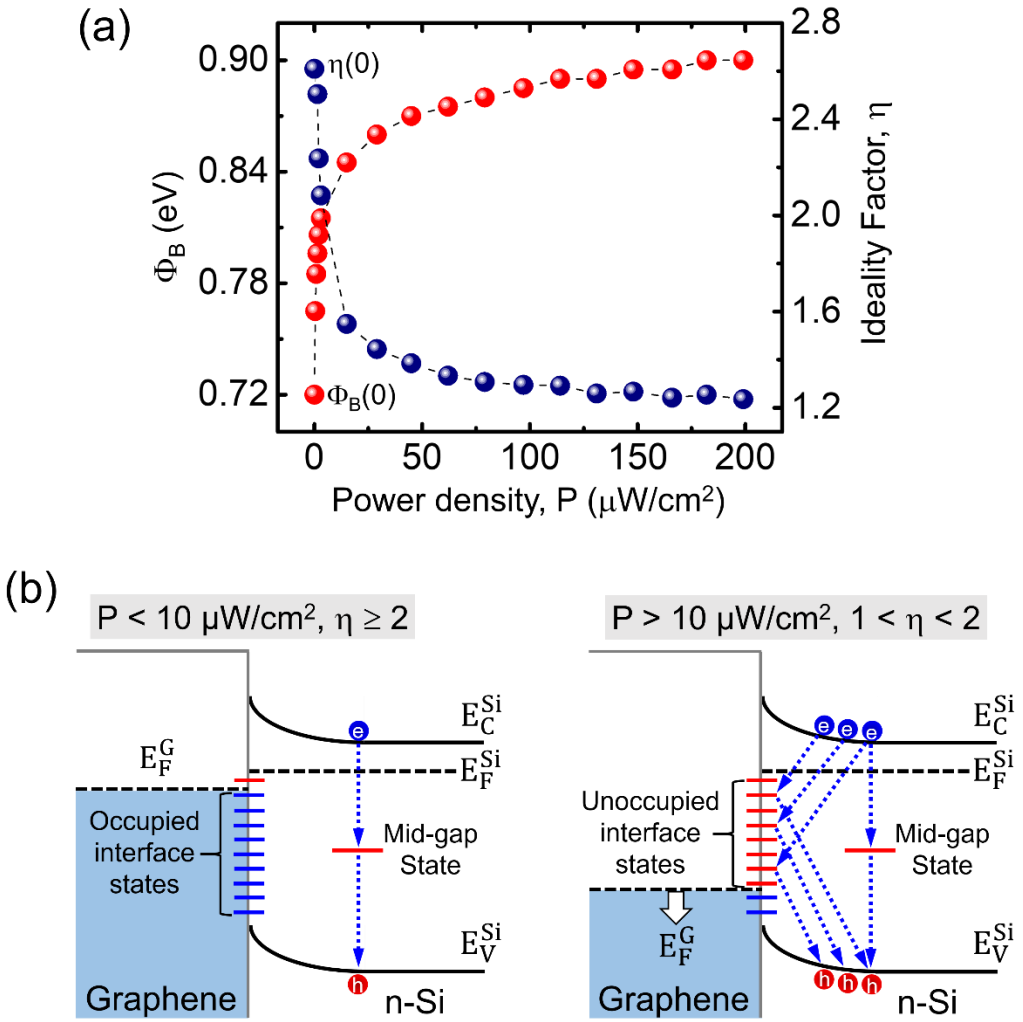

Figure 4.5. (a) Φ_B and η versus light power density plots for Gr/n-Si Schottky diode. (b) The schematic energy band diagram of Gr/n-Si Schottky junction photodiode depicting the charge recombination mechanisms at low and high incident light power densities.

states (or deep trap states) located at the depletion region of heterojunction devices (Arefinia and Asgari 2014; 2015). As seen in Figure 4.5(b), the charge recombination in our sample is greatly dominated by the mid-gap states at low light power densities (P < 10 μW/cm^2). However, as the light power density is increased gradually above 10 μW/cm^2 the calculated η varies between the values 1 and 2. In this case some exotic effects like surface recombination processes occur in heterojunction devices as reported in (Stolterfoht et al., 2019; Wolff et al., 2019). For the light power densities below 10 μW/cm^2, where the Fermi level of graphene electrode is slightly shifted relative to that of n-Si substrate, most of the interface states are occupied with electrons due to charge transfer from graphene layer. Since the number of unoccupied interface states required

for surface recombination is not sufficient enough, the recombination occurs mostly via mid-gap states. However, as the light power density is increased, a great number of unoccupied interface states to contribute recombination become available as a consequence of the significant shift in graphene's Fermi level. And therefore the recombination throughout the interface states becomes dominant for $P > 10$ μW/cm^2. The interplay between these two distinct recombination processes seems to be the main reason for the nonlinear variation of both V_{oc} and Φ_B of our sample.

The spectral response (R) is one of the most important device parameters of a photodiode and is defined as the ratio of generated photocurrent (I_p) to the incident light power (P) at a certain wavelength. Figure 4.6 shows the R measurements of our sample over a broad spectrum from 540 nm to 1050 nm at zero bias and under reverse bias voltages of – 2 V and – 4 V. The maximum R appeared at a peak wavelength of 905 nm and exhibited a downward trend towards a cutoff wavelength of 1050 nm, which is due to doping concentration and the band gap of n-Si substrate, respectively. At the peak wavelength of 905 nm, the device at zero bias revealed a responsivity value of 0.40 AW^{-1}, while the responsivity of the device was measured to be 0.56 AW^{-1} under reverse bias of – 4 V. This is due to the increase of the external electric field with applied bias. It is well known that when the Gr/n-Si Schottky junction photodiode is illuminated, the incident photons generate electron-hole pairs in the n-Si substrate.

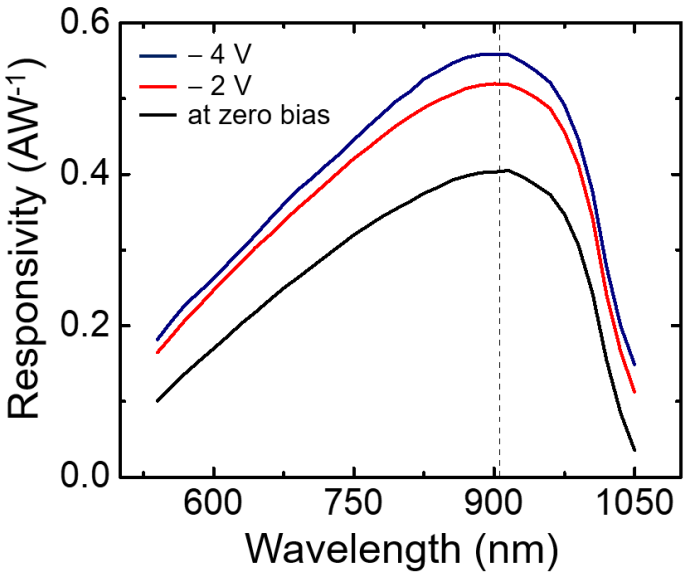

Figure 4.6. Spectral responsivity of the Gr/n-Si device for wavelength ranging from 540 nm to 1050 nm at different applied bias voltages of 0, – 2 V and – 4 V.

Besides that, the applying reverse bias voltage on such devices causes a dilation in the depletion region of Gr/n-Si heterojunction and the photogenerated holes in n-Si accelerate into graphene, leading to more excessive photocurrent. On the other hand, the dark current values of the sample were found to be increased from 0.6 nA to 48 nA when the applied bias voltage reaches to − 4 V. So, this leads to reduce signal-to-noise ratio of the diode.

The effect of doping concentration of n-Si substrate on Gr/n-Si photodiodes was investigated. At the previous works in our laboratory, Aydin et al., and Gülçin et al., studied on Gr/n-Si photodiode produced with CVD graphene transferred on n-Si substrate with a resistivity of 1-10 ohm.cm (doping concentration ~ 4-5 × 10^{14}). The experimental results showed that the obtained maximum responsivity of the devices were at the wavelength range of 780 - 850 nm. On the other hand, in my work, I have studied with phosphorus doped silicon wafer with a resistivity of 1-5 ohm.cm (doping concentration ~ 1-5 × 10^{15}). The photoresponsivity measurements demonstrated that the maximum responsivity was at the wavelength of 905 nm. The peak of responsivity for Gr/n-Si samples fabricated with the low resistivity substrate occurs at the higher wavelength as shown in Figure 4.7. The n-Si substrate with low resistivity has high carrier concentration; this leads to narrowing the band gap of n-Si. The Gr/n-Si diodes operated at 905 nm wavelength have the potential to be used in optoelectronic device technologies such as laser range finder, high-speed photometry and LIDAR.

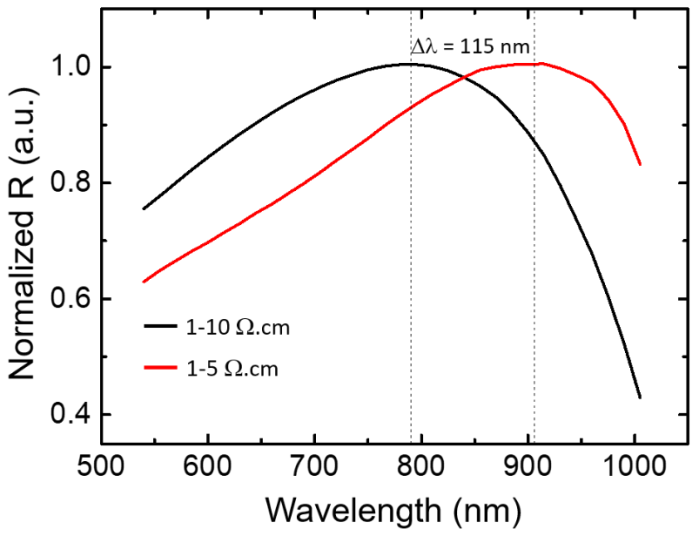

Figure 4.7. Comparison of spectral responsivity of the fabricated Gr/n-Si devices with different substrate resistivity.

4.2. Junction Area Dependent Performance of Graphene/Silicon Based Self-Powered Schottky Photodiodes

The impact of junction area on the device performance parameters of Gr/n-Si based Schottky photodiodes is also investigated. Herein, three batches of Gr/n-Si photodiode samples were produced based on various sized CVD grown monolayer graphene layers transferred on individual n-Si substrates. A schematic of the fabricated Gr/n-Si Schottky photodiodes is shown in Figure 4.8.

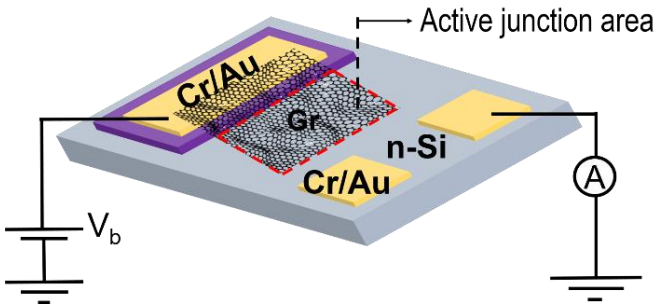

Figure 4.8. Schematic illustration of the fabricated Gr/n-Si photodiode.

Firstly, I investigated the dark I-V characteristic of the photodiodes with three different junction areas such as 4 mm^2, 12 mm^2 and 20 mm^2. From the obtained I-V measurements the dark current (I_d) of all the devices were extracted as ~ 0.3 nA. As seen in Figs. 4.9(a-c), the I-V measurements of the samples displayed typical rectifying Schottky junction behaviour. From the I-V data the reverse saturation current (I_0) values were determined to be 0.75 × 10^{-8}, 2.61 × 10^{-8} and 0.78 × 10^{-8} for the photodiodes with junction area of 4 mm^2, 12 mm^2 and 20 mm^2, respectively. From the linear forward-bias region of the ln(I)–V plot shown at the right of Figs. 4.9(a-c), the Schottky diode parameters η and Φ_B for our devices were extracted by using the method developed by Cheung et al., (Cheung and Cheung 1986) as explained in previous section of 4.1. For the junction areas of 4 mm^2, 12 mm^2 and 20 mm^2, the η of our devices were found to be 1.20, 1.89 and 1.06, respectively. By means of the corresponding η values, zero-bias Φ_B of the devices in dark were deduced as 0.87 eV, 0.76 eV and 0.96 eV, respectively. It should be mentioned that these diode parameters are consistent with the previously reported η and Φ_B parameters for the heterojunction

of monolayer CVD graphene with n-Si substrate (H. Y. Kim et al., 2013; Tongay et al., 2012; Y. Wang, Yang, Lambada, et al., 2020). The variation in η and Φ_B may originate from the degree of unintentional hole doping of graphene electrode due to the chemicals used in the growth and transfer processes and/or from the inhomogeneities at the Gr/n-Si interface. For example, impurities and defects modify graphene's work function by shifting its Fermi level relative to its charge neutrality point and therefore changes the magnitude of η and Φ_B in Gr/n-Si heterojunction.

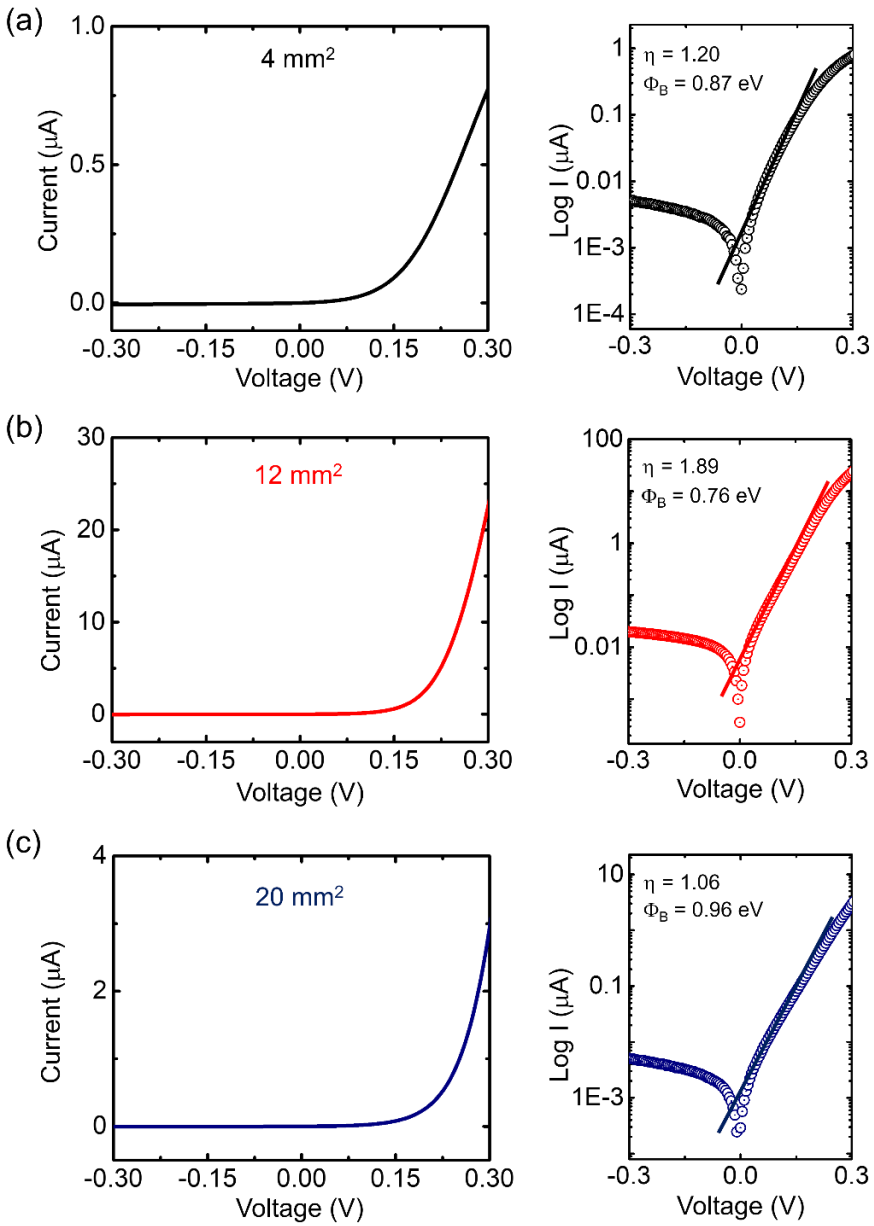

Figure 4.9. The dark I-V graphs of the Gr/n-Si photodiodes depending on junction areas: a) 4 mm^2, b) 12 mm^2 and c) 20 mm^2. Plots on the right show the dark I-V measurements of the devices on a semi-logarithmic scale, which was used to extract the ideality factor and the barrier height of the diodes.

Figure 4.10(a) displays the R spectrum of the samples with different junction areas at zero bias voltage. All the measurements were done at the wavelength ranging from 540 nm to 1050 nm under the same conditions. The measurements showed that the R parameter of the Gr/n-Si Schottky photodiode has an excellent linear dependence on the junction area as displayed in Figure 4.10(b). In our device design the junction area is defined as the photoactive region where the graphene electrode is in direct contact with the underlying Si substrate. Therefore, the dimension of the junction area is determined only by the size of the graphene electrode itself. The large lateral dimensions of the graphene electrode (or the size of junction area) lead to greater depletion region length of the junction. This promotes the vertical electric field across the Gr/n-Si heterojunction and enhances the effective separation/collection of photo-generated charge carriers at the depletion region. Because of enhanced charge separation and collection, the photocurrent and thus the spectral response of our photodiode increase as a function of the size of graphene electrode. The maximum R of 0.76 AW^{-1} was achieved for the device with a junction area of 20 mm^2. This is the highest R value measured for a self-powered Gr/n-Si Schottky photodiode presented in the literature.

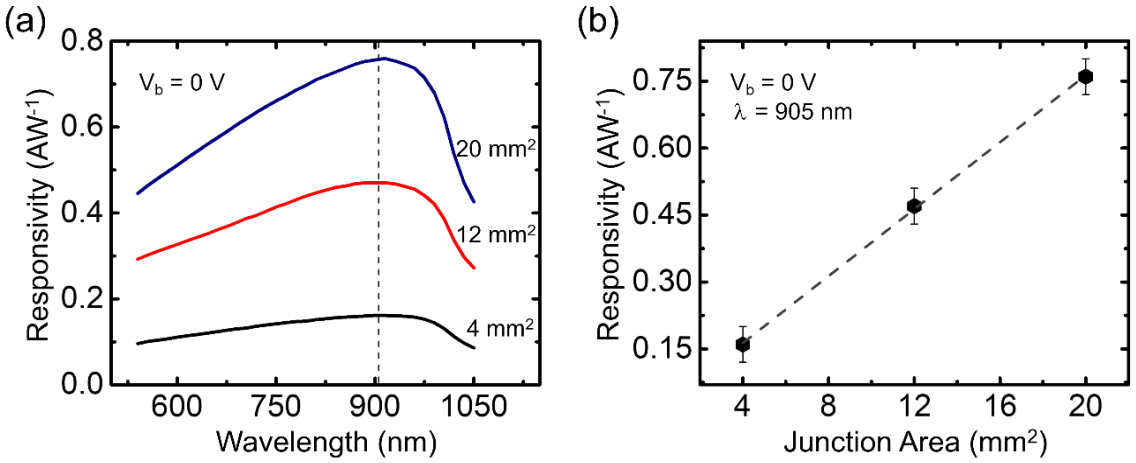

Figure 4.10. (a) Responsivity vs. wavelength of the Gr/n-Si devices based on different junction areas at zero-bias voltage. (b) Responsivity of the devices at the peak wavelength of 905 nm at $V_b = 0$ V.

Based on the measured R values, we also calculated the specific detectivity (D^*) and noise equivalent power (NEP) parameters of our samples. Here, D^* is defined as the weakest level of light detected by a photodiode having a junction area of 1 cm^2 and is determined by (Wan et al., 2017),

$$D^* = \frac{A^{1/2}R}{\sqrt{2qI_d}} \qquad 4.9$$

where A is the junction area (0.04 cm^2, 0.12 cm^2 and 0.2 cm^2 for our Gr/n-Si samples, respectively), q is the elementary charge. NEP is the incident power required to obtain a signal-to-noise ratio of 1 at a bandwidth of 1 Hz and is calculated by (Xinming Li et al., 2016),

$$NEP = \frac{A^{1/2}}{D^*} \qquad 4.10$$

D^* and NEP of our samples were calculated using Eq. 4.9 and Eq. 4.10, respectively and the obtained results were displayed as a function of wavelength in Figure 4.11(a-c).

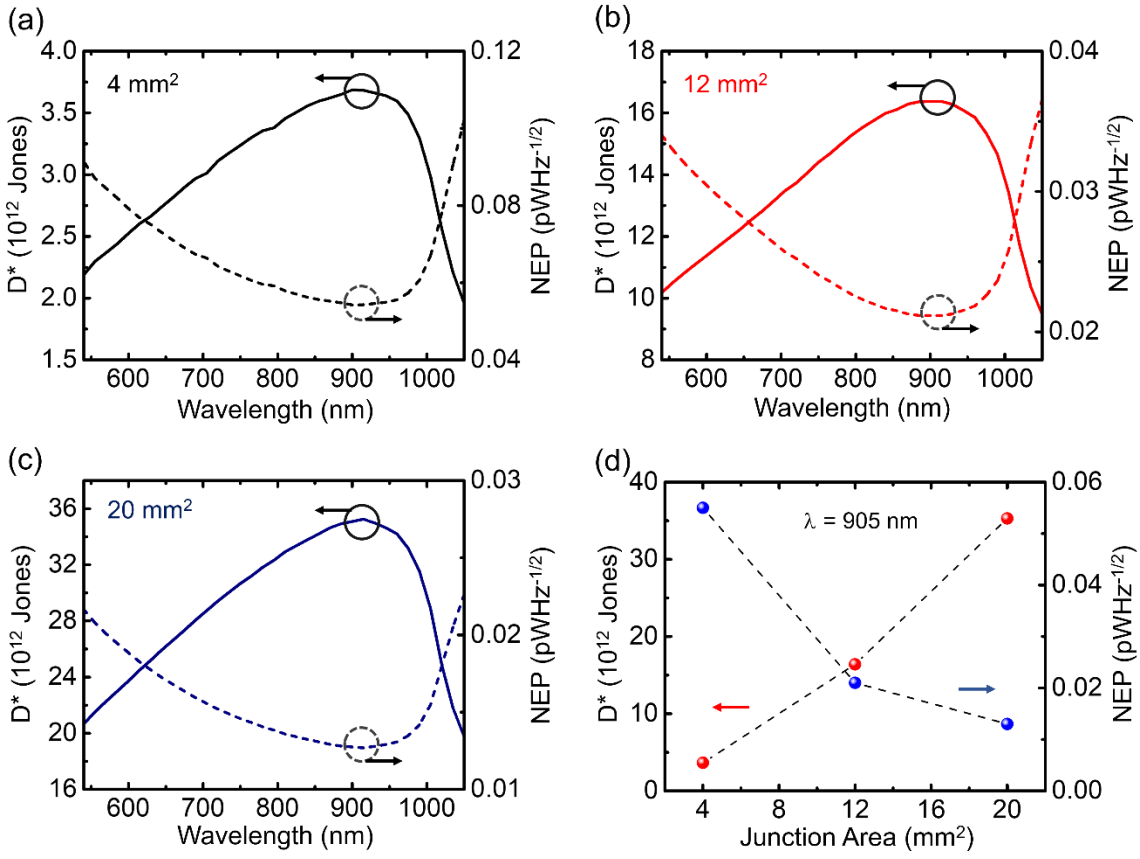

Figure 4.11. D^* and NEP as a function of wavelength at the fabricated Gr/n-Si photodiodes with junction area of (a) 4 mm^2, (b) 12 mm^2 and (c) 20 mm^2. (d) D^* and NEP of the devices at the peak wavelength of 905 nm at $V_b = 0$ V.

In agreement with the corresponding R values, the maximum D^* and minimum NEP values were found at 905 nm peak wavelength. At 905 nm, the results of the calculated D^* and NEP values with increasing junction area were also shown in Figure 4.11(d). With $D^* = 3.5 \times 10^{13}$ Jones and NEP = 0.013 $pWHz^{-1/2}$, the sample having a junction area of 20 mm^2 was determined to be the most sensitive one among other samples with smaller junction areas. These obtained results clearly showed that the detection limit of a Gr/n-Si photodiode can be improved simply by increasing its junction area without need of either external doping of the graphene electrode or interface modification of the Gr/n-Si heterojunction.

The variation in the I-V characteristics of our samples illuminated with different light power were displayed in the semi-logarithmic scale in Figure 4.12(a-c). All samples exhibit a clear photovoltaic activity under light illumination. In detail, semi-logarithmic scale I-V characteristics of our devices under the illumination of 905 nm wavelength light with 10 μW power is shown in Figure 4.12(d). The variation in V_{oc} and I_{sc} for each of the sample was plotted in Figure 4.12(e-f) as a function of the incident light power. As seen in Figure 4.12(e) and 4.12(f) although I_{sc} exhibits a clear linear response to the incident light, V_{oc} increases nonlinearly and converges to different saturation levels depending on the junction area as the incident light power exceeds 20 μW. Fitting the plots in Figure 4.12(f) with power law of $I_{sc} \sim P^{\theta}$, we extracted the factor θ determining the efficiency of photo-generated charges to incident light power. Linear increase of I_{sc} with the light power (where $0.98 \leq \theta \leq 1.03$) confirms that the photocurrent in all the samples is solely determined by the amount of photo-generated charge carriers. The nonlinear variation of V_{oc} with incident light power is typical for Gr/n-Si Schottky photodiodes and can be explained in terms of the quasi-Fermi level transport model including surface recombination mechanism as explained before. Consistent with the maximum R values, the measured I_{sc} had a linear dependence on the junction area. However, such a trend was not observed for the variation in V_{oc} values. As explained by the quasi-Fermi level transport model, V_{oc} generated in a heterojunction device is strongly governed by the magnitude of Φ_B. Therefore, the inconsistent change of V_{oc} with increasing junction area shown in Figure 4.12(e) can be directly correlated with the difference in Φ_B of the devices discussed previously.

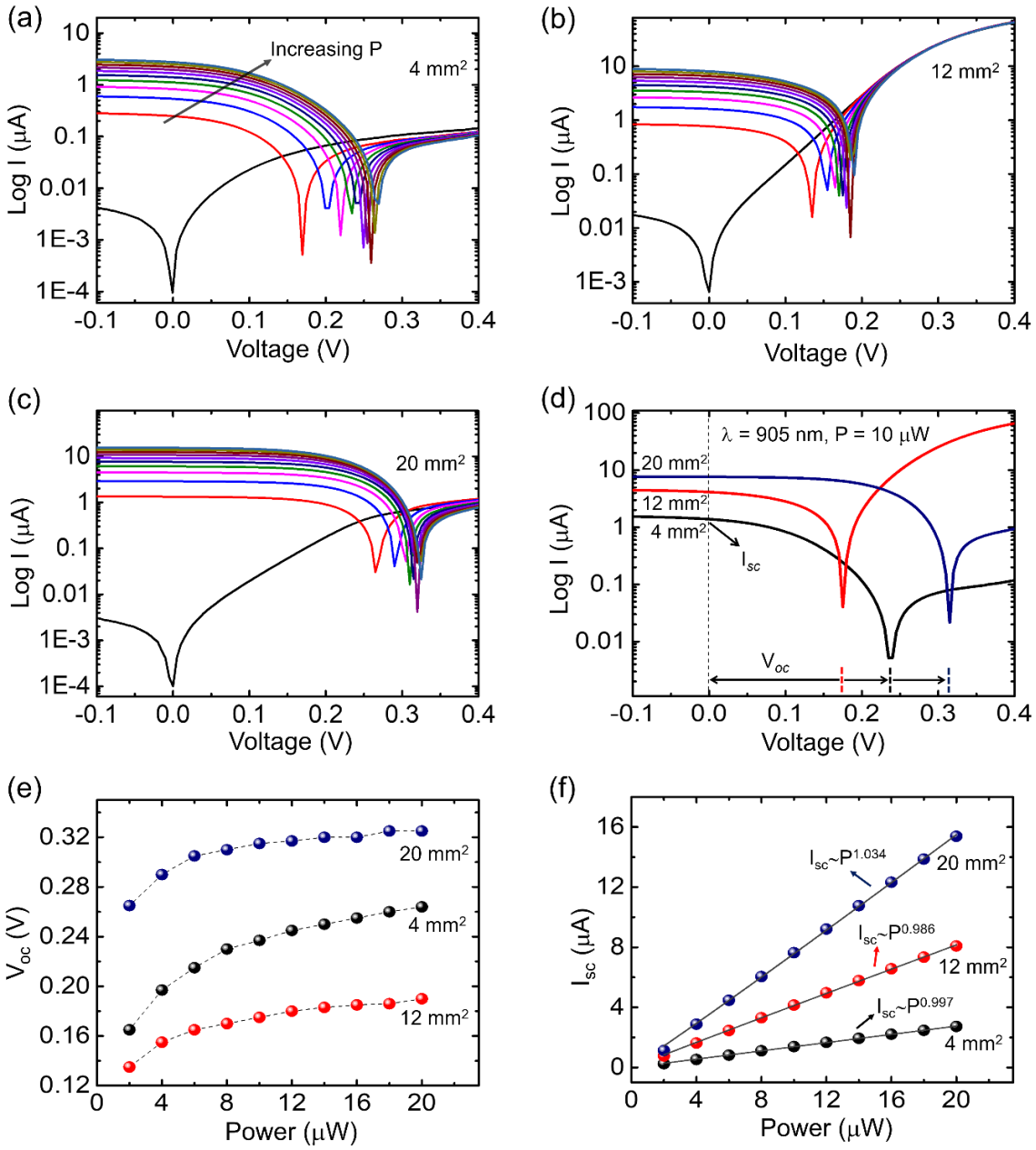

Figure 4.12. (a-c) I-V curves at dark and under the irradiation with light power changing from 2 μW to 20 μW. (d) Semi-logarithmic scale I-V characteristics of the devices under a constant light power of 10 μW at 905 nm. (e) V_{oc} and (f) I_{sc} of the fabricated Gr/n-Si photodiodes exposed to 905 nm wavelength light with different power densities. The curves in (f) are fitted by the power law.

In order to determine the response speed and 3-dB bandwidth (B_w) of our samples, we conducted time-resolved photocurrent measurements using the experimental set-up illustrated in Figure 4.13. For the measurements, a 940 nm wavelength collimated LED light source with a broad full width half maximum and a

905 nm laser line bandpass filter are used. The measurements were done for zero-bias condition and the photocurrent data were recorded under 905 nm wavelength light pulsed at 5 kHz frequency. The output photocurrent signal was converted to voltage with a transimpedance amplifier and then measured by an oscilloscope.

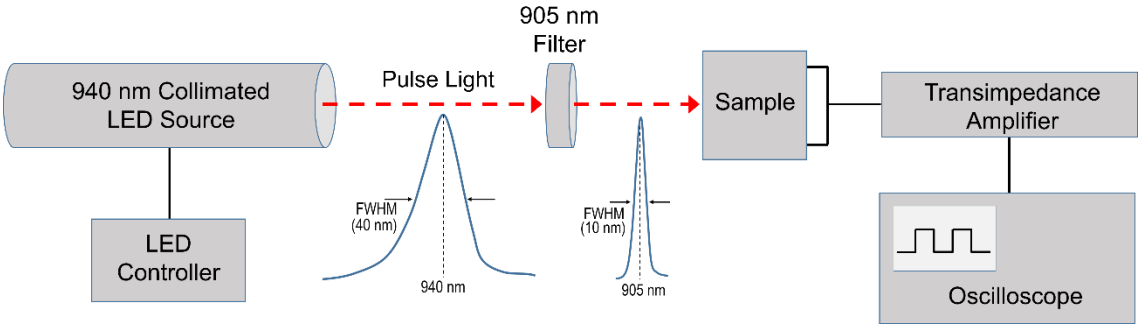

Figure 4.13. Schematic diagram of the time-resolved photocurrent measurement system.

Time-resolved photocurrent measurements, which were repeated over several on/off switching cycles within 1.0 ms. total time, showed that all the devices have excellent photocurrent reversibility and stability as seen in Figure 4.14.

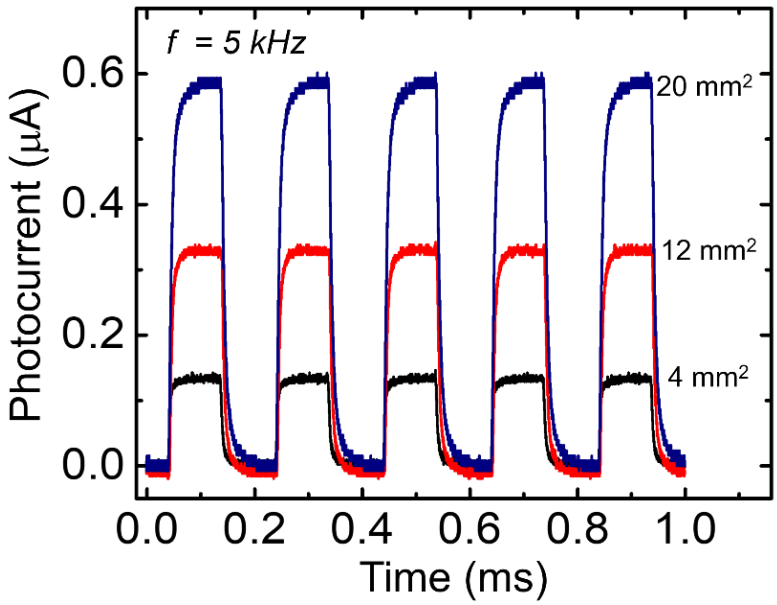

Figure 4.14. Time-resolved photocurrent spectrum of the Gr/n-Si photodiodes under fast varied light illumination (905 nm, ~ 1 μW) with a light switching frequency of 5 kHz at zero-bias voltage.

Rise time (t_r) and decay time (t_d) of each of the samples were determined from single pulse response measurements. Here t_r is defined as the range that the photocurrent rises from 10 to 90% of its maximum and t_d is defined similarly. Based on the obtained t_r and t_d values shown in Figure 4.15, we found that the response speed of our Gr/n-Si Schottky photodiodes decreases as the junction area increases. This is likely caused by the increased number of interface defects for larger junction area, which can act as carrier trapping centers. The slow release of trapped charge carriers results in a long decay edge. This phenomenon is more evident especially at low temperatures because of relatively low trapping energy levels (Lv et al., 2013). Rise time and 3-dB B_w are two closely-related parameters used to describe the limit of a circuit's capability to respond to abrupt changes in an input signal. The 3-dB B_w is related to the RC constant of the circuit and determines the operational speed of a photodetector (Lu et al., 2020). Using the relation $B_w = 0.35/t_r$ we also estimated the 3-dB B_w of the samples with 4, 12 and 20 mm^2 junction areas as 55, 31 and 22 kHz, respectively.

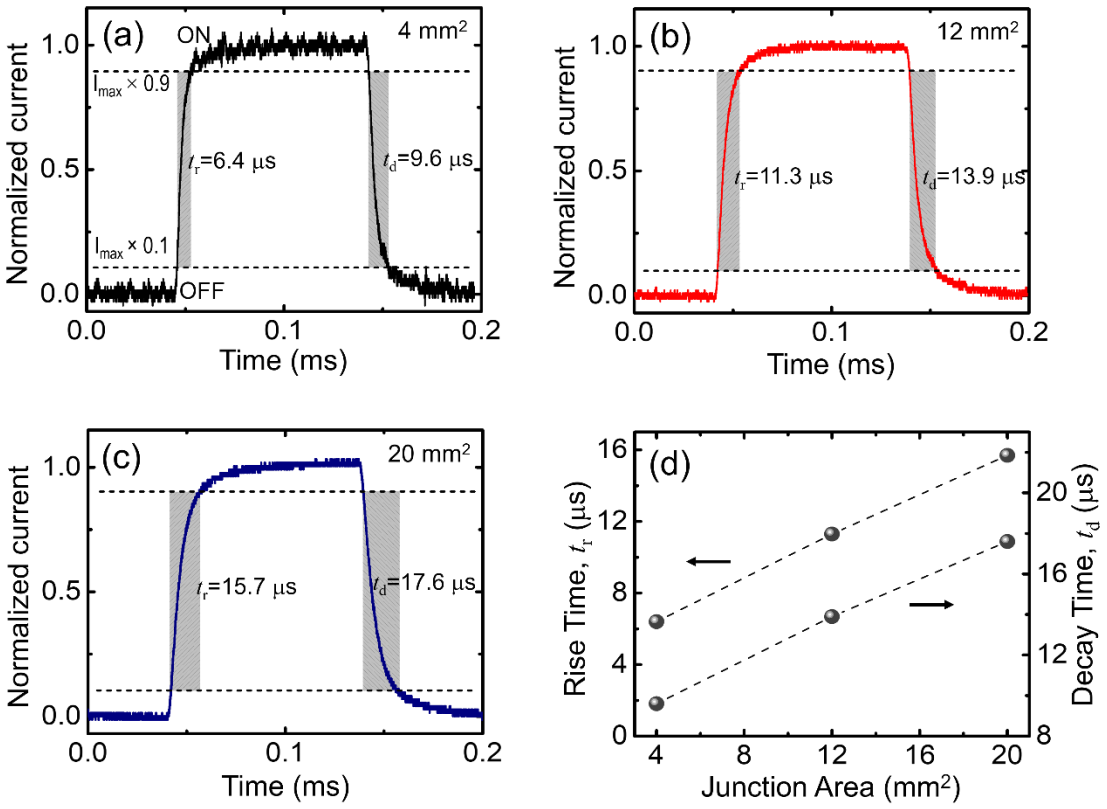

Figure 4.15. The 0.2 ms one cycle time-resolved photocurrent spectrum of the Gr/n-Si photodiodes under 905 nm wavelength at zero-bias voltage; depending on junction areas (a) 4 mm^2, (b) 12 mm^2 and (c) 20 mm^2. The measured photocurrents were normalized with the maximum values. (d) The t_r and t_d values of the devices as a function of junction area.

Considering the large junction area and relatively low conductivity of the graphene electrode, it is expected that the response speed of Gr/n-Si photodiodes can be remarkably improved by further optimizing the device design.

The performance parameters of Gr/n-Si photodiodes obtained in this work are compared in Table 4.1. Depending on the increasing junction area, the photodiode parameters including R, D^* and NEP are seemed to be improved. Compared to previously reported Gr/n-Si photodiodes (Xinming Li et al., 2016; Lv et al., 2013; An et al., 2013; Aydin et al., 2018), our device with the junction area of 20 mm^2 displayed excellent R, D^* and NEP values which are 0.76 AW^{-1}, 3.5 x 10^{13} Jones and 0.013 $pWHz^{-1/2}$, respectively. However, contrary to the improvement in such photodiode parameters, the device exhibited lower response speed due to larger junction area.

Table 4.1. The performance of the fabricated Gr/n-Si photodiodes under 905 nm wavelength light at 0 V bias.

Junction Area (mm^2)	R (AW^{-1})	I_d (nA)	D^* (Jones)	NEP ($pWHz^{-1/2}$)	t_r (μs)	t_d (μs)
4	0.16	0.24	0.37×10^{13}	0.055	6.4	9.6
12	0.47	0.31	1.64×10^{13}	0.021	11.3	13.9
20	0.76	0.29	3.53×10^{13}	0.013	15.7	17.6

4.3. Enhancing the Photo-response Characteristics of Graphene/n-Si based Schottky Barrier Photodiodes by Increasing the Number of Graphene Layers

In this study, the impact of the number of graphene layers on the spectral responsivity and response speed of Gr/n-Si based Schottky barrier photodiodes was investigated. Gr/n-Si photodiode devices were fabricated by transferring CVD grown monolayer graphene films one by one on n-Si substrates, reaching up to three graphene layers. Prior to electrical and optoelectronic measurements of the fabricated devices, the thickness of graphene layers and its optical transparency have been checked by Raman spectroscopy and optical transmittance measurements, respectively. After each monolayer graphene is transferred on n-Si substrate, the Raman measurements were performed on the samples in order to confirm its continuity and the thickness of

graphene, the average data is shown in Figure 4.16(a). In all the measurements, the typical graphene related D, G and 2D peaks were found at the peak wavelength of around 1350, 1588 and 2697 cm^{-1}, respectively. While the D peak is mainly associated with sp^3 defect sites and a structural disorder in graphene, G band peak indicates sp^2 bonded pairs of graphene and 2D peak confirms the ultimate nature of graphene. From the Raman spectrum of the devices, the large 2D to G peak intensity ratio ($I_{2D}/I_G > 1$) corresponds to the single-layer thickness of the graphene layer. While the $I_{2D}/I_G = 1$ represents the bilayers of graphene, $I_{2D}/I_G < 1$ and close to each other reveals that the grown graphene have three-layers (Ferrari et al., 2006; Y. Y. Wang et al., 2008). Figure 4.16(b) displays the optical transmittance values for a clean quartz and as well as graphene layers placed on its surface. The transmittance measurements were done under the irradiation at the fixed wavelength of 905 nm. Quartz substrate with the thickness of 10 mm have the transmittance value of 94 %. The increasing number of graphene layers on quartz sample reduces the optical transmittance by approximately 2 – 3 % per layer.

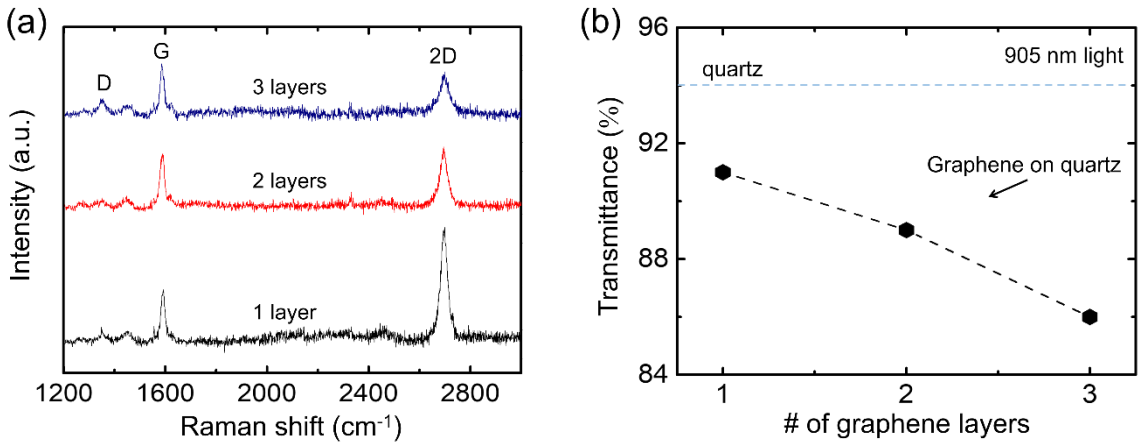

Figure 4.16. (a) Raman spectrum of three different graphene layers, (b) optical transmittance values as a function of increasing number of graphene films where a quartz was used as a substrate.

A schematic illustration of the fabricated Gr/n-Si Schottky barrier photodiode with electrical contacts is displayed in Figure 4.17(a). For comparison and verification, the electrical and optoelectronic characterizations were done on two individual samples which were labeled as Device-1 (D1) and Device-2 (D2). The devices have similar active junction areas of 20 mm^2. The I-V measurement of the samples were conducted under dark conditions with an applied bias voltage range between – 0.5 and 0.5 V. The experiments were repeated for an increasing number of graphene layers transferred on

the device structure shown in Figure 4.17(a). For both samples, all the obtained I-V curves exhibited typical rectifying Schottky contact behavior but with slightly different saturation current levels at reverse bias region as seen in Figure 4.17(b). This already suggest that the Schottky contact parameters (e.g., ideality factor, barrier height…etc.) and hence the rectification strength of the samples vary as a function of the number of graphene layers.

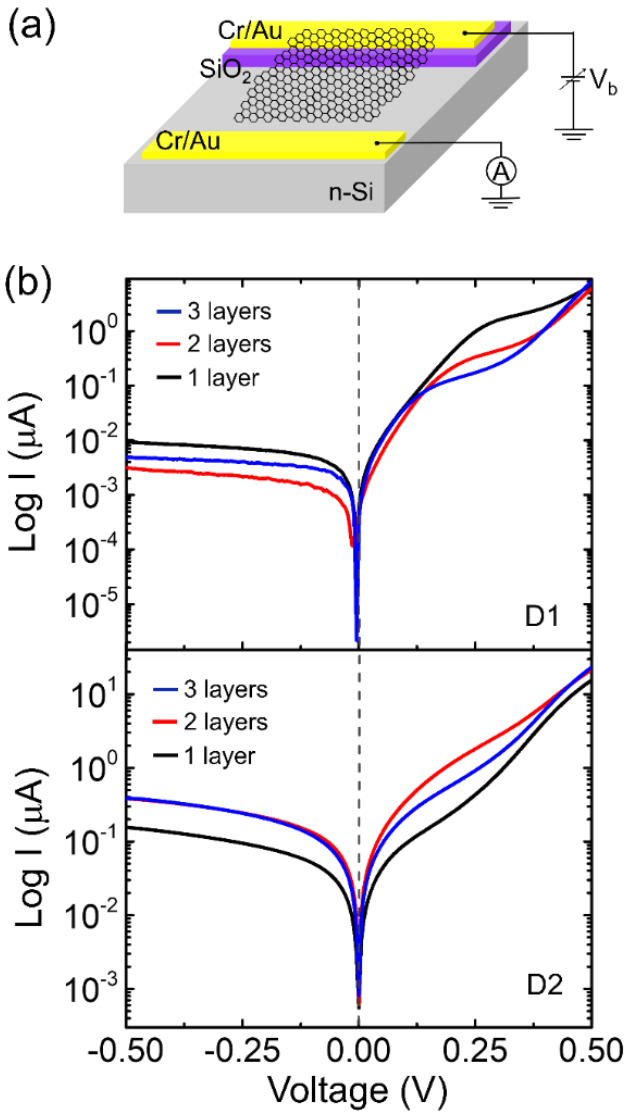

Figure 4.17. (a) Schematic structure of the fabricated Gr/n-Si photodiode with electrical connections. (b) Dark I-V measurements of the samples D1 and D2 in semi-logarithmic scale.

From the linear forward-bias region of the semi-logarithmic scale I-V plots in Figure 4.18(a), Φ_B of our devices were determined by using the method developed by Cheung et al., (Cheung and Cheung 1986) as mentioned in the section of 4.1. The obtained Φ_B

values were plotted as a function of the number of graphene layers in Figure 4.18(b). As can be seen in Fig. 4.18(b), the Φ_B of both devices increases as a function of graphene layers. For both devices, the increment of Φ_B was found to be 5 meV in average as the number of graphene layers reach to three-layers.

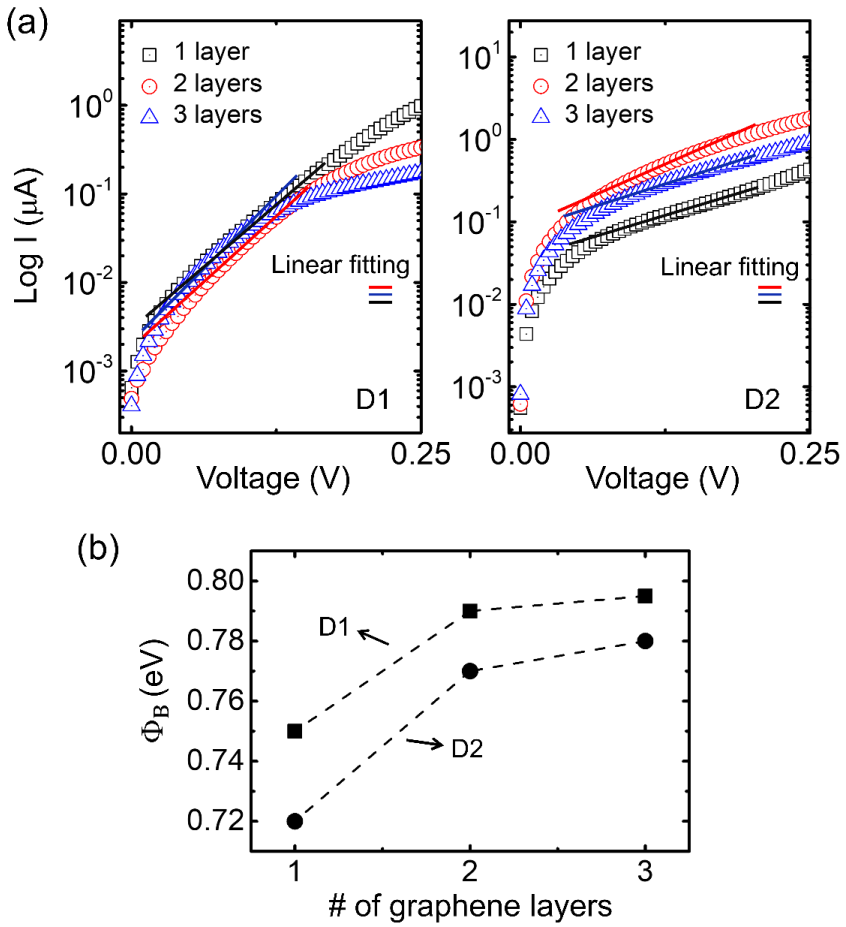

Figure 4.18. (a) The forward-bias regions of the I-V plots shown in Fig. 4.17(b), which were linearly fitted to calculate the Φ_B values of the samples D1 and D2. (b) The extracted Φ_B values of the devices vs the number of graphene layers.

In order to determine the zero-bias R of the samples we conducted wavelength-resolved photocurrent spectroscopy measurements under illumination of light with different wavelengths tuned between 540 nm to 1050 nm. The measurements were repeated for increased number of graphene layers on the device structure and the results were plotted in Figure 4.19(a) and (b). For a clear comparison, the maximum R values at 905 nm wavelength were plotted in Figure 4.19(c) as a function of the number of graphene layers. The maximum R of the sample D1 rises from 0.65 AW^{-1} to 0.75 AW^{-1}

when the number of graphene layers is increased from 1 to 3. And for the sample D2 the maximum R was found to be rising from 0.59 AW^{-1} to about 0.72 AW^{-1}. For both samples, the R values seemed to be converging to a saturation level in the case of three graphene layers used as the hole-collecting electrode.

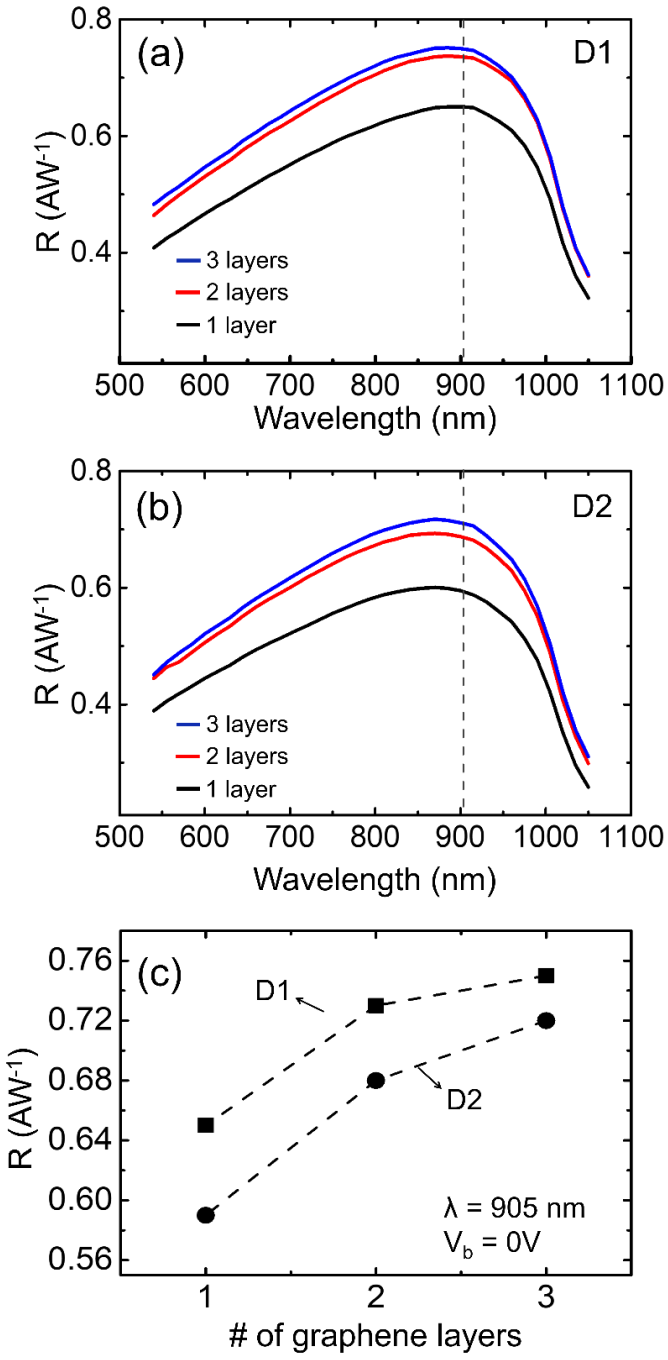

Figure 4.19. (a) and (b) are the zero-bias spectral responsivity of the devices D1 and D2 measured in the wavelength range between 540 nm to 1050 nm at zero bias voltage, respectively. (c) Comparison of the zero-bias spectral responsivity of the two individual devices acquired at the peak wavelength of 905 nm.

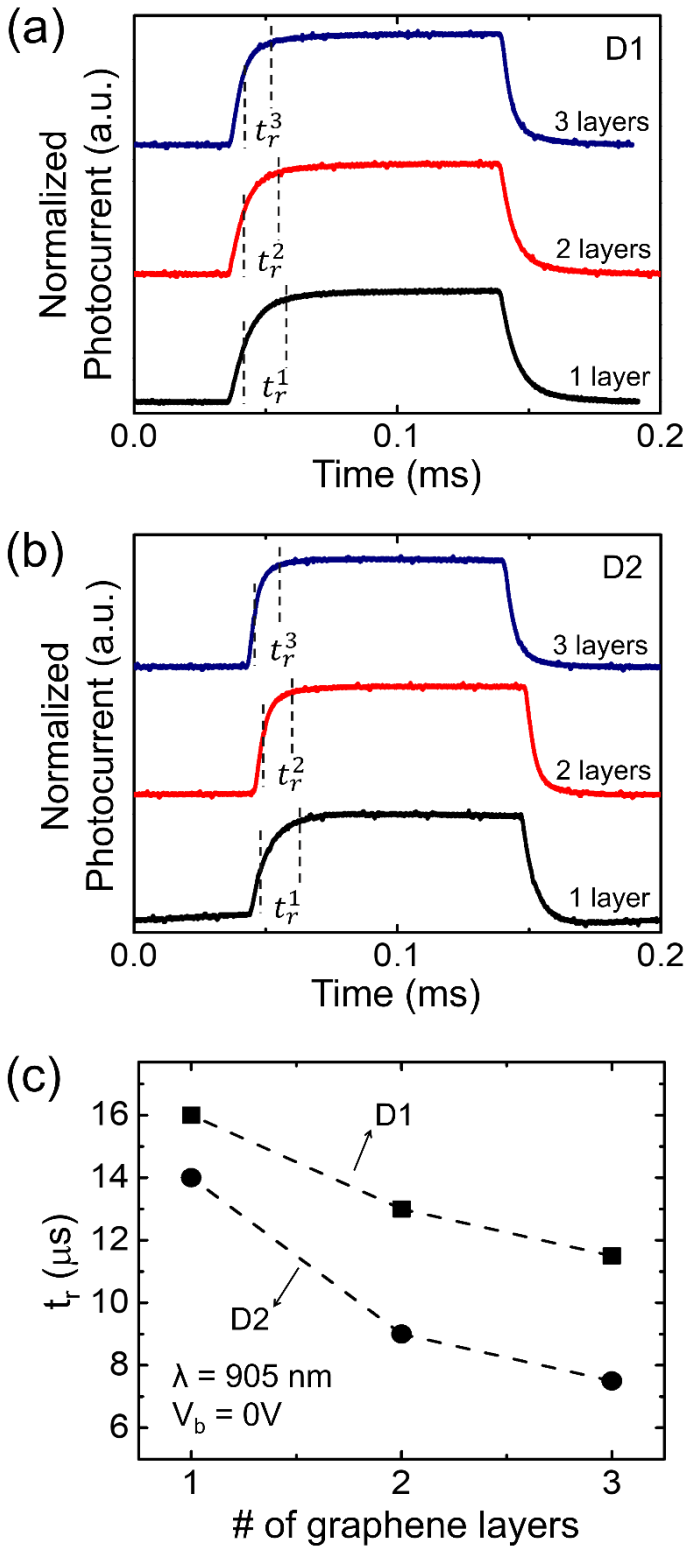

Figure 4.20. (a-b) The time-dependent photocurrent spectrum of the fabricated Gr/n-Si photodiodes D1 and D2, respectively. One cycle time-dependent photocurrent spectrum of the devices under fast varied 905 nm wavelength light with switching frequency of 5 kHz at zero-bias voltage. The measured photocurrents were normalized with the maximum values. (c) The rise time values of the devices as a function of the number of graphene layers.

Time-dependent photocurrent spectroscopy measurements were performed to determine the response speed of the fabricated devices as a function of the number of graphene layers. The measurements were carried out one-cycle switching on/off within 0.2 ms. as seen in Figure 4.20(a) and (b). All the samples with different number of graphene layers exhibited great capability to respond high frequency pulsed light and on/off switching stability. To determine the response speed of the sample with different number of graphene layers, the t_r values were extracted from single pulse response measurements. As seen in Figure 4.20(c) the response speed of the samples increases with the number of graphene layers.

The variation in the spectral responsivity and response speed of Gr/n-Si photodiodes with the number of graphene layers can be explained in terms of the electronic transport characteristics of graphene electrode and charge injection dynamics. The sheet resistance (R_s) and carrier density (n) of the graphene electrode were determined as a function of the number of graphene layers using four probe and Hall effect measurement techniques. For the transport experiments, the grown graphene layers were transferred on square-shaped quartz substrates having Cr/Au metallic contact pads at their corners. The measurements were carried out on two individual samples and repeated for increased number of graphene layers. All the samples exhibited p-type conductivity with initial hole density ranging between 1.2×10^{13} cm^{-2} and 3.2×10^{13} cm^{-2} in the case of one-layer graphene. As shown in Figure 4.21(a) and (b), the hole density of the samples was identified to be increasing linearly as a function of the number of graphene layers. However, the sheet resistance of the samples first decreases sharply as the number of graphene layers is increased from 1 to 2 and then converges to a saturation level for three graphene layers. As depicted in Figure 4.21(c) the Fermi level of graphene is lowered relative to its initial stage when 2 and/or 3 graphene layers are used as electrode due to increased hole density. The shift of Fermi level towards lower energy states increases the work function of graphene electrode and as well as the magnitude of the built-in potential and junction electric field at the Gr/n-Si interface. This promotes greatly the effective separation of the photo-generated charge carriers at the depletion region and enhances the photocurrent of the device. Therefore, the spectral responsivity and response speed of the samples are expected to rise as a function of the number of graphene layers in agreement with increasing hole density shown in Figure 4.21(a-b). The experimentally observed deviation of these two

photodiode parameters from linearity can be correlated with the nonlinear decrease in the series resistance of the device.

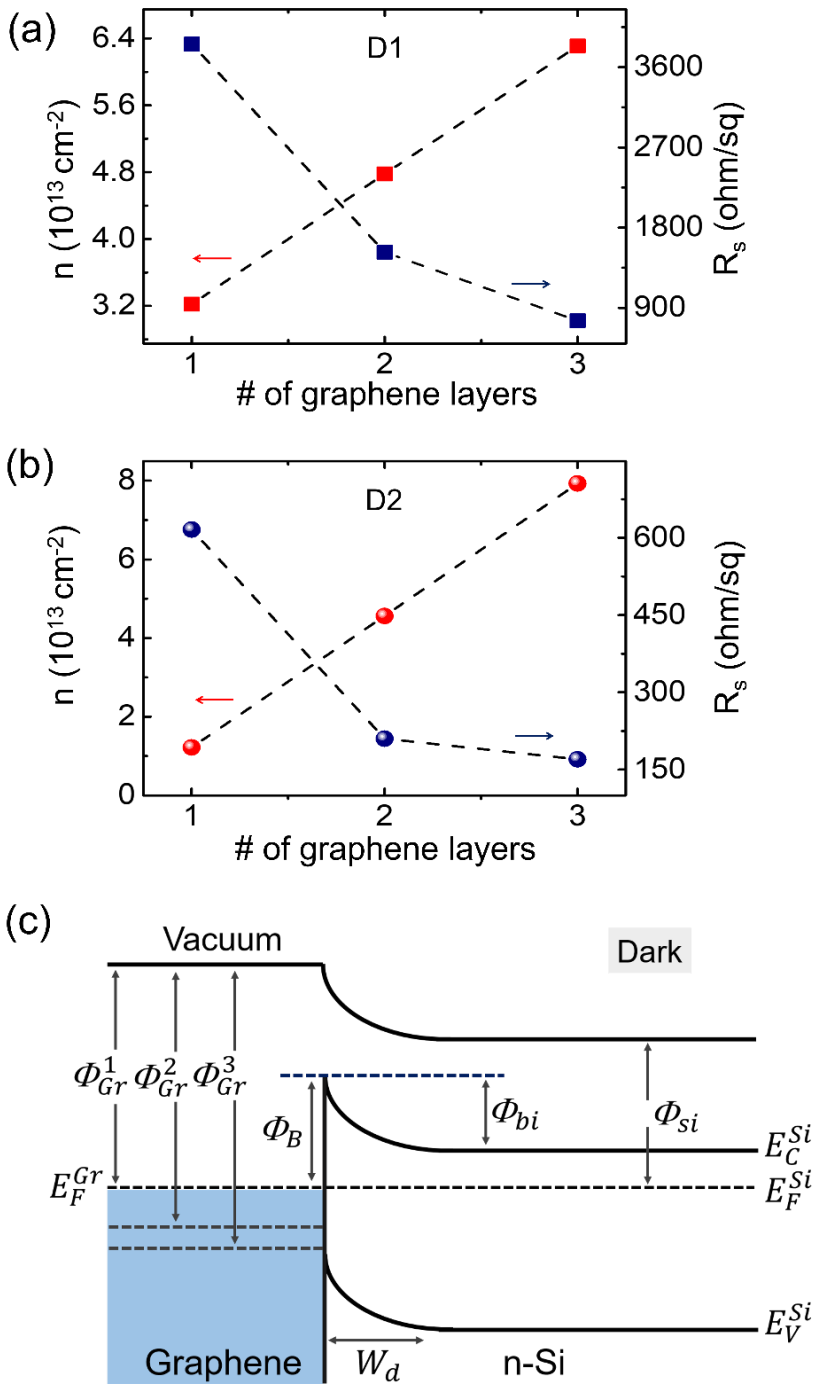

Figure 4.21. (a-b) Charge carrier concentration and sheet resistance vs the number of graphene layers for the devices D1 and D2, respectively. (c) The schematic illustration of the energy band diagram for the Gr/n-Si Schottky junction photodiode as a function of increasing the number of graphene layers. Φ_{Gr} and Φ_B are the work function of graphene electrode and the Schottky barrier height at the Gr/n-Si heterojunction, respectively.

CHAPTER 5

CONCLUSION

This thesis is focused on the enhancement of the device performance parameters for Gr/n-Si based near-infrared Schottky photodiodes. For the experimental works, the devices were produced by transferring CVD grown monolayer graphene films onto n-Si substrates, and their electrical and optoelectronic measurements were performed to determine typical diode characteristics such as Schottky barrier height, ideality factor, spectral responsivity and response speed etc. The dark current-voltage (I-V) measurement of the samples exhibited excellent rectifying character of a typical Schottky diode. The spectral response measurements of Gr/n-Si devices were done in the wavelength range between 540 nm and 1050 nm. For all the samples, the maximum spectral response was measured at a peak wavelength of 905 nm. Afterwards, power-dependent I-V measurements were carried out in order to get open-circuit voltage and photocurrent values of the devices under the illumination of 905 nm wavelength light. All devices showed clear photovoltaic activity under light illumination. Based on the experimental findings, the fabricated Gr/n-Si photodiode was exposed to 905 nm wavelength light with different power densities and then the light-induced modification of the Schottky barrier height at the interface of the sample was examined in Chapter 4.1. Subsequently, some critical experimental approaches were employed to improve the spectral response and response speed of the Gr/n-Si devices discussed in Chapter 4.2 and Chapter 4.3 in detail. The results of the experiments were summarized in following.

In Chapter 4.1, the effect of incident light on the SBH in Gr/n-Si Schottky photodiodes were investigated. The optoelectronic transport measurements conducted at room temperature showed that light illumination increases the hole carrier density in p-type CVD grown graphene and hence shifts its Fermi level relative to that of n-Si substrate. Because of light induced shift in graphene's Fermi level, the SBH of Gr/n-Si heterojunction was determined to be increasing nonlinearly from 0.7 eV to 0.9 eV when the light power density is boosted from 0 to 200 $\mu W/cm^2$. The experimentally observed nonlinear behavior of the SBH is interpreted within the framework of two-step Shockley-Read-Hall model considering the charge recombination processes through

mid-gap and interface states at the Gr/n-Si heterojunction. At relatively low light power densities (e.g., $P < 10$ $\mu W/cm^2$), the charge recombination in Gr/n-Si photodiodes was found to be mainly dominated by the mid-gap states in n-Si substrate. However, in the case of higher light power densities exceeding 10 $\mu W/cm^2$, the charge recombination throughout the interface states becomes dominant. The combination of these two distinct recombination processes was identified to be the main reason for the experimentally determined nonlinear variation of the SBH in Gr/n-Si heterojunction devices. Light induced tunability of SBH at the graphene/semiconductor heterojunction is of great importance especially for the development of new generation optically driven devices in which graphene acts as a functioning element.

In Chapter 4.2, the effect of junction area on the device characteristics of Gr/n-Si Schottky photodiodes were also investigated. A set of photovoltaic type photodiode samples with different junction areas (e.g., 4 mm^2, 12 mm^2 and 20 mm^2) was fabricated by transferring monolayer CVD grown graphene on n-Si substrate. The devices exhibiting rectification behavior have been examined in terms of their spectral response, specific detectivity, noise equivalent power and response speed under self-powered condition. The measurements showed that, in contrast to their response speed, the spectral response of Gr/n-Si based photodiodes increases linearly as a function of the junction area. A maximum spectral response of 0.76 AW^{-1} is achieved at 905 nm peak wavelength for 20 mm^2 junction area which is the highest value reported in the literature for Gr/n-Si based Schottky photodiodes operating under zero-bias condition. With specific detectivity of 3.5×10^{13} Jones and noise equivalent power of 0.013 $pWHz^{-1/2}$, the sample having a junction area of 20 mm^2 was determined to be the most sensitive one among other samples with smaller junction areas. These obtained results clearly showed that the detection limit of a Gr/n-Si photodiode can be improved simply by increasing its junction area.

In Chapter 4.3, the impact of number of graphene layers on the spectral responsivity and response speed of Gr/n-Si photodiodes were investigated. Herein, the devices were fabricated by transferring monolayer graphene layers one by one on n-Si substrates, reaching up to 3 graphene layers in total. Wavelength-resolved and time-dependent photocurrent measurements demonstrated that both spectral responsivity and response speed are enhanced as the number of graphene layers is increased from 1 to 3 on n-Si substrates. For example, the spectral responsivity and the response speed of the fabricated device was found to be improved about 15 % (e.g., from 0.65 AW^{-1} to 0.75

AW^{-1}) and 50 % (e.g., 14 μs to 7 μs), respectively when 3 graphene layers are used as the hole collecting cathode electrode. The experimentally obtained results showed that the device parameters such as spectral responsivity and response speed of Gr/n-Si Schottky barrier photodiodes can be boosted simply by increasing the number of graphene layers on n-Si substrates. This study is expected to provide useful information for the realization of high-performance graphene/semiconductor-based Schottky barrier photodiodes with improved photo-detection capability.

To summarize, the obtained experimental findings suggest that the photo-sensitivity of these type of photodiodes can be improved simply by not only increasing their junction area but also the number of graphene layers without need of either external doping of the graphene electrode or interface modification of the Gr/n-Si heterojunction. This thesis may serve towards the standardization of junction area and/or graphene layer thickness for the development of high performance self-powered Gr/Si based optoelectronic devices such as solar cells and photodetectors operating in between ultraviolet and near-infrared spectral regions.

REFERENCES

An, X., F. Liu, Y. J. Jung, and S. Kar (2013). Tunable Graphene-Silicon Heterojunctions for Ultrasensitive Photodetection. *Nano Letters* 13(3), 909–916.

Arefinia, Z., and A. Asgari (2014). A New Modeling Approach for Graphene Based Silicon Nanowire Schottky Junction Solar Cells. *Journal of Renewable and Sustainable Energy* 6(4), 043132.

Arefinia, Z., and A. Asgari (2015). An Analytical Model for Optimizing the Performance of Graphene Based Silicon Schottky Barrier Solar Cells. *Materials Science in Semiconductor Processing* 35, 181–188.

Aydin, H., S. B. Kalkan, C. Varlikli, and C. Celebi (2018). P3HT-Graphene Bilayer Electrode for Schottky Junction Photodetectors. *Nanotechnology* 29(14), 145502.

Bae, S., H. Kim, Y. Lee, X. Xu, J. S. Park, Y. Zheng, J. Balakrishnan, et al., (2010). Roll-to-Roll Production of 30-Inch Graphene Films for Transparent Electrodes. *Nature Nanotechnology* 5(8), 574–578.

Bao, Q., and K. P. Loh (2012). Graphene Photonics, Plasmonics, and Broadband Optoelectronic Devices. *ACS Nano* 6(5), 3677–3694.

Bardeen, J. (1947). Surface States and Rectification at a Metal Semi-Conductor Contact. *Physical Review* 71(10), 717.

Bartolomeo, A. Di. (2016). Graphene Schottky Diodes: An Experimental Review of the Rectifying Graphene/Semiconductor Heterojunction. *Physics Reports* 606, 1–58.

Bartolomeo, A. Di., F. Giubileo, G. Luongo, L. Iemmo, N. Martucciello, G. Niu, M. Fraschke, O. Skibitzki, T. Schroeder, and G. Lupina (2017). Tunable Schottky Barrier and High Responsivity in Graphene/Sinanotip Optoelectronic Device. *2D Materials* 4(1), 015024.

Bethe, H. A. (1991). Theory of the Boundary Layer of Crystal Rectifiers. In *Semiconductor Devices: Pioneering Papers*, 387–399.

Blake, P., E. W. Hill, A. H. Castro Neto, K. S. Novoselov, D. Jiang, R. Yang, T. J. Booth, and A. K. Geim (2007). Making Graphene Visible. *Applied Physics Letters* 91(6), 063124.

Bolotin, K. I., K. J. Sikes, Z. Jiang, M. Klima, G. Fudenberg, J. Hone, P. Kim, and H. L. Stormer (2008). Ultrahigh Electron Mobility in Suspended Graphene. *Solid State Communications* 146(9-10), 351–355.

Bonaccorso, F., Z. Sun, T. Hasan, and A. C. Ferrari (2010). Graphene Photonics and Optoelectronics. *Nature Photonics* 4, 611–622.

Braun, F. (1875). Ueber Die Stromleitung Durch Schwefelmetalle. *Annalen Der Physik*.

Card, H. C., and E. H. Rhoderick (1971). Studies of Tunnel MOS Diodes I. Interface Effects in Silicon Schottky Diodes. *Journal of Physics D: Applied Physics* 4(10), 1589.

Castro Neto, A. H., F. Guinea, N. M.R. Peres, K. S. Novoselov, and A. K. Geim (2009). The Electronic Properties of Graphene. *Reviews of Modern Physics* 81(1), 109.

Çelebi, C., C. Yanik, A. G. Demirkol, and I. I. Kaya (2012). The Effect of a SiC Cap on the Growth of Epitaxial Graphene on SiC in Ultra High Vacuum. *Carbon* 50(8), 3026–3031.

Chen, C. C., M. Aykol, C. C. Chang, A. F.J. Levi, and S. B. Cronin (2011). Graphene-Silicon Schottky Diodes. *Nano Letters* 11(5), 1863–1867.

Cheung, S. K., and N. W. Cheung (1986). Extraction of Schottky Diode Parameters from Forward Current-Voltage Characteristics. *Applied Physics Letters* 49(2), 85–87.

Cowley, A. M., and S. M. Sze (1965). Surface States and Barrier Height of Metal-Semiconductor Systems. *Journal of Applied Physics* 36(10), 3212–3220.

Crowell, C. R., and V. L. Rideout (1969). Normalized Thermionic-Field (T-F) Emission in Metal-Semiconductor (Schottky) Barriers. *Solid State Electronics* 12(2), 89–105.

Dash, G. N., S. R. Pattanaik, and S. Behera (2014). Graphene for Electron Devices: The Panorama of a Decade. *IEEE Journal of the Electron Devices Society* 2(5), 77-104.

Donald A. Neamen (2006). *Semiconductor Physics and Devices : Basic Principles 1 Donald A. Neamen. - 3rd Ed. P. McGraw-Hill Companies, Inc.,*.

Fang, T., A. Konar, H. Xing, and D. Jena (2007). Carrier Statistics and Quantum Capacitance of Graphene Sheets and Ribbons. *Applied Physics Letters* 91(9), 092109.

Ferrari, A. C., J. C. Meyer, V. Scardaci, C. Casiraghi, M. Lazzeri, F. Mauri, S. Piscanec, et al., (2006). Raman Spectrum of Graphene and Graphene Layers. *Physical Review Letters* 97(18), 187401.

Fidan, M., Ö. Ünverdi, and C. Çelebi (2021). Junction Area Dependent Performance of Graphene/Silicon Based Self-Powered Schottky Photodiodes. *Sensors and Actuators, A: Physical* 331, 112829.

Geim, A. K., and K. S. Novoselov (2009). The Rise of Graphene. In *Nanoscience and Technology: A Collection of Reviews from Nature Journals*, pp 11–19.

Heer, W. A. D., C. Berger, M. Ruan, M. Sprinkle, X. Li, Y. Hu, B. Zhang, J. Hankinson, and E. Conrad (2011). Large Area and Structured Epitaxial Graphene Produced by Confinement Controlled Sublimation of Silicon Carbide. *Proceedings of the National Academy of Sciences of the United States of America* 108(41), 16900–16905.

Hökelek, E., and G. Y. Robinson (1983). A Study of Schottky Contacts on Indium Phosphide. *Journal of Applied Physics* 54(9), 5199–5205.

Jorio, A. (2012). Raman Spectroscopy in Graphene-Based Systems: Prototypes for Nanoscience and Nanometrology. *ISRN Nanotechnology* 2012, 16 pages.

Kim, H. Y., K. Lee, N. McEvoy, C. Yim, and G. S. Duesberg (2013). Chemically Modulated Graphene Diodes. *Nano Letters* 13(5), 2182–2188.

Kim, K. S., Y. Zhao, H. Jang, S. Y. Lee, J. M. Kim, K. S. Kim, J. H. Ahn, P. Kim, J. Y. Choi, and B. H. Hong (2009). Large-Scale Pattern Growth of Graphene Films for Stretchable Transparent Electrodes. *Nature* 457(7230), 706–710.

Kosonocky, W. F. (1991). Review of Infrared Image Sensors with Schottky-Barrier Detectors. *Optoelectronics-Devices and Technologies* 6, 173–203.

Koster, L. J. A., V. D. Mihailetchi, R. Ramaker, and P. W.M. Blom (2005). Light Intensity Dependence of Open-Circuit Voltage of Polymer:Fullerene Solar Cells. *Applied Physics Letters* 86(12), 123509.

Kravets, V. G., A. N. Grigorenko, R. R. Nair, P. Blake, S. Anissimova, K. S. Novoselov, and A. K. Geim (2010). Spectroscopic Ellipsometry of Graphene and an Exciton-Shifted van Hove Peak in Absorption. *Physical Review B - Condensed Matter and Materials Physics* 81(15), 155413.

Li, X., H. Zhu, K. Wang, A. Cao, J. Wei, C. Li, Y. Jia, Z. Li, X. Li, and D. Wu (2010). Graphene-on-Silicon Schottky Junction Solar Cells. *Advanced Materials* 22(25), 2743–2748.

Li, X., M. Zhu, M. Du, Z. Lv, L. Zhang, Y. Li, Y. Yang, et al., (2016). High Detectivity Graphene-Silicon Heterojunction Photodetector. *Small* 12(5), 595–601.

Li, X., W. Cai, J. An, S. Kim, J. Nah, D. Yang, R. Piner, et al., (2009). Large-Area Synthesis of High-Quality and Uniform Graphene Films on Copper Foils. *Science* 324(5932), 1312–1314.

Lillington, D. R., and W. G. Townsend (1976). Effects of Interfacial Oxide Layers on the Performance of Silicon Schottky-Barrier Solar Cells. *Applied Physics Letters* 28(2), 97–98.

Liu, F., and S. Kar (2014). Quantum Carrier Reinvestment-Induced Ultrahigh and Broadband Photocurrent Responses in Graphene-Silicon Junctions. *ACS Nano* 8(10), 10270–10279.

Loginova, E., N. C. Bartelt, P. J. Feibelmarr, and K. F. McCarty (2009). Factors Influencing Graphene Growth on Metal Surfaces. *New Journal of Physics* 11(6), 063046.

Lu, Z., Y. Xu, Y. Yu, K. Xu, J. Mao, G. Xu, Y. Ma, D. Wu, and J. Jie (2020). Ultrahigh Speed and Broadband Few-Layer MoTe2/Si 2D–3D Heterojunction-Based Photodiodes Fabricated by Pulsed Laser Deposition. *Advanced Functional Materials* 30(9), 1907951.

Lv, P., X. Zhang, X. Zhang, W. Deng, and J. Jie (2013). High-Sensitivity and Fast-Response Graphene/Crystalline Silicon Schottky Junction-Based near-IR Photodetectors. *IEEE Electron Device Letters* 34(10), 1337–1339.

Mak, K. F., L. Ju, F. Wang, and T. F. Heinz (2012). Optical Spectroscopy of Graphene: From the Far Infrared to the Ultraviolet. *Solid State Communications* 152(15), 1341–1349.

Miao, X., S. Tongay, M. K. Petterson, K. Berke, A. G. Rinzler, B. R. Appleton, and A. F. Hebard (2012). High Efficiency Graphene Solar Cells by Chemical Doping. *Nano Letters* 12(6), 2745–2750.

Mishra, N., J. Boeckl, N. Motta, and F. Iacopi (2016). Graphene Growth on Silicon Carbide: A Review. *Physica Status Solidi (A) Applications and Materials Science* 213(9), 2277–2289.

Molitor, F., J. Güttinger, C. Stampfer, S. Dröscher, A. Jacobsen, T. Ihn, and K. Ensslin (2011). Electronic Properties of Graphene Nanostructures. *Journal of Physics Condensed Matter* 23(24), 243201.

Monch, W. (1990). On the Physics of Metal-Semiconductor Interfaces. *Reports on Progress in Physics* 53(3), 221.

Mott, N. F. (1938). Note on the Contact between a Metal and an Insulator or Semi-Conductor. *Mathematical Proceedings of the Cambridge Philosophical Society* 34(4), 568–572.

Muñoz, R., and C. G. -Aleixandre (2013). Review of CVD Synthesis of Graphene. *Chemical Vapor Deposition* 19(10-11-12), 297–322.

Murata, Y., S. Nie, A. Ebnonnasir, E. Starodub, B. B. Kappes, K. F. McCarty, C. V. Ciobanu, and S. Kodambaka (2012). Growth Structure and Work Function of Bilayer Graphene on Pd(111). *Physical Review B* 85(20), 205443.

Nair, R. R., P. Blake, A. N. Grigorenko, K. S. Novoselov, T. J. Booth, T. Stauber, N. M R Peres, and A. K. Geim (2008). Fine Structure Constant Defines Visual Transparency of Graphene. *Science* 320(5881), 1308–1308.

Novoselov, K. S., A. K. Geim, S. V. Morozov, D. Jiang, M. I. Katsnelson, I. V. Grigorieva, S. V. Dubonos, and A. A. Firsov (2005). Two-Dimensional Gas of Massless Dirac Fermions in Graphene. *Nature* 438(7065), 197–200.

Padovani, F. A., and R. Stratton (1966). Field and Thermionic-Field Emission in Schottky Barriers. *Solid State Electronics* 9(7), 695–707.

Parui, S., R. Ruiter, P. J. Zomer, M. Wojtaszek, B. J. Van Wees, and T. Banerjee (2014). Temperature Dependent Transport Characteristics of Graphene/n-Si Diodes. *Journal of Applied Physics* 116(24), 244505.

Pelella, A., A. Grillo, E. Faella, G. Luongo, M. B. Askari, and A. Di Bartolomeo (2021). Graphene-Silicon Device for Visible and Infrared Photodetection. *ACS Applied Materials and Interfaces* 13(40), 47895–47903.

Periyanagounder, D., P. Gnanasekar, P. Varadhan, J. H. He, and J. Kulandaivel (2018). High Performance, Self-Powered Photodetectors Based on a Graphene/Silicon Schottky Junction Diode. *Journal of Materials Chemistry C* 6(35), 9545–9551.

Philip W. H. S., and D. Akinwande (2011). *Carbon Nanotube and Graphene Device Physics*. Cambridge University Press.

Pimenta, M. A., G. Dresselhaus, M. S. Dresselhaus, L. G. Cançado, A. Jorio, and R. Saito (2007). Studying Disorder in Graphite-Based Systems by Raman Spectroscopy. *Physical Chemistry Chemical Physics* 9(11), 1276–1290.

Qin, F., C. Xu, G. Zhu, F. Chen, R. Wang, J. Lu, D. You, X. Wang, W. Zhang, and J. Zhao (2019). Brightness Improvement in a Graphene Inserted GaN/ZnO Heterojunction Light Emitting Diode. *Journal of Physics D: Applied Physics* 52(39), 395104.

Ranade, A. K., R. D. Mahyavanshi, P. Desai, M. Kato, M. Tanemura, and G. Kalita (2019). Ultraviolet Light Induced Electrical Hysteresis Effect in Graphene-GaN Heterojunction. *Applied Physics Letters* 114(15), 151102.

Reich, S., J. Maultzsch, C. Thomsen, and P. Ordejón (2002). Tight-Binding Description of Graphene. *Physical Review B* 66(3), 035412.

Riazimehr, S., A. Bablich, D. Schneider, S. Kataria, V. Passi, C. Yim, G. S. Duesberg, and M. C. Lemme (2016). Spectral Sensitivity of Graphene/Silicon Heterojunction Photodetectors. *Solid-State Electronics* 115, 207–212.

Riazimehr, S., S. Kataria, R. Bornemann, P. H. Bolívar, F. J. G. Ruiz, O. Engström, A. Godoy, and M. C. Lemme (2017). High Photocurrent in Gated Graphene-Silicon Hybrid Photodiodes. *ACS Photonics* 4(6), 1506–1514.

Riazimehr, S., S. Kataria, J. M. Gonzalez-Medina, S. Wagner, M. Shaygan, S. Suckow, F. G. Ruiz, O. Engström, A. Godoy, and M. C. Lemme (2019). High Responsivity and Quantum Efficiency of Graphene/Silicon Photodiodes Achieved by Interdigitating Schottky and Gated Regions. *ACS Photonics* 6(1), 107–115.

Saeed, M., Y. Alshammari, S. A. Majeed, and E. Al-Nasrallah (2020). Chemical Vapour Deposition of Graphene—Synthesis, Characterisation, and Applications: A Review. *Molecules* 25(17), 3856.

Şahan, N., M. Fidan, and C. Çelebi (2020). Adsorbate-Induced Enhancement of the Spectral Response in Graphene/Silicon-Based Schottky Barrier Photodetectors. *Applied Physics A* 126(12), 1–6.

Sarma, S. D., S. Adam, E. H. Hwang, and E. Rossi (2011). Electronic Transport in Two-Dimensional Graphene. *Reviews of Modern Physics* 83(2), 407.

Schottky, W. (1938). Halbleitertheorie Der Sperrschicht. *Die Naturwissenschaften* 26, 843.

Schroder, D. K. (2006). Semiconductor Material and Device Characterization, John Wiley&Sons. *Inc., Publication, Canada*.

Shockley, W. (1949). The Theory of p-n Junctions in Semiconductors and p-n Junction Transistors. *Bell System Technical Journal* 28(3), 435–489.

Singh, A., M. A. Uddin, T. Sudarshan, and G. Koley (2014). Tunable Reverse-Biased Graphene/Silicon Heterojunction Schottky Diode Sensor. *Small* 10(8), 1555–1565.

Sinha, D., and J. U. Lee (2014). Ideal Graphene/Silicon Schottky Junction Diodes. *Nano Letters* 14(8), 4660–4664.

Somvanshi, D., and S. Jit (2014). Analysis of I-V Characteristics of Pd/ZnO Thin Film/n-Si Schottky Diodes with Series Resistance. *Journal of Nanoelectronics and Optoelectronics* 9(1), 21–26.

Stolterfoht, M., P. Caprioglio, C. M. Wolff, J. A. Márquez, J. Nordmann, S. Zhang, D. Rothhardt, et al., (2019). The Impact of Energy Alignment and Interfacial Recombination on the Internal and External Open-Circuit Voltage of Perovskite Solar Cells. *Energy and Environmental Science* 12(9), 2778–2788.

Sze, S. M., and K. K. Ng (2007). Physics of Semiconductor Devices, *3rd Edition.; John Wiley & Sons, Inc.; NJ*.

Tang, X., G. Wu, H. Zhang, and K. W. C. Lai (2015). Tuning Graphene/Silicon Schottky Barrier Height by Chemical Doping. In *IEEE-NANO 2015 - 15th International Conference on Nanotechnology*, 1250–1253.

Tomer, D., S. Rajput, L. J. Hudy, C. H. Li, and L. Li (2015). Inhomogeneity in Barrier Height at Graphene/Si (GaAs) Schottky Junctions. *Nanotechnology* 26(21), 215702.

Tongay, S., M. Lemaitre, X. Miao, B. Gila, B. R. Appleton, and A. F. Hebard (2012). Rectification at Graphene-Semiconductor Interfaces: Zero-Gap Semiconductor-Based Diodes. *Physical Review X* 2(1), 011002.

Tyagi, M. S. (1984). Physics of Schottky Barrier Junctions. In *Metal-Semiconductor Schottky Barrier Junctions and Their Applications*. New York, Plenum, 1–60.

Wan, X., Y. Xu, H. Guo, K. Shehzad, A. Ali, Y. Liu, J. Yang, et al., (2017). A Self-Powered High-Performance Graphene/Silicon Ultraviolet Photodetector with Ultra-Shallow Junction: Breaking the Limit of Silicon? *Npj 2D Materials and Applications* 1(1), 1–8.

Wang, C., Y. Dong, Z. Lu, S. Chen, K. Xu, Y. Ma, G. Xu, X. Zhao, and Y. Yu (2019). High Responsivity and High-Speed 1.55 Mm Infrared Photodetector from Self-Powered Graphene/Si Heterojunction. *Sensors and Actuators, A: Physical* 291, 87–90.

Wang, Y., S. Yang, A. Ballesio, M. Parmeggiani, A. Verna, M. Cocuzza, C. F. Pirri, and S. L. Marasso (2020). The Fabrication of Schottky Photodiode by Monolayer Graphene Direct-Transfer-on-Silicon. *Journal of Applied Physics* 128(1), 014501.

Wang, Y., S. Yang, D. R. Lambada, and S. Shafique (2020). A Graphene-Silicon Schottky Photodetector with Graphene Oxide Interlayer. *Sensors and Actuators, A: Physical* 314, 112232.

Wang, Y. Y., Z. H. Ni, T. Yu, Z. X. Shen, H. M. Wang, Y. H. Wu, W. Chen, and A. T. S. Wee (2008). Raman Studies of Monolayer Graphene: The Substrate Effect. *Journal of Physical Chemistry C* 112(29), 10637–10640.

Wolff, C. M., P. Caprioglio, M. Stolterfoht, and D. Neher (2019). Nonradiative Recombination in Perovskite Solar Cells: The Role of Interfaces. *Advanced Materials* 31(52), 1902762.

Xiang, D., C. Han, Z. Hu, B. Lei, Y. Liu, L. Wang, W. P. Hu, and W. Chen (2015). Surface Transfer Doping-Induced, High-Performance Graphene/Silicon Schottky Junction-Based, Self-Powered Photodetector. *Small* 11(37), 4829–4836.

Yu, T., F. Wang, Y. Xu, L. Ma, X. Pi, and D. Yang (2016). Graphene Coupled with Silicon Quantum Dots for High-Performance Bulk-Silicon-Based Schottky-Junction Photodetectors. *Advanced Materials* 28(24), 4912–4919.

Zeng, L., C. Xie, L. Tao, H. Long, C. Tang, Y. H. Tsang, and J. Jie (2015). Bilayer Graphene Based Surface Passivation Enhanced Nano Structured Self-Powered near-Infrared Photodetector. *Optics Express* 23(4), 4839–4846.

Zhang, T., M. B. Nix, B. Y Yoo, M. A. Deshusses, and N. V. Myung (2006). Electrochemically Functionalized Single-Walled Carbon Nanotube Gas Sensor. *Electroanalysis* 118(12), 1153–1158.

VITA

EDUCATION

2022, Ph.D. in Physics, Graduate School of Engineering and Sciences, İzmir Institute of Technology, İzmir / Turkey
Thesis Title: Performance Enhancement of Graphene/Silicon Based Near-Infrared Schottky Photodiodes
Supervisor: Prof. Dr. Cem Çelebi

2014, M.Sc. in Physics, Graduate School of Engineering and Sciences, İzmir Institute of Technology, İzmir / Turkey
Thesis Title: Structural and Magnetic Characterization of Nitrogen Ion Implanted Stainless Steel and CoCrMo Alloys
Supervisor: Prof. Dr. Orhan Öztürk

2008, B.Sc. in Physics Education, Yüzüncü Yıl University, Van / Turkey

PUBLICATIONS

M. Fidan, G. Dönmez, A. Yanilmaz, Ö. Ünverdi, C. Çelebi
Light-induced modification of the Schottky barrier height in graphene/Si based near-infrared photodiodes
Infrared Physics & Technology 123, 104165 (2022)

M. Fidan, Ö. Ünverdi, C. Çelebi
Enhancing the photo-response characteristics of graphene/n-Si based Schottky barrier photodiodes by increasing the number of graphene layers
Journal of Vacuum Science & Technology A, 40, 032203 (2022)

A. Yanilmaz, M. Fidan, Ö. Ünverdi, C. Çelebi
Graphene/SOI-based self-powered Schottky barrier photodiode array
Applied Physics Letters, 121, 011105 (2022)

M. Fidan, Ö. Ünverdi, C. Çelebi
Junction area dependent performance of graphene/silicon based self-powered Schottky photodiodes
Sensors and Actuators A: Physical, 331, 112829 (2021)

N. Şahan, M. Fidan, C. Çelebi
Adsorbate-induced enhancement of the spectral response in graphene/silicon based-Schottky barrier photodetectors
Applied Physics A 126, 938 (2020)